Die approbierte Originalversion dieser Diplom-/Masterarbeit ist in der Hauptbibliothek der Technischen Universität Wien aufgestellt und zugänglich.
http://www.ub.tuwien.ac.at

The approved original version of this diploma or master thesis is available at the main library of the Vienna University of Technology.
http://www.ub.tuwien.ac.at/eng

M A S T E R T H E S I S

Operational Experience at the MedAustron Injector Teststand
Simulation and Measurement

conducted at the
Institute of Nuclear Physics of TU Wien
in cooperation with CERN and EBG MedAustron

under supervision of

Doz. Dr. Michael Benedikt

by

Tobias Kulenkampff, BSc

Arndtstraße 11/11
A-1120 Wien

Wien, 05.09.2016

MedAustron ist ein Zentrum für Ionentherapie und Forschung in Wiener Neustadt. Die Anlage kann grob in folgende Sektionen unterteilt werden: Ionenquellen und Niederenergietransferlinien, Linearbeschleuniger, Mittelenergietransferlinie, Synchrotron und Hochenergietransferlinie. Der Linearbeschleuniger wird wieder in zwei Abscnitte unterteilt. Einen Radiofrequenzquadrupol und einen Driftröhrenbeschleungier. Das Thema der Arbeit ist die Kommissionierung der Niederenergietransferlinie und des Radiofrequenzquadrupols im Rahmen eines Teststandes am CERN. Theoretische Untersuchungen des Designs werden mit Messungen ergänzt Adaptierungen und die Inbetriebnahme mit all ihren Hürden beschrieben.

MedAustron is a center for ion-therapy and research in Wiener Neustadt. The accelerator-complex can be subdivided into the following sections: ion source and low energy transfer line, linear accelerator, medium energy transfer line, synchrotron and high energy transfer line. The linear accelerator can again be partitioned into two parts. A radio frequency quadrupole and a drift tube linac. The topic of this thesis is the commissioning work of the low energy transfer line and the radio frequency quadrupole in the framework of a test stand operated at CERN. Theoretical investigations are being paired with measurements and the commissioning with all its challenges is presented.

I want to thank my supervisor Michael Benedikt for providing me the unique opportunity of working in such a fruitful environment as CERN and allowing me to pursue my goals in the medical application of accelerators. I am also grateful for Edgar Sargsyan's continuous support during the commissioning process and everyone at MedAustron who helped me operate the injector test stand. Last, but not least I want to thank my family to give me the outstanding privilege of studying physics and their support along the way.

Contents

1 Introduction **1**

2 Basic Principles and Parameters of an RF Linac **3**

3 Particle Dynamics **9**
3.1 Longitudinal Particle Dynamics in Linacs 9
3.2 Transverse Particle Dynamics in RF linacs 13
3.2.1 Quadrupole Focusing in a Linac 15
3.2.2 Dipole magnets 17
3.2.3 Solenoid 18
3.3 Linear Particle Dynamics 19
3.3.1 The Matrix Formalism 19
3.3.2 Emittance, Phase-Space and Liouville-Theorem 21
3.4 The Radio Frequency Quadrupole 22

4 Injector Test Stand **29**
4.1 purpose 29
4.2 Beam-line description and functional specifications 29
4.2.1 Beam-line composition 29
4.2.2 ECR ion source 30
4.2.3 Radio Frequency Quadrupole and Inter-tank Matching Section 32
4.2.4 Beam Diagnostics 34
4.2.5 Test Benches 34
4.2.6 Measurement stages 36
4.3 Theoretical studies, simulation, and measurements 37
4.3.1 Preliminary measurements 38
4.3.2 Beam Tracking 39
4.3.3 Matching 41
4.3.4 RFQ sensitivity studies 43
4.3.5 RFQ acceptance 48
4.3.6 Experimental results 52
4.3.7 Beam-line configuration and measurements 54
4.3.8 Conclusions from the ITS operation 77

5 Simulation Software **79**
5.1 TRACE 3D 79
5.2 Path Manager 79

5.3 genBeam 81
5.4 MedAustron Emittace Analysis 81
5.5 PARMTEQM 82
5.6 PlotWin 82

1 Introduction

In the field of cancer treatment radiation therapy is one of the three pillars next to operation and chemo therapy. A problem with conventional radiation therapy via x-rays lies within the dose distribution. A large amount of dose is deposited in the first centimeters of tissue after which an exponential decay takes place. This poses an issue with treating tumors in deeper parts of the body. Radiation from many directions can reduce this problem, but not solve the underlying issue. An alternative to this form of radiation treatment is hadron therapy. The energy placement of hadrons can be controlled via their kinetic energy. Depending on their energy, they will deposit the vast majority of their energy in a certain depth of tissue. This is called a Bragg peak

In Figure 1.1 the different behaviors of photons and hadrons are displayed. In the top figure the Bragg peak for an ion beam is clearly visible. To address differents depths in the body, different energies can be used. The dose distribution will begin to form a plateau in the are of interest. What is remarkable is the fact that the dose distribution around the tumor is much lower than in the case of photons. This allows very precise treatment whilst sparing healthy tissue of high levels of irradiation. MedAustron is the first facility in Austria offering this type of treatment. It is a synchrotron complex with three treatment rooms which can supply a range of different ions over an energy spectrum suitable for medical treatment. In addition there is one room for non-clinical research. The accelerator complex can be subdivided into 5 segments:

- Ion source and low energy beam transfer
- Linear accelerator
- Medium energy beam transfer
- Synchrotron
- High energy beam transfer

Each segment has its own challenges when it comes to providing beam for downstream applications [2]. The scope of this thesis was to run an injector test-stand (ITS) for parts of the linear accelerator set-up. It consisted of an ion-source, a low energy transfer line and a radio frequency quadrupole (RFQ). The final goal was to verify the performance of the RFQ. To understand most of the system, simulation and measurements were performed in parallel and compared whenever possible. The knowledge gathered could later be used in the commissioning of the accelerator complex in Wiener Neustadt.

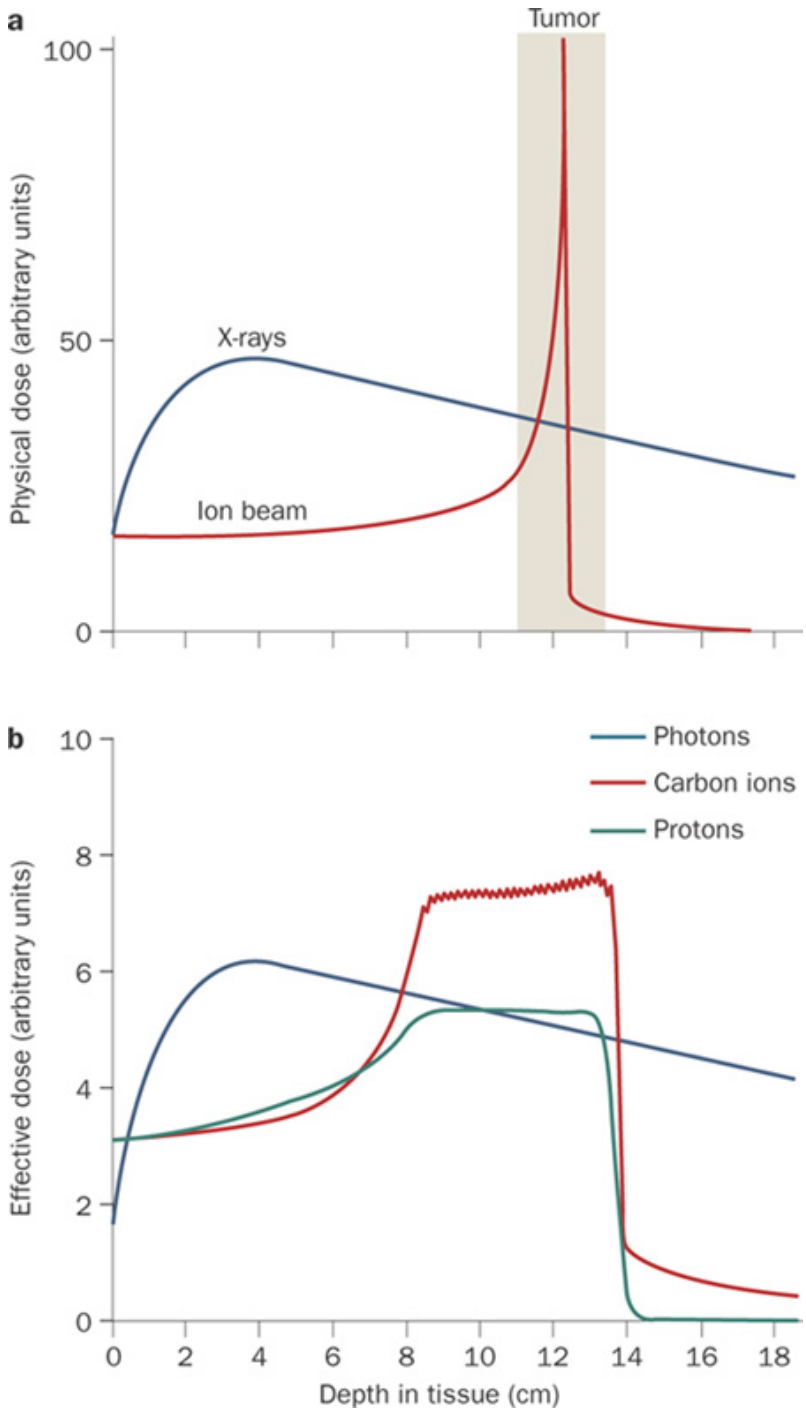

Figure 1.1: Penetration behavior of different radiation types. [1]

2 Basic Principles and Parameters of an RF Linac

The acceleration of charged particles in an RF linac is done by time dependent electromagnetic fields powered by an RF power source of a specified frequency. The shape of the field in the accelerator is defined by so called cavities. A cavity is the metallic boundary which generates the field during operation.Each cavity is characterized by its shape and corresponding resonance frequency. A lot of the content presented is taken from [3], a highly recommended book on the physics of RF linacs.

A cavity the metallic boundary which defines the shape of the field used for acceleration. Each cavity has its own resonance frequency which only depends on its geometry. The field of the cavity is driven by the power source with the resonance frequency of the cavity. A beam of ionized particles that enters the cavity changes its energy depending of the phase of the particle in reference to the field. How this occurs and what effect the phase on energy gain has will be described in section 3.1. The cavity design has a very big influence on the efficiency of an RF linac. There are some parameters that have to be taken into account during the design stage. For the cavity itself these are:

- The field pattern inside a cavity.
- Minimizing ohmic losses on the wall whilst maximising the stored energy.

But not only is the design of the cavity of great importance, also the beam optics play a big role. The challenges which occur are

- Timing of the RF field with the particle beam.
- Maintain the beam within certain geometrical boundaries i.e. as small as possible during acceleration.
- Matching to downstream sections.

For a first idea on how acceleration in an RF field works. A particle shall be considered to be accelerated by a travelling wave described by 2.1

$$E_z(z,t) = E(z)cos[\omega t - \int_0^z dz' k(z') + \Phi] \tag{2.1}$$

in which $E(z)$ is the longitudinal field distribution at maximum voltage.

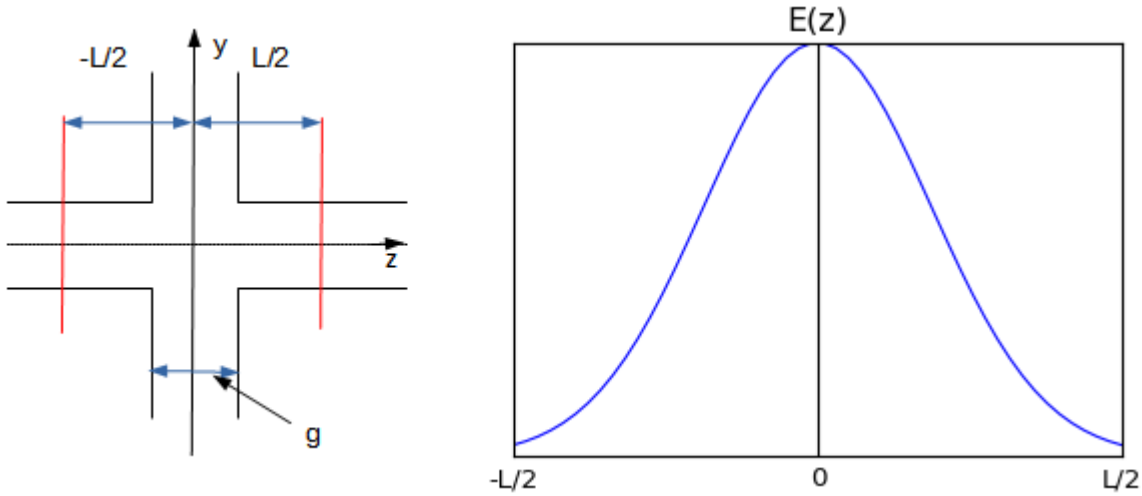

Figure 2.1: Gap geometry and field distribution

The wavenumber $k(z) = \omega/v_p(z)$ takes into account that the phase velocity $v_p(z)$ is not constant through out the entire cavity. If one considers a particle travelling in the +z direction which's velocity $v(z)$ at any given point z is equal to v_p then the particles arrives at any position z after the time $t(z) = \int_0^z dz'/v_p(z')$. The forces experienced by a particle with charge q in the electromagnetic field is given by $F_z = qE(z)\cos(\Phi)$. The particle that satisfies the condition of $v(z) = v_p(z)\ \forall\ z$ is called the *synchronous particle* and the phase Φ is called the *synchronous phase*

In a cavity it can be assumed that the field can be described as a standing wave of the form:

$$E(z,t) = E(z)\cos(\omega t + \phi) \tag{2.2}$$

For efficiency reasons it is of course of interest to concentrate the RF power of the generator within the area where the beam is located. Therefore the cavity geometry plays a big role in the efficiency of a linac. Before looking further into beam dynamics, the most important cavity design parameters will be presented and explained.

- Average electric field.

$$E_0 = \frac{1}{L}\int_{-L/2}^{L/2} E_z(x=0, y=0, z)dz \tag{2.3}$$

  The value of the average electric field depends on geometry, resonating mode and frequency.

- transit-time factor

  If one assumes the accelerating field to be zero at the boundaries of the gap shown in 2.1 the gained energy by a particle simply sums up to:

$$\Delta W = q\int_{-L/2}^{L/2} E(0,z)cos(\omega t(z) + \phi)dz \tag{2.4}$$

using $\cos(x \pm y = \cos(x)\cos(y) \mp \sin(x)\sin(y)$ one can rewrite 2.4 as

$$\Delta W = q \int_{-L/2}^{L/2} E(0,z)[\cos(\omega t) cos(\phi) - \sin(\omega t)\sin(\phi)]dz \tag{2.5}$$

Additionally one can introduce an axial RF voltage, defined by

$$V_0 \equiv \int_{-L/2}^{L/2} E(0,z)dz \tag{2.6}$$

This leads to the simple expression

$$\Delta W = qV_0 T cos(\phi) \tag{2.7}$$

The factor T in equation 2.7 is the so called *transit-time factor*. It is a number that allows a comparison of the effectiveness of the acceleration of the particle in a gap in reference to a dc field powered by the same voltage.

$$T \equiv \frac{\int_{-L/2}^{L/2} E(0,z)\cos(\omega t(z))dz}{\int_{-L/2}^{L/2} E(0,z)dz} - tan(\Phi)\frac{\int_{-L/2}^{L/2} E(0,z)\sin(\omega t(z))dz}{\int_{-L/2}^{L/2} E(0,z)dz} \tag{2.8}$$

Equation 2.7 is a very useful expression as it gives the opportunity to quickly see whether a particle is accelerated or decelerated simply by knowing its phase. If the particle arrives at the centre of the gap when the field is at its maximum then $\Phi = 0$. If the particles arrives at the centre before the field has reached its maximum then $\Phi < 0$. If it arrives later then $\Phi > 0$. For non relativistic particles, it can be useful to accelerate particles with $\Phi < 0$ as this will allow longitudinal focusing. This technique will be discussed in section 3.1 when longitudinal beam dynamics become of importance. Equation 2.7 can be rewritten if one defines an average axial field $E_0 = V_0/L$:

$$\Delta W = qE_0 T\cos(\phi)L \tag{2.9}$$

Equation 2.9 looks deceivingly simple, but a lot of physics comes into play when calculating the *time-transit factor* T. The field between the electrodes is generally assumed to be symmetrical. This simplifies equation 2.8 to the point that the uneven integral in the second term results in 0. So under the assumption of an symmetrically distributed field the transit-time factor is:

$$T = \frac{\int_{-L/2}^{L/2} E(0,z)\cos(\omega t(z)dz}{\int_{-L/2}^{L/2} E(0,z)dz} \tag{2.10}$$

The transit-time factor depends on the geometry of the gap and the frequency of the structure. For efficiency it is desired to be as close to 1 as possible.[3]

- Shunt impedance R_s

$$P_d = \frac{V^2}{R_s} \tag{2.11}$$

The Shunt impedance is a factor which describes the relation between the accelerating voltage and the power dissipated in the cavity walls. Usually the shunt impedance is given in Ω per unit length. A more general definition that also takes traveling waves into account is:

$$\frac{dP}{dz} = -\frac{E_z^2}{r} \; with \; r = \frac{R_s}{L} \tag{2.12}$$

In equation 2.12 L is the length of the cavity, r is the shunt impedance per unit length, E_z is the amplitude of the accelerating field and $\frac{dP}{dz}$. The negative sign indicates that the power transported in a traveling wave structure decreases because of losses.
For standing wave-cavities an uncorrected shunt impedance Z is sometimes given.

$$R_s = ZT^2 \tag{2.13}$$

where T is the time-transit factor given in equation 2.10. To minimize power losses it is obviously of high interest to create a structure which's shunt impedance per unit length is as high as possible. Power losses per unit-length within a cavity are proportional to the square of the wall-current i_w and the wall resistance per unit-length r_w:

$$\frac{dP}{dz} \propto i_w^2 r_w \tag{2.14}$$

The axial electric field is proptional to the ratio of the wall current and the cavity radius b.

$$E_z = \frac{i_w}{b} \tag{2.15}$$

The wall resistance r_w is given by:

$$r_w = \frac{\rho}{2\pi b \delta} \tag{2.16}$$

δ is the skin depth which is equal to:

$$\delta = \sqrt{\frac{2\rho}{\omega\mu}} \tag{2.17}$$

Combining all equations and using $b \propto 1/\omega$ leads to

$$r \propto \sqrt{\omega} \tag{2.18}$$

So it is more efficient to operate a linac at very high frequencies. Unfortunately the frequency is limited by the size of the aperature ($b \propto 1/\omega$) and therefor can not exceed a certain threshold since it needs to be big enough to let the beam pass through. [4]

- Quality factor Q

  The quality factor Q is defined as the ratio between the stored energy and power losses on the wall.

$$Q = \frac{\omega E_s}{P_d} \tag{2.19}$$

  Q is a function of the geometry and the surface resistance of the material. [5]

- Kilpatrik sparking criterion

  In a RF accelerator the field used for acceleration is limited by the breakdown-criteria. If the field gets too high for the structure then sparks between elements will occur leading to a breakdown of the device. In 1950 W.D. Kilpatrick analysed data of RF-breakdowns and defined the condition for a breakdown-free operation of cavities as [6]

$$f = 1.64 MHz E^2 exp{-}8.5/E \tag{2.20}$$

  Equation 2.20 is the least square fit optimization to empirical data and is shown in figure 2.2.

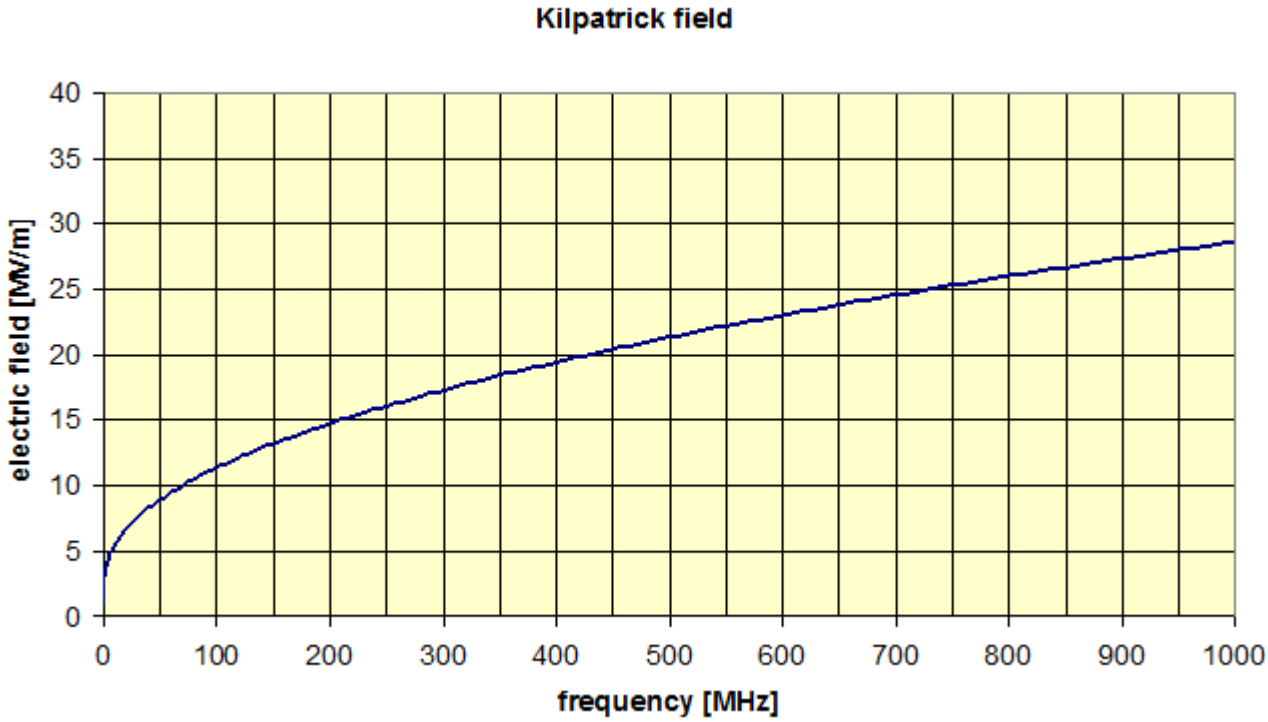

Figure 2.2: Kilpatrick limit - the maximum field at a given frequency which can be achieved before sparking
[5]

3 Particle Dynamics

3.1 Longitudinal Particle Dynamics in Linacs

Longitudinal particle dynamics play a significant role in terms of acceleration in a linac. Phase and momentum spread are the relevant coordinates in longitudinal dynamics. Depending of the phase, a beam might either become longitudinally (de-)focused or (de-)accelerated. Imagine a synchronous particle with a negative synchronous phase. It will arrive in an accelerating gap before the field reaches its crest. So a particle that arrives ealier than the synchronous particle will experience less accelerating force and a particle that arrives later will experience a stronger force. See figure 3.1 [5]. Therefore in the non-relativistc case, the particles will move closer towards each other. This process is called longitudinal focusing. It creates bunches of particles, that closely move around the synchronous particle, assuming the limits of stability are respected.

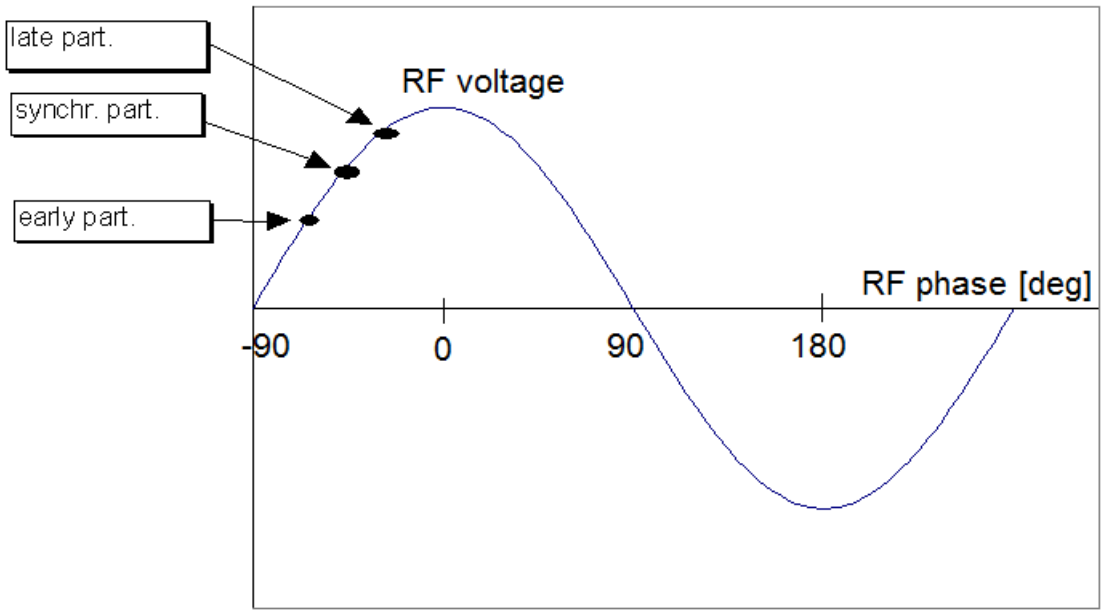

Figure 3.1: early and late particles in respect to the synchronous particle [5]

To get an idea of the beam dynamics in a linac, some basic properties will be presented based in the dynamics in a DTL (drift-tube linac). A drift-tube Linac

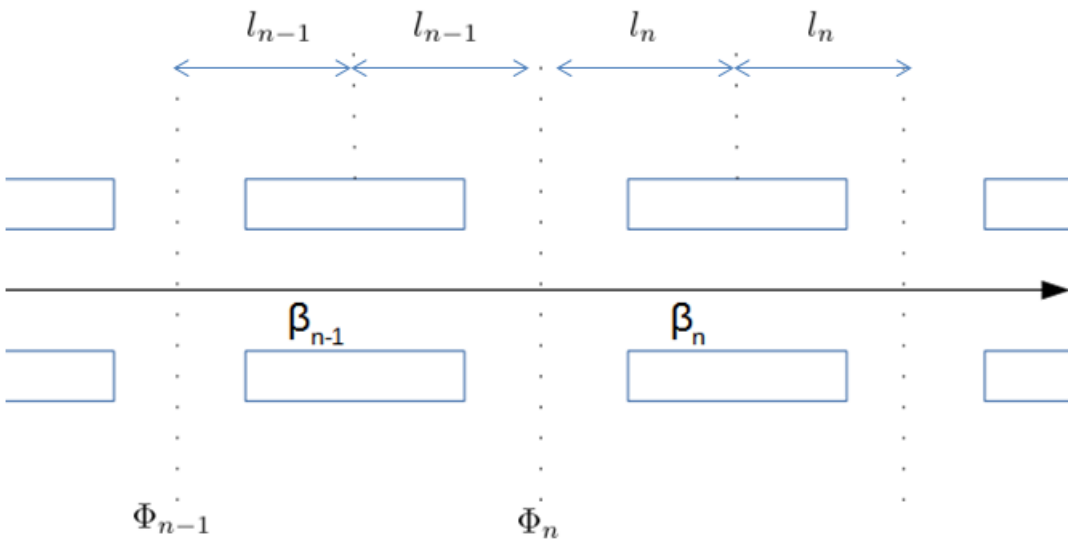

Figure 3.2: cells in a DTL

consist of adjacent drift tubes, in which the particles experience no interaction with the field, and gaps in between them, where acceleration occurs. To describe longitudinal dynamics it is necessary to derive the equations of motion in such a structure as seen in figure 3.2. The blue boxes represent cross-sections of the drift tubes. Φ is the phase, $\beta = v/c_0$.

Moving from gap $n-1$ to gap n (within a drift tube) a particle has a constant velocity β_{n-1}. With the particles advancing to the next gap the RF changes according to

$$\phi_n = \phi_{n-1} + \omega \frac{2l_{n-1}}{\beta_{n-1}c} + \begin{cases} \pi & \text{for } \pi \text{ mode} \\ 0 & \text{for 0 mode} \end{cases} \tag{3.1}$$

the half-cell length is chosen such that:

$$l_{n-1} = \frac{N\beta_{s,n-1}\lambda}{2} \text{ where N} = \begin{cases} \frac{1}{2} & \text{for } \pi \text{ mode} \\ 1 & \text{for 0 mode} \end{cases} \tag{3.2}$$

So the length between drift-tube centers accumulates to $L_n = N(\beta_{s,n-1}+\beta_{s,n})\lambda/2$. For an arbitrary particle, the phase change, when traveling from gap n-1 to gap n, relative to that of the synchronous particle is

$$\Delta(\phi - \phi_s)_n = \Delta\phi_n - \Delta\phi_{s,n} = 2\pi N\beta_{s,n-1}\left(\frac{1}{\beta_{n-1}} - \frac{1}{\beta_{s,n-1}}\right) \tag{3.3}$$

For small velocity changes between gaps, one can apply Taylor's formula on the expression in parenthesis.

$$\frac{1}{\beta} - \frac{1}{\beta_s} = \frac{1}{\beta_s + \delta\beta} - \frac{1}{\beta_s} \simeq \frac{\delta\beta}{\beta_s^2} \tag{3.4}$$

Replacing $\delta\beta$ with $\delta\beta = \delta W/mc^2\gamma_s^3\beta_s$ yields:

$$\Delta(\phi - \Phi_s)_n = -2\pi N \frac{W_{n-1} - W_{s,n-1}}{mc^2\gamma_{s,n-1}^3\beta_{s,n-1}^2} \tag{3.5}$$

The energy change of a particle relative to that of a synchronous particle can be written as using equation 2.7:

$$\Delta(W - W_s)_n = \Delta W_n - \Delta W_{s,n} = qE_0TL_n(\cos(\varphi_n) - \cos(\varphi_{s,n})) \tag{3.6}$$

Equation 3.5 and 3.6 are coupled difference equations for relative phase and energy change and can be solved using numerical techniques. The next step is to move from discrete difference equations to continuous differential equations. In order to take this step n will be treated as a continuous variable.

$$\Delta(\phi - \phi_s) \rightarrow \frac{d(\phi - \phi_s)}{dn} \tag{3.7}$$

$$\Delta(W - W_s) \rightarrow \frac{d(W - W_s)}{dn} \tag{3.8}$$

To replace n it is possible to use $n = s/N\beta_s\lambda$. All this leads to:

$$\gamma_s^3 \frac{d(\phi - \phi_s)}{ds} = -2\pi \frac{W - W_s}{mc^2\lambda} \tag{3.9}$$

$$\frac{d(W - W_s)}{ds} = qE_0T(\cos(\phi) - \cos(\phi_s)) \tag{3.10}$$

By differentiation of 3.9 and substituting 3.10 for the righthand side one obtains a non-linear second order differential equation for the longitudinal motion.

$$\frac{d}{ds}\left[\gamma_s^3\beta_s^3 \frac{d(\phi - \phi_s)}{ds}\right] = -2\pi \frac{qE_0T}{mc^2\lambda}(\cos(\phi) - \cos(\phi_s)) \tag{3.11}$$

Executing all steps in the differentiation results in

$$\gamma_s^3\beta_s^3 \frac{d^2(\phi - \phi_s)}{ds^2} + 3\gamma_s^2\beta_s^2\left[\frac{d}{ds}(\gamma_s\beta_s)\right]\left[\frac{d(\phi - \phi_s)}{ds}\right] + 2\pi \frac{qE_0T}{mc^2\lambda}(\cos(\phi) - \cos(\phi_s)) = 0 \tag{3.12}$$

Equation 3.12 is a nonlinear second order differential equation which describes the phase motion. Phase is proportional to time. The more negative the phase is, the earlier will a particle arrive relative to the maximum of the field. This also results in a spatial separation of the particles.

$$z - z_s = -\frac{\beta_s\lambda}{2\pi}(\phi - \phi_s) \tag{3.13}$$

For a small acceleration rate and under the assumption that E_0T, ϕ_s, and β_s are constant it is convenient to use the following notation.

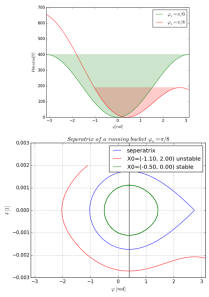

Figure 3.3: top: potential energy
bottom: longitudinal phase-space trajectory

$$\mathcal{W} \equiv \delta\gamma = \frac{W - W_s}{mc^2} \qquad A \equiv \frac{2\pi}{\beta_s^3 \gamma_s^3 \lambda} \qquad B \equiv \frac{qE_0T}{mc^2} \tag{3.14}$$

With this notation equations 3.9, 3.10, and 3.11 take on a simpler form

$$\mathcal{W}' \equiv \frac{d\mathcal{W}}{ds} = B(\cos(\phi) - \cos(\phi_s)) \tag{3.15}$$

$$\phi' \equiv \frac{d\phi}{ds} = -A\mathcal{W} \tag{3.16}$$

$$\phi'' \equiv \frac{d^2\phi}{ds^2} = -AB(\cos(\phi) - \cos(\phi_s)) \tag{3.17}$$

Integrating 3.17 gives

$$d\phi' = -AB(\cos(\phi) - \cos(\phi_s))ds \tag{3.18}$$

With $ds = d\phi/\phi'$. Multiplying by ϕ', integrating and substituting 3.16 one finally obtains

$$\frac{A\mathcal{W}^2}{2} + B(sin(\phi) - \phi\cos(\phi_s)) = H_\phi \tag{3.19}$$

H_ϕ is a constant of the motion and is identified with the Hamiltonian of the system. The first term being the kinetic energy and the second being the potential energy. The potential energy has a well for $-\pi < \phi_s < 0$. From 2.7 one knows that acceleration occurs between $-\pi/2 \leq \phi_s \leq \pi/2$. The stable region for acceleration is between ϕ_2 and $-\phi_s$ where ϕ_2 can be derived from solving $H_\phi(\phi_2) = H_\phi(\phi_s)$.

In figure 3.3 one can see longitudinal phase-space trajectories and the potential energy term from 3.19 for $\phi_s = \pi/8$. At the maximum of the potential term ,which lies at $-\phi_s$, is no change of the phase of a particle relative to the synchronous particle and therefor $\phi' = 0$. From equation 3.16 it is obvious that $\mathcal{W} = 0$. For $\phi = -\phi_s$ the Hamiltonian becomes

$$B[sin(-\phi_s) - (-\phi_s\cos(\phi_s))] = H_\phi \tag{3.20}$$

Thus by knowing the synchronous phase one can easily determine the Hamiltonian of the system and the seperatrix since all points on the seperatrix must satisfy the condition:

$$\frac{A\mathcal{W}^2}{2} + B(sin(\phi) - \phi\cos(\phi_s)) = -B(sin(\phi_s) - \phi_s\cos(\phi_s)) \tag{3.21}$$

The seperatrix is a very important curve within the longitudinal phase-space since it defines the area in which the particle motion is stable. A common name for the seperatrix for ϕ_s is *bucket* and for accelerating phase the name *fish* is used widely. The phase width of the seperatrix is given by the two solutions for $\mathcal{W} = 0$. One solution is found at $\phi_1 = -\phi_s$ and the other is at ϕ_2 which is obtained by solving $H_\phi(\phi_2) = H_\phi(\phi_s)$ for ϕ_2. Or simpler just by solving equation 3.22. At ϕ_2 3.21 becomes

$$sin(\phi_2) - \phi_2\cos(\phi_s) = \phi_s\cos(\phi_s) - sin(\phi_s) \tag{3.22}$$

So the total phase-width of the seperatrix is

$$\psi = |\phi_s| + |\phi_s| = -\phi_s - \phi_2 \tag{3.23}$$

Using 3.23, equation 3.21 becomes for $\mathcal{W} = 0$

$$sin(\phi_2) = -sin(\phi_s + \psi) = -(sin(\phi_s)\cos(\psi) + sin(\psi)\cos(\phi_s)) \tag{3.24}$$

Inserting 3.24 into 3.22 and applying elementary formula-manipulation one obtains

$$tan(\phi_s) = \frac{sin(\psi) - \psi}{1 - \cos(\psi)} \tag{3.25}$$

For very small ψ and ϕ_s one can again apply the Taylor expansion for the trigonometric functions. This results in

$$tan(\phi_s) \simeq -\frac{\psi}{3} \tag{3.26}$$

With $tan(\phi_s) \simeq \phi_s$ 3.26 becomes $\psi = 3|\phi_s|$ and $\phi_2 \simeq 2\phi_s$. So at $-\phi_s = -90°$ (where no acceleration occurs) the size of the *bucket* reaches its maximum. [3]

3.2 Transverse Particle Dynamics in RF linacs

In this section the transverse dynamics in an RF linac will be introduced. It is important to understand them because a beam has to maintain a certain size (among other things) to be able to be transfered through the beam line. One fundamental property of transverse beam dynamics can be understood when taking a closer look at the La Place equation after a Lorentz transformation into the rest frame of the particle where V is the electromagnetic potential.

$$\frac{\partial^2 V}{\partial x^2} + \frac{\partial^2 V}{\partial y^2} + \frac{\partial^2 V}{\partial z^2} = 0 \tag{3.27}$$

The magnetic forces are 0 and only the electrostatic forces can act. For an electrostatic field the Earnshaw theorem states, that the there is no static electric or magnetic field that can maintain an object in a stable condition. A stable condition would require a local potential minimum. Yet any electrical force derived from an a potential will always be divergenceless and therefor satisfy the La Place equation. But this means that there are no local minima or maxima. There are only saddle points. Therefor there is always one direction in which a force will act so that the configuration will not remain in an equilibrium state. For particle dynamics this means that there is no way to focus a particle bunch in all three directions of space. In general a particle travelling through an accelerating gap will also experience radial forces. It is necessary to understand what kind of influence these forces have on the dynamics of the particle. The symmetry of a gap geometry might lead to the conclusion that the radial electric forces would cancel each other out. Whilst this would be true in a static structure the time dependency of an RF gap will scatter this assumption. In general there will be a net radial impulse for which three mechanism are responsible.

- The field is not constant whilst a particle crosses the gap.
- The field is dependend on radial displacement of the particle.
- As a particle gets accelerated whilst travelling through a gap it will not spend the same time in each half of the gap, unless the particle is ultra relativistic.

For longitudinal stability (particle inside the *bucket*) it is necessary to have a negative synchronous phase ϕ_s of the synchronous particle. So when the particle enters the gap the field is rising and particles in the second half of the gap will experience a larger force than in the first half which will result in a net defocusing force. This is the qualitative explanation of the first mechanism. It also known as *RF-defocusing force*. The other mechanisms play a much larger role in electron linacs than in proton linacs and are therefore not of importance to this thesis.

The non-zero field components experienced by a particle of phase ϕ are

$$E_z = E_0 T I_0(Kr)\cos(\phi) \tag{3.28}$$

$$E_r = -\gamma_s E_0 T I_1(Kr) sin(\phi) \tag{3.29}$$

$$B_\Theta = -\frac{\gamma_s \beta_s}{c} E_0 T I_1 sin(\phi) \tag{3.30}$$

where I_0 and I_1 are the Bessel functions of zeroth and first order. With $K = 2\pi/\gamma_s\beta_s\lambda$ and E_0T being the average axial electric field of the traveling wave. So the radial Lorentz force component is:

$$\frac{dp_r}{dt} = q(E_r - \beta c B_\Theta) = -q\gamma_s(1-\beta\beta_s) I_1(Kr) E_0 T sin(\phi) \tag{3.31}$$

The radial momentum can be written in terms of $p_r = mc\gamma\beta r'$ where $r' = dr/dz$. So the radial momentum gain of a particle being accelerated over a length L is:

$$\Delta(\gamma\beta r') = -\frac{1}{mc}\int_0^L q\gamma_s(1-\beta\beta_s)I_1(Kr)E_0 T sin(\phi)\frac{dz}{\beta c} \tag{3.32}$$

$$= -q\frac{\gamma_s(1-\beta\beta_s)}{mc^2\beta}E_0 TLI_1(Kr)sin(\phi) \tag{3.33}$$

Under the assumption that $\beta \approx \beta_s$ equation 3.32 becomes

$$\Delta(\gamma\beta r') = -\frac{qE_0 TLI_1(Kr)sin(\phi)}{mc^2\gamma_s\beta_s} \tag{3.34}$$

For small Kr i.e. $Kr \ll 1$ the Bessel function can be appromixated via $I_1(Kr) \approx Kr/2$ which leads to

$$\Delta(\gamma\beta r') = \frac{\pi qE_0 TLsin(\phi)}{mc^2\gamma_s^2\beta_s^2\lambda}r \tag{3.35}$$

As established earlier for longitudinal stability it is necessary that the sign of ϕ_s is negative. On average the particles surrounding the synchronous particle should also have a negative phase. This means that the gain of the radial impulse will always be positive. In other words, there is always a defocusing effect. For relativistic velocities, this RF-defocusing effect vanishes due to the magnetic force canceling out the electric force.

3.2.1 Quadrupole Focusing in a Linac

In the previous section 3.2 it has been shown that there is always a defocusing force when dealing with a charge particle beam in a linac. The standard method to deal with this is to introduce quadrupole-magnets to the beamline which are necessary anyway to deal with inherent divergences. So in this section the equations of motion will be derived and analyzed. A magnetic quadrupole is amagnet with for iron pole shoes and coils in case of an electromagnet. The contour of the pole shoes is ideally hyperbolic. For an ideal quadrupole-magnet the field is linear when deviating from the axis.

$$B_z = -gx,\ B_x = -gz \tag{3.36}$$

The constant g is the gradient of the field which is related to the current flowing through the coil. In the empty space of a quadrupole-magnet, no currents are present and therefor it is possible to use the homogeneous Maxwell equation.

$$\nabla \times \vec{B} = 0 \tag{3.37}$$

Therefor the magnetic field can be derived from a scalar potential function V

$$\vec{B} = -\nabla V\, with\, V = gxz \tag{3.38}$$

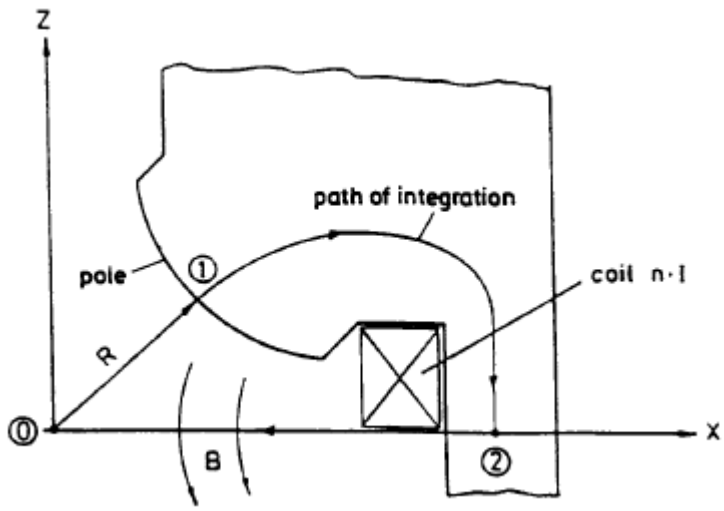

Figure 3.4: path of integration to calculate g

So the equipotential lines are hyperbolas as well with $xz = const$. The field lines are perpendicular to the equipotential lines. For high permeability of the iron used in the yoke ($\mu_r \gg 1$) the assumption for the quadrupole field 3.36 is very well satisfied. The relation between the gradient g and the current I can be derived applying the integral theorem

$$\oint \vec{H} \cdot d\vec{s} = nI \tag{3.39}$$

where n is the number of loops in the coil. The path of integration can be seen in 3.4[4]

$$nI = \oint \vec{H} \cdot d\vec{s} = \int_0^R H(r)dr + \int_1^2 \vec{H}_\epsilon + \int_2^0 \vec{H} \cdot d\vec{s} \tag{3.40}$$

The second integral is very small due to $\mu \gg 1$ and the third term is equal to 0 due to the fact the $\vec{H} \perp d\vec{s}$ at any point. So the only factor which remains is the first term $H(r) = gr/\mu_0$.

$$nI = \frac{1}{\mu_0} \int_0^R gr\, dr \qquad r = \sqrt{x^2 + y^2} \tag{3.41}$$

and therefor

$$g = \frac{2\mu_0 nI}{R^2} \tag{3.42}$$

It is convenient to normalize the quadrupole-gradient to the momentum of the particle which gives

$$k = \frac{eg}{p} = k[m^2] = 0.2998 \frac{g[T/m]}{p[GeV/c]} \tag{3.43}$$

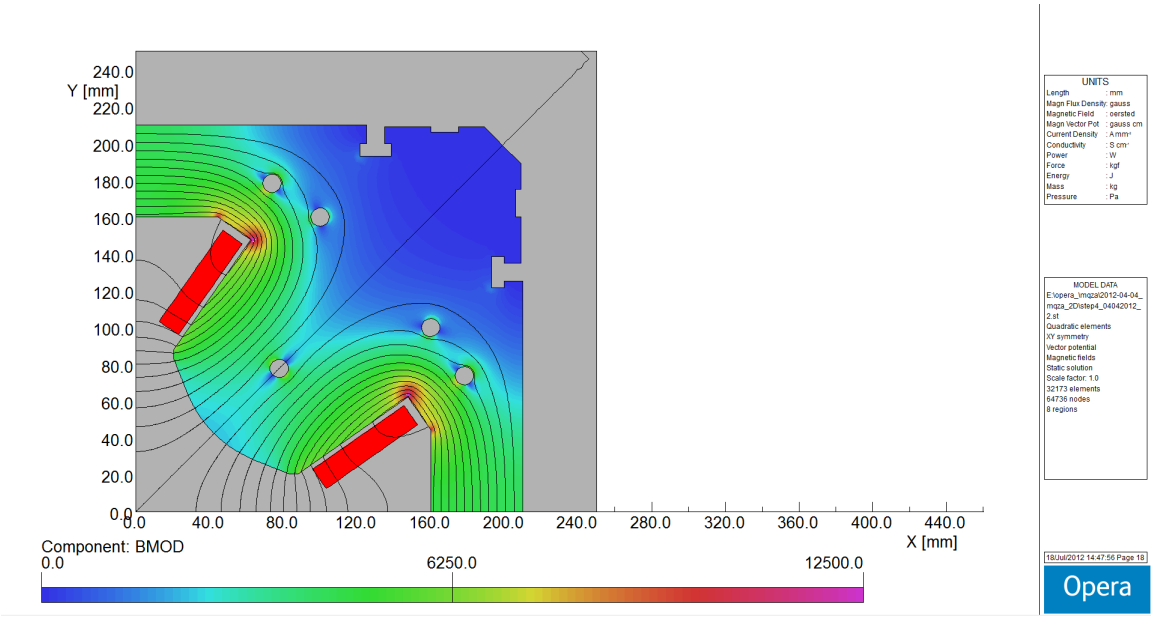

Figure 3.5: 2D simulation of one of the quadrupoles used in MedAustron's LEBT [7]

The Lorentz force acting in a quadrupole is:

$$\begin{aligned} F_x &= evB_z(x,z) = -evgx \\ F_x &= -evB_x(x,z) = evgz \end{aligned} \tag{3.44}$$

So the force acting on a particle in the horizontal plane is only dependent on its position on the horizontal axis. The same is valid for the vertical plane. It is now also very easy to see that a quadrupole focuses in one plane while defocusing in another. Changing the direction of the current powering the quadrupole will exchange the effects. In 3.5 one can see the magnetic field off one of the quadrupoles which are used in the LEBT of MedAustron.

In equation a very important often used concept was silently introduced. The concept of the magnetic rigidity $B\rho$.

$$B\rho = \frac{p}{q} \tag{3.45}$$

It is used to normalize magnetic fields such that the numerical values become energy independent which makes a theoretical description of an accelerator easier.

3.2.2 Dipole magnets

Dipole magnets are structure which provide a magnetic field that only has one component (neglecting fringe fields). Usually this component is chosen to be directed

in $\hat{e}_z$. The equation of motion of a charged particle in a dipole field is:

$$\dot{\vec{v}} = \frac{q}{\gamma m_0}(\vec{v} \times \vec{B}) \tag{3.46}$$

with $\vec{B} = B_0\hat{e}_z$. It can be shown that the magnetic field does no work on the particle. Energy is there for a conserved quantity. Due to the geometry of the magnetic field the vertical component of the particle's velocity also remains constant. Executing the cross product in 3.46 and combining the various components after applying a time derivation on this system of differential equations one obtains the following decoupled set of equations for an harmonic oscillator:

$$\ddot{v_x} + \omega_c v_x = 0\ddot{v_y} + \omega_c v_y = 0 \tag{3.47}$$

where $\omega_c = \frac{qE_0}{\gamma m_0}$. The solution to the equations is well known as:

$$\begin{aligned} v_x &= -v_m \sin(\omega_c t + \varphi) \\ v_y &= v_m \cos(\omega_c t + \varphi) \end{aligned} \tag{3.48}$$

Integrating 3.48 with respect to dt gives:

$$\begin{aligned} x &= R\cos(\omega_c t + \varphi) + x_0 \\ y &= R\sin(\omega_c t + \varphi) + y_0 \end{aligned} \tag{3.49}$$

So the particle follwing a cirle with $R = v_m/\omega_c$ around (x_0, y_0). The fact that the radius of the circle is depending on the particle's velocity gives the opportunity to use a dipole magnet as a spectrometer to separate particles with various energies. In the case of MedAustron this is necessary because the ECR ion-source creates mixed species of ions (for example $H^+, H_2^+, and H_3^+$ in Hydrogenoperation). H_3^+ is the ion in which lies the most interest and it is there for essential to segregate it from the other ions.

3.2.3 Solenoid

Another standard element in a low energy beam line is a solenoid magnet as a focusing element. Solenoid can be found in many applications such as electron guns, electron microscopes or in the case of MedAustron as an optical element in the LEBT. An assumption about the field of a solenoid is, that its field has axial symmetry about the z-axis.

$$\vec{B}(r, z) = B_z(z)\hat{e_z} + B_r(r, z)\hat{e_r} \tag{3.50}$$

A distinct property of a solenoid magnet is, that it introduces cross plane coupling.

3.3 Linear Particle Dynamics

The concepts which have been presented in the earlier sections are good for a qualitative understanding of the problems encountered in linear accelerators. In this framework each particle requires to be tracked through a field map representing the element. The very high number of particles (10^{10-12}) would quickly lead to exhaustive computational effort, so the idea is to find a simpler description of the particle dynamics.

3.3.1 The Matrix Formalism

Particle motion in an accelerator can be described by the so called Hill equations:

$$\begin{gathered} x'' - \left(k(s) - \frac{1}{\rho^2(s)}\right) x = \frac{1}{\rho(s)} \frac{\Delta p}{p} \\ y'' + k(s) y = 0 \end{gathered} \tag{3.51}$$

with $k(s)$ being continuous lattice-function to describe the optical elements at a given point s.

For the majority of optical elements used in a linac the horizontal and vertical dynamics can be treated separately (i.e. no coupling between the planes). Dispersion is introduced by bending magnets and taken into account by the right hand side of the horizontal equation. For simplicity it is assumed that bending magnets only act in the horizontal plane.

In 3.51 x/ρ^2 describes the "weak focusing" introduced by a bending magnet. In high energy accelerators like CERN SPS, this term can usually be negelected compared to the "strong focusing" provided by the k-order magnets (quadrupoles, sextupoles, and so on).

The general solution to a inhomogeneous differential equation of the kind in **??** looks like

$$\begin{gathered} x(s) = C(s)x_0 + S(s)x_0' + D(s)\tfrac{\Delta p}{p_0} \\ y(s) = C(s)y_0 + S(s)y_0' \end{gathered} \tag{3.52}$$

$C(s)$ and $S(s)$ are (co)-sinelike functions, which are the solutions to the homogeneous equation, x_0, x_0', y_0, y_0' are constants determined by initial conditions and $D(s)\frac{\Delta p}{p_0}$ is the solution to the inhomogeneous problem for the horizontal plane. The particle coordinates are now linearly related to the initial conditions.

$$\begin{pmatrix} x \\ x' \\ \frac{\Delta p}{p_0} \end{pmatrix}_s = \begin{pmatrix} C & S & D \\ C' & S' & D' \\ 0 & 0 & 1 \end{pmatrix} \begin{pmatrix} x \\ x' \\ \frac{\Delta p}{p_0} \end{pmatrix}_{s_0} \tag{3.53}$$

The vertical motion is described the same way, just without the matrix elements coupling to $\frac{\Delta p}{p_0}$.

For a piecewise constant lattice function K(s) it is now possible to easily calculate the effects of optical elements on the particles. The most commonly used matrices are presented as follows:

Drift space of length l:

$$M_x = M_y = \begin{pmatrix} 1 & l & 0 \\ 0 & 1 & 0 \\ 0 & 0 & 1 \end{pmatrix} \tag{3.54}$$

Quadrupole magnet: A quadrupole magnet with $\varphi = k\sqrt{|k|}$ and $k > 0$ (horizontal focusing). If $k < 0$, then M_x and M_z are just interchanged (vertically focusing).

$$M_x = \begin{pmatrix} \cosh\varphi & \frac{1}{\sqrt{|k|}} & 0 \\ \sqrt{|k|}\sinh\varphi & \cosh\varphi & 0 \\ 0 & 0 & 1 \end{pmatrix} M_y = \begin{pmatrix} \cos\varphi & \frac{1}{\sqrt{|k|}} & 0 \\ -\sqrt{|k|}\sin\varphi & \cos\varphi & 0 \\ 0 & 0 & 1 \end{pmatrix} \tag{3.55}$$

The bending dipole:

The bending radius of a dipole is given by $\rho = \frac{m_0 c\beta\gamma}{qB}$ and the transformation matrix yields:

$$M_x = \begin{pmatrix} \cos\frac{l}{\rho} & \rho\sin\frac{l}{\rho} & \rho(1-\cos\frac{l}{\rho}) \\ -\frac{1}{\rho}\sin\frac{l}{\rho} & \cos(\rho) & \sin\rho \\ 0 & 0 & 1 \end{pmatrix} \tag{3.56}$$

The solenoid magnet:

The solenoid magnet's transformation matrix can not be derived simply from solving 3.52. For a deeper understanding of the dynamics in a solenoid [8] is highly recommended. A linear transformation matrix in the hard edge approximation is with $\phi = l/r$ and $r = p/(qB_0)$:

$$M = \begin{pmatrix} \frac{1+\cos\phi}{2} & r\sin\phi & \frac{\sin\phi}{2} & r(1-\cos\phi) \\ -\frac{\sin\phi}{4r} & \frac{1+\cos\phi}{2} & -\frac{1-\cos\phi}{4r} & \frac{\sin\phi}{2} \\ -\frac{\sin\phi}{2} & -r(1-\cos\phi) & \frac{1+\cos\phi}{2} & r\sin\phi \\ \frac{1-\cos\phi}{4r} & -\frac{\sin\phi}{2} & -\frac{\sin\phi}{4r} & \frac{1+\cos\phi}{2} \end{pmatrix} \tag{3.57}$$

The mixed terms in 3.57 are what makes a solenoid the tedious structure it is, despite its very powerful focusing. It introduces coupling between the planes. So any alignment or steering error in one plane, automatically leads to an off-axis beam in both planes after the solenoid. It also introduces emittance-exchange.

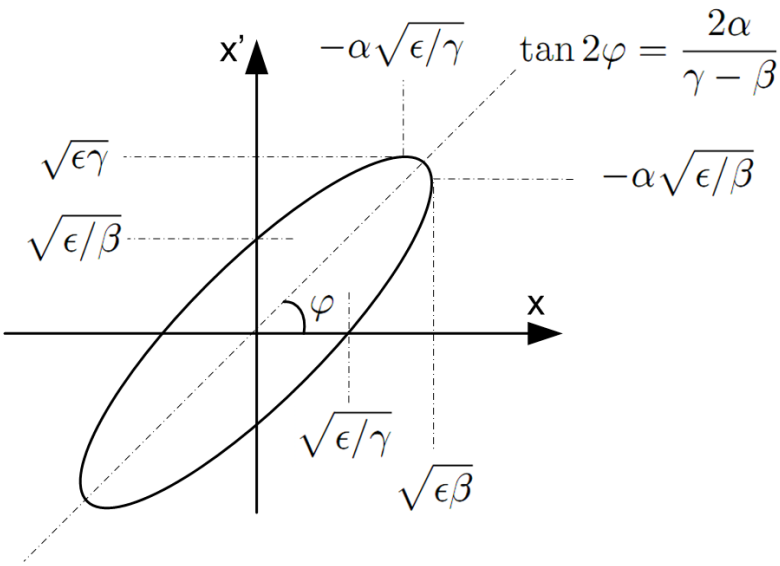

Figure 3.6: Beam properties represented by Twiss parameters [9]

3.3.2 Emittance, Phase-Space and Liouville-Theorem

So far, all the concepts that have been represented are very useful for single particle problems. A beam on the other hand consists of many particles (10^{5-12}). So a statistical approach is unavoidable. So instead of analyzing each particle separately, an entire ensemble is taken into account. In a linear theory a particle distribution is a Gaussian. Under the assumption that coupling is not present each plane can individually be described by a 2D Gaussian.

$$f(\boldsymbol{x}) = A\exp(-\boldsymbol{x}^T\boldsymbol{\Sigma}\boldsymbol{x}) \tag{3.58}$$

where Σ is the covariance matrix.

$$\Sigma = \begin{pmatrix} xx & xx' \\ x'x & x'x' \end{pmatrix} = \begin{pmatrix} \beta\epsilon_x & \alpha\epsilon_x \\ \alpha\epsilon_x & \gamma\epsilon_x \end{pmatrix} \tag{3.59}$$

with

$$\det(\Sigma) = \epsilon_x^2 \tag{3.60}$$

The right hand side of equation 3.59 describes an ellipse using the parameters α, β, and γ and is an alternative represenation to equation 3.61. These are the so called "Twiss-parameters" and they represent statistical properties of the distribution.

$$\pi\epsilon = A = \gamma x^2 + 2\alpha xx' + \beta x'^2 \tag{3.61}$$

The area of the ellipse divided by π is called the "emittance" and is one of the most important parameters in accelerator physics. In figure 3.6 [9] one can see the relation between Twiss parameters and measurable quantities.

Liouville's Theorem

In a conservative system, Liouville's theorem is one of the key statements. It states that in a conservative system the phase-space-volume is a conserved quantity. More strictly it states, that in a small area around a given point in phase space, the system-point density remains constant through time. In terms of accelerator physics this means, that the emittance is a conserved quantity. The shape and orientation of the phase-space-ellipse may change, but its total area does not. For the derivation of this theoerem the following effects were not included:spacecharge-effects,synchrotron-radiation, beam-cooling, mismatching, and various other effects. If any of these effects is present, the Liouville theorem no longer applies. In a LEBT (low energy beam transport) the spacecharge-force is the dominant effect which increases emittance. Some work of this thesis was performed in a low energy region

This theorem allows one to find transformation matrices which can then be used to calculate the evolution of the Twiss-parameters at any desired point. All it requires is to find matrices which leave the emittance invariant.

$$\epsilon = \gamma x^2 + 2\alpha x x' + \beta x'^2 = \gamma_0 x_0^2 + 2\alpha_0 x_0 x_0' + \beta_0 x_0'^2 \tag{3.62}$$

The evolution of Twiss parameters can then again be described by matrix-multiplication.

3.4 The Radio Frequency Quadrupole

A radio frequency quadrupole (RFQ) is a special type of linear rf accelerator. It is used for low particle velocities ($\beta = 0.01...0.06$) and as such plays an important role in the acceleration of ions. It can be used as a stand-alone accelerator or as a pre-accelerator for adjacent accelerating structures like a drift-tube-linac. It consists of 4 vanes of which are connected to an RF power supply such that two opposite vanes are on positive, while the other two are on negative potential and vice-versa. The RFQ structure was first presented in 1969 by Kapchinkskiy and Tepliakov.[10] The proposed shape of the vanes was in such a way that an RFQ could be used for acceleration, bunching and transversal focus at the same time. Combining these three features into one compact machine made it the important structure it is today. Before giving a mathematical description of the field and beam dynamics, a qualitative approach to the functionality of an RFQ is chosen.

An RFQ consists of four parallel placed vanes or rods. The opposite vanes have the same charge, while adjacent vanes have opposite charge. The electric field of a quadrupole can be seen in figure 3.7. Since and RFQ is a time dependent structure, currents will flow through the vanes leading to magnetic fields. The magnetic forces in an RFQ are very low in comparison to the electric, because of the low β of the particles and are therefore negligible. If a particle beam is sent through the four vanes, off center particles will experience a net non-zero force and will be pushed back towards the center whilst particles on axis will remain on axis. If all vanes are uniform cylinders, the electric field will have no longitudinal component and

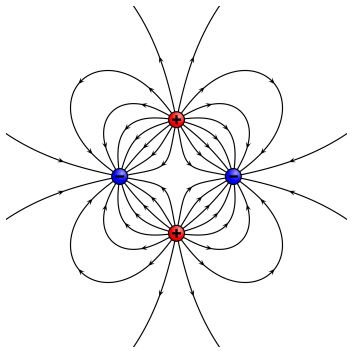

Figure 3.7: electric field of a quadrupole [11]

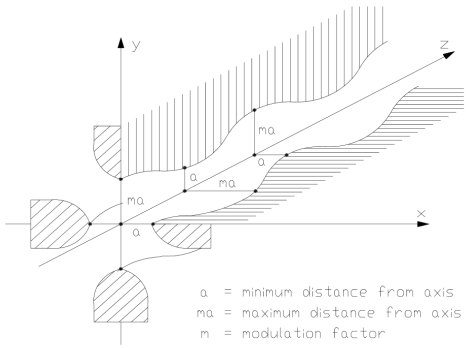

Figure 3.8: Electrode modulation and displacement. [12]

there will be no acceleration. So Kapchinkskiy and Tepliakov introduced sinusoidal modulation and displacement of the electrodes (see figure 3.8).

This perturbation of the geometry introduced an axial field component that enables the RFQ to bunch and accelerate the beam. The modulation of the vanes itself is varied over the length of the structure. Its shape defines whether the beam just gets focused, bunched or accelerated. This allows to built an RFQ which contains different stages which are shown in 3.9.

The section presented in 3.9 from left to right are the following:

- A radial matching section. It is used to adapt a incoming DC beam to the alternative field.
- A shaper to transversally focus the beam and to begin adiabatic bunching.
- A gentle buncher to continue the adiabatic bunching.
- The final stage, acceleration.

The mathematical description of a RFQ can be done using the quasi-static approximation. This approximation is valid when the main part of the electromagnetic force originates from the electric charges and the magnetic forces can be ignored [3].

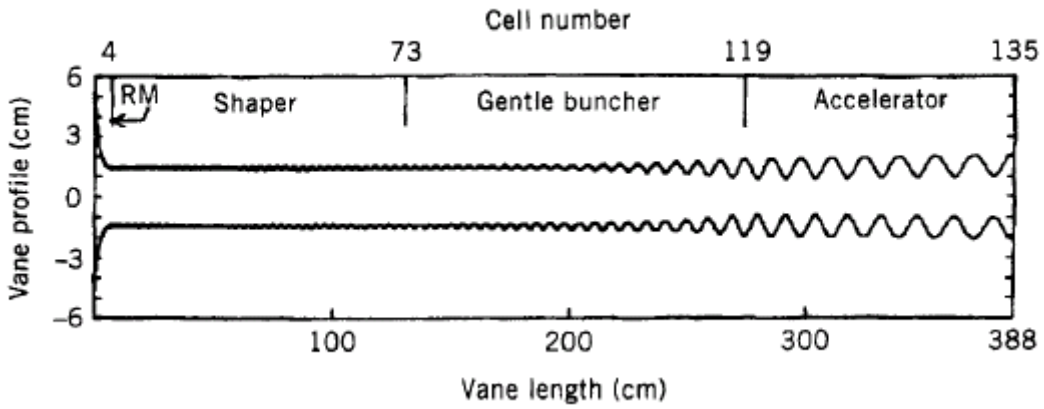

Figure 3.9: RFQ vane-modulation. [3]

This is valid as long as electrode displacements are small compared to the RF wavelength. The time dependent scalar potential can be written in the form of

$$U(r, \Theta, z, t,) = V(r, \Theta, z) \sin(\omega t + \Phi) \tag{3.63}$$

where $\omega/2\pi$ is the RF frequency, Φ is the initial phase of the potential and $V(r, \Theta, z)$ is a solution to the cylindrical Laplace equation.

$$\frac{\partial^2 V}{\partial r^2} + \frac{1}{r}\frac{\partial V}{\partial r} + \frac{1}{r^2}\frac{\partial V}{\partial \Theta^2} + \frac{\partial V}{\partial z^2} = 0 \tag{3.64}$$

To obtain a solution to this problem another approximation is useful. It is assumed that the vane geometry is periodic along the axis. This assumption corresponds to the an acceleration rate which is small compared to the distance a particle travels in one RF period. Or in other words, the vanes do not have a modulation and only the two dimensional quadrupolar solution is of interest. Applying this assumption. The solution to this case is:

$$V(r, \Theta) = \sum_{k=0}^{\infty} A_s r^{2(2s+1)} \cos[2(2s+1)\Theta] \tag{3.65}$$

In case this approximation is not valid and the vanes are modulated along the z-axis, which causes particle acceleration one obtains:

$$V(r, \Theta, z) = \sum_{n=1}^{\infty}\sum_{s=0}^{\infty} A_{ns} I_{2s}(knr) \cos(2s\Theta) \sin(knz) \tag{3.66}$$

Adding both solutions gives:

$$V(r, \Theta, z) = \sum_{k=0}^{\infty} A_s r^{2(2s+1)} \cos[2(2s+1)\Theta] + \sum_{n=1}^{\infty}\sum_{s=0}^{\infty} A_{ns} I_{2s}(knr) \cos(2s\Theta) \sin(knz) \tag{3.67}$$

Equation 3.67 is the general K-T potential and is used to calculate the electric field around the beam ($I_{2s}(knr)$ are the modified bessel functions and A are constants defined by the vane geometry). It can be used for any arbitrary vane geometry, but is a rather bulky expression and a simplification would allow a quicker analysis and design process. Kapchinkskiy and Tepliakov decided to only use a two-term-potential function (s=0, n=1) in their original paper. To justify this simplification, they simply chose to adapt the vane geometry in such a way that only the first two terms play a role in the infinite sum.

$$V(r, \Theta, z) = A_0 r^2 \cos(2\Theta) + A_{10} I_0(kr) \cos(kz) \tag{3.68}$$

- A_0 and A_{10} depend on the vane geometry
- $k = \frac{2\pi}{L}$
- $L = \beta_s \lambda$ is the period of the electrode modulation $I_0(\eta) \approx 1 + \frac{\eta^2}{4}$

Now the determination of A_0 and A_{10} is the key factor to this approximation. During an RF-cycle, there will be a time where the voltages on the vanes are $\pm\frac{V_0}{2}$. At $z = 0$ the potential on the horizontal vane ($\Theta = 0$)

$$\frac{V_0}{2} = A_0 a^2 + A_{10} I_0(ka) \tag{3.69}$$

For the vertical vane ($\Theta = \pi/2$) the potential function becomes

$$-\frac{V_0}{2} = -A_0 (ma)^2 + A_{10} I_0(kma) \tag{3.70}$$

Solving 3.69 and 3.70 for A_0 and A_{10} gives:

$$A_0 = \frac{V_0}{2a^2} \frac{I_0(ka) + I_0(kma)}{m^2 I_0(ka) + I_0(kma)} \tag{3.71}$$

and

$$A_10 = \frac{V_0}{2} \frac{m^2 - 1}{m^2 I_0(ka) + I_0(kma)} \tag{3.72}$$

Introducing the dimensionless constants

$$X = \frac{I_0(ka) + I_0(kma)}{m^2 I_0(ka) + I_0(kma)} \tag{3.73}$$

$$A = \frac{m^2 - 1}{m^2 I_0(ka) + I_0(kma)} \tag{3.74}$$

allows to write the time dependent two-term-potential function in a compact manner

$$U(r,\Theta,z,t) = \frac{V_0}{2}\left[X((\frac{r}{a})^2\cos(2\Theta) + AI_0(kr)\cos(kz)\right]\sin(\omega t + \Phi) \tag{3.75}$$

or in Cartesian coordinates:

$$U(x,y,z,t) = \frac{V_0}{2}\left[\frac{X}{a^2}(x^2 - y^2) + AI_0(kr)\cos(kz)\right]\sin(\omega t + \Phi) \tag{3.76}$$

From 3.76 we can easily derive the electric fields using $\vec{E} = -\vec{\nabla}U$ which yields:

- $E_x = -\frac{XV_0}{a^2}x - \frac{kAV_0}{2}I_1(kr)\frac{x}{r}\cos(kz)\sin(\omega t + \Phi)$
- $E_y = \frac{XV_0}{a^2}y - \frac{kAV_0}{2}I_1(kr)\frac{y}{r}\cos(kz)\sin(\omega t + \Phi)$
- $E_z = \frac{kV_0A}{2}I_0(kr)\sin(kz)\sin(\omega t + \Phi)$

The E_z-component is responsible for acceleration and bunching. The first term in both the x and y component represents the transversal focusing provided by the quadrupole field. The second term in both components leads to the transversal RF-defocusing force which acts when the vane modulation is a such that longitudinal focusing occurs. The dimensionless constants A and X can now be called acceleration and focusing efficiency. At this point it becomes very clear that the modulation is the key factor in the design of an RFQ. For example when $m = 1$ then $A = 0$ and the RFQ becomes a transferline that provides no acceleration at all. For $m \neq 1$ the energy gain of a particle is simply

$$\Delta W = \frac{qkAV_0I_0(kr)}{2}\int_0^l \sin(kz)\sin(k'z + \Phi)dz \tag{3.77}$$

In 3.77 ωt was replaced by $2\pi z/\beta'\lambda$, $k' = 2\pi/\beta'\lambda$, $k = 2\pi/\beta_s\lambda$ and $l = \beta_s\lambda/2$. The acceleration has a maximum when a particle travels from one centre of a cell to the next in exactly half a RF-period. This particle then satisfies the synchronous condition and is called the synchronous particle. Synchronism requires $\beta' = \beta_s$ then ΔW becomes:

$$\Delta W = \frac{q\pi AV_0I_0(kr)\cos(\Phi)}{4} \tag{3.78}$$

Φ is called the particle or synchronous phase and for $\Phi = 0$ the field is at a peak value. Introducing the average axial field

$$E_0 = \frac{1}{l}\int_0^l E_z dz = \frac{2AV_0}{\beta\lambda} \tag{3.79}$$

and calculation the time-transit-factor T

$$T = \frac{\int_0^l E_z\sin(kz)dz}{\int_0^l E_z dz} = \frac{\pi}{4} \tag{3.80}$$

gives for 3.78

$$\Delta W = qE_0 T I_0(kr) l \cos\Phi_s \tag{3.81}$$

The next interesting step is to analyze the particle dynamics in the RFQ. Similar to 3.1 longitudinal phase-space is of concern at first. Substracting the energy gain of the synchronous particle W_s from the energy gain of any particle and differentiating by dz one obtains

$$\frac{d(W - W_s)}{dz} = qE_0 T\big[I_0(kr)\cos(\Phi) - \cos(\Phi_s)\big] \tag{3.82}$$

For the evolution of the the difference in phase one immediatly finds:

$$\frac{d(\Phi - \Phi_s)}{dz} = -\frac{2\pi(W - W_s)}{mc^2\beta_s^3\lambda} \tag{3.83}$$

The transverse particle dynamics require a bit more effort. Using the x and y component of the electric field, one can derive the equations of motion in the transversal plane. The non-relativistic equation of motion for a particle of mass m, charge q and small displacement from the axis in the horizontal plane is:

$$\ddot{x} + \left(\frac{qXV_0}{ma^2} + \frac{qk^2AV_0}{4m}\cos(kz)\right)x\sin(\omega t + \Phi) = 0 \tag{3.84}$$

Using the fact that $kz = \omega t$ and that

$$\cos(\omega t)\sin(\omega t + \Phi) = \frac{\sin(\Phi) + \sin(2\omega t + \Phi)}{2} \tag{3.85}$$

The second term in 3.85 with double the RF frequency averages to 0 since the synchronous particle travels through one unit cell in half the RF period. So 3.84 becomes

$$\ddot{x} + \left[\frac{qXV_0}{ma^2}\sin(\omega t + \Phi) + \frac{qk^2AV_0}{8m}\sin(\Phi)\right]x = 0 \tag{3.86}$$

This equation has the form of the Matthieu-equation. A solution to this problem can be found considering the a trial solution of the form:

$$x = (C_1\sin(\Omega t) + C_2\cos(\Omega t))[1 + \epsilon\sin(\omega t + \Phi)] \tag{3.87}$$

C_1 and C_2 are constants. Ω and ϵ are new parameters, where $\Omega \ll \omega$ and $\epsilon \ll 1$. The term in the parenthesis varies slowly over a unit-cell and represents the smooth betatron-oscillation with the betatron-frequency Ω. The term in the square brackets varies with the RF-frequency and is called the flutter factor. Choosing $C_1 = 1$ and $C_2 = 0$ for simplicity and inserting 3.87 into 3.84 and ignoring terms of order $O(\omega^-1)$ equation 3.84 becomes:

$$\ddot{x} \approx -\epsilon\omega^2\sin(\Omega t)\sin(\omega t + \Phi) \tag{3.88}$$

Inserting equation 3.87 into the original Mathieu equation and averaging over one RF-period it becomes clear, that the average particle displacement can be described as a harmonic oscillator.

$$\ddot{\bar{x}} + \Omega^2 \bar{x} = 0 \tag{3.89}$$

with

$$\Omega^2 = \frac{1}{2}\left(\frac{qXV_0}{m\omega a^2} + \frac{qk^2 V_0 A \sin(\Phi)}{8m}\right) \tag{3.90}$$

The first term in 3.90 represents the quadrupole focusing in a RFQ and the second term the RF defocusing. It is common to express 3.90 as a measure of phase advance per focusing period using $\sigma_0 = \Omega\lambda/c$:

$$\sigma_0^2 \approx \frac{1}{8\pi^2}\left(\frac{qXV_0\lambda^2}{mc^2a^2}\right)^2 + \frac{\pi^2 qV_0 A \sin(\Phi)}{2mc^2\beta^2} \tag{3.91}$$

For a stable particle motion it is required that $\sigma_0^2 > 0$, because otherwise the solution to equation 3.89 would an exponential with un-restrained growth. Linear accelerators, like a DTL, require a bunched beam. Bunching can be aquired using RF cavities which decelerate particles ahead of the synchronous particle and accelerate the particles which travel behind it. Going through a drift all the particles will move closer together and form a bunch. Unfortunately this process is not very efficient, especially for high current beams, because it increases the particle density and therefor the spacecharges, which then leads to a blow-up of transverse emittance. With an RFQ on the other hand, the bunching process can be done adiabatically by slowly changing the modulation of the vanes, which resolves these problems to a very large extent. Controlling the bunching process can be done with the right modulation of the vanes and the sychronous phase (which is controlled by the center-to-center spacing of the unit-cells).

4 Injector Test Stand

4.1 purpose

The purpose of the MedAustron Injector Test Stand (ITS) at CERN is to test and validate the choice of different structures and components in preparation for a complete Injector [1] installation and commissioning in its final configuration in Wiener Neustadt, Austria. ITS activities provide a good training and valuable experience to the MedAustron personnel to ensure efficient machine installation and commissioning in Wiener Neustadt. Different technical and/or conceptual issues can be identified well in advance.

The installation and tests of different beam-line elements have been done according to the ITS schedule [2], which was mainly defined by the availability of different elements and systems. The beam measurements and data analyses were performed in January-December 2012.

4.2 Beam-line description and functional specifications

4.2.1 Beam-line composition

- Electron Cyclotron Resonance (ECR) Ion Source generating C^{4+} and H_3^+ beams
- 90 degrees spectrometer dipole for ion species separation (filtering)
- Low Energy Beam Transport (LEBT) line, comprising quadrupole triplet, solenoid and steering magnets for beam focusing and trajectory correction, various Beam Diagnostics devices and a fast electrostatic deflector (EFE)
- Radio Frequency Quadrupole (RFQ) Linac
- two Test Benches (TB1 and TB2) consisting of Beam Diagnostics monitors

The buncher which is displayed in 4.1 was not installed in the actual test-setup, due to delays in the manufacturing process. It will be tested at a later point at the MedAustron facility.

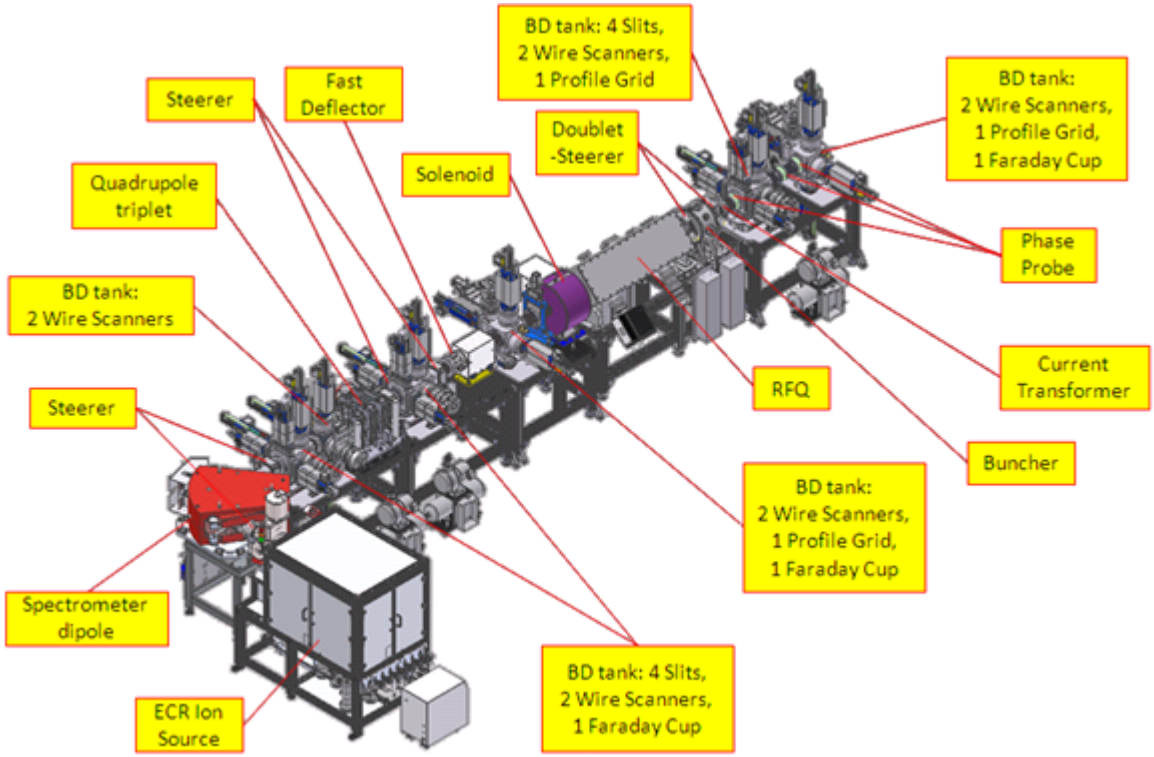

Figure 4.1: ITS basic layout

4.2.2 ECR ion source

The main components of the MedAustron ECR Ion Source [3] are depicted in 4.2 and its main characteristics are summarized in Table 1. It is a commercially available Supernanogan Ion Source from PANTECHNIK. The operation principle of the MedAustron ECR Ion Source is the following:

- Microwaves are employed in a confinement volume (plasma chamber) to generate plasma from a gas mixture injected into the plasma chamber in a controlled manner.
- The confinement of the generated plasma is ensured by a magnetic field resulting from the superposition of a hexapole magnet and two solenoid magnets field (all of them being permanent magnets).
- The charged particles are extracted from the plasma chamber by using a system of electrodes (the extraction system) polarized at a high electric potential (24 kV nominal).

The Ion Source is generating a DC beam, however, if necessary, the beam can also be pulsed by pulsing the RF generator.

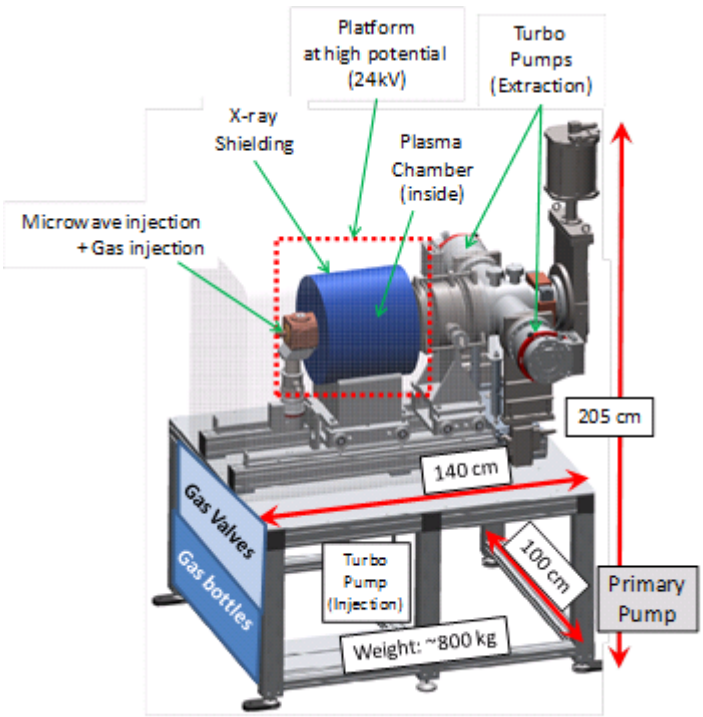

Figure 4.2: PANTECHNIK ECR ion source

Parameter	Value	Unit	Comment
Nominal ion species	C_{12}^{4+},H_3^+	-	For clinical use
Injected gas for C_{12}^{4+} operation	CO_2 and He	-	
Injected gas for H_3^+ operation	H_2	-	
Nominal extraction voltage	24	kV	
Max extraction voltage	30	kV	
Nominal beam energy	8	keV/u	for nominal ion species
Max beam current from source	<6	mA	for complete spectrum of extracted ions
Nominal beam current	0.2 C_{12}^{4+}, 0.5 H_3^+	mA	at the exit of the spectrometer
Nominal emittance	180	$\pi.mm.mrad$	At the exit of the spectrometer dipole, for the beam fraction containing the nominal current

Table 4.1: ECR parameters

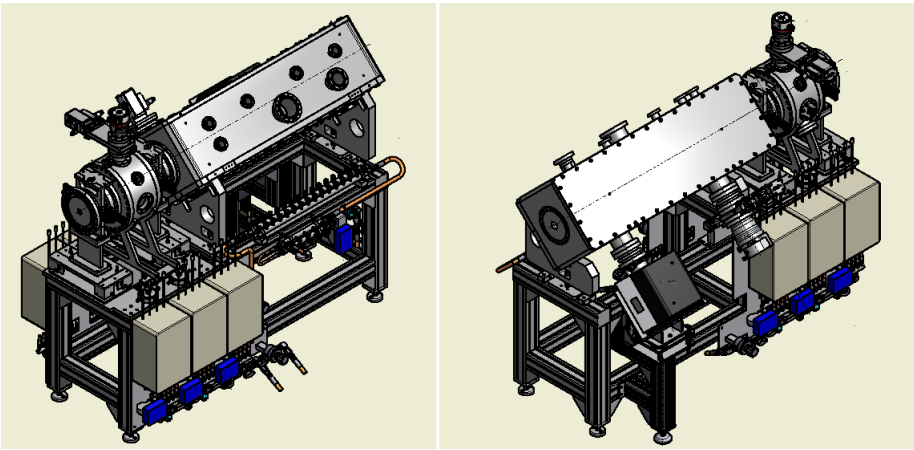

Figure 4.3: RFQ and IMS

Parameter	**Value**	**Unit**
Operation frequency	216.816	MHz
Nominal electrode voltage	70	kV
Input beam energy	8	keV/u
Output beam energy	400	keV/u
Max design beam current	1	mA
Max pulse length	500	μs
Max repitition rate	10	Hz
Max duty factor	1/200	-

Table 4.2: main RFQ parameters

4.2.3 Radio Frequency Quadrupole and Inter-tank Matching Section

The 1.33 m long four-rod RFQ tank (see 4.3) is made of thick stainless steel plates with copper plated inner side. The base plate and the stems are made of copper and are water cooled. In general negligible X-ray emissions are expected from the RFQ during the nominal operation, which is not the case during the RF conditioning. The main characteristics of the RFQ are summarized in 4.2.

The Inter-tank Matching Section (IMS) consists of two Doublet-Steerer magnet units and a bunching cavity. The main parameters of the IMS are summarized in Table 3 and 4.

Parameter	**Value**	**Unit**
Quadrupole effective length	50	mm
Quadrupole max integrated gradient	4.9	T
Steerer effective length	27	mm
Max repition rate	5	Hz
Beam aperture diameter	18	mm

Table 4.3: Main parameters of the Doublet-Steerer unit

Parameter	**Value**	**Unit**
Operating frequency	216.816	Mhz
Effective gap voltage	100	kV
RF phase	-90	degree
Max pulse length	500	μs
Max repition rate	10	Hz
Max duty factor	1/200	-
Beam pipe aperture diameter	18	mm

Table 4.4: Main parameters of the Doublet-Steerer unit

4.2.4 Beam Diagnostics

Different types of Beam Diagnostics monitors are used in the beam-line for DC and pulsed beam measurements:

- Faraday Cups (FCN) are used for DC (type A) and pulsed (type B) beam current measurements. The acquisition rate is up to 10 kHz.
- Wire Scanners (WSX) are used for DC beam profile and position measurements. The position measurement accuracy is 100 μs, which is defined by the thickness of the wire.
- Combined horizontal and vertical beam Profile Grids (PGX) are used for pulsed beam profile and position measurements.
- A pair of Slit plates (SLX) in horizontal plane is used for selection of the ion species of interest. Horizontal and Vertical Slits are also used at different locations for beam emittance measurements in combination with Wire Scanners or Profile Grids.
- Beam current transformers (CTA) are used for pulsed beam current measurements (type A in the LEBT, type R in the exit flange of the RFQ, type C in the Test Bench 2).
- Beam Phase Probes (PHP) are used in the Test Bench 2 for beam energy measurements using Time-of-Flight method.

The complete list of the BD monitors at ITS can be found in Annex 1.

4.2.5 Test Benches

Two temporary Test Benches (TB1 and TB2) containing Beam Diagnostics monitors are used for the beam measurements. TB1 is used at the end of the LEBT to measure and prepare the beam at the matching plane of the RFQ. TB2 is used at the end of the RFQ (with and without IMS) to measure the beam parameters at the exit of the RFQ.

TB1

The TB1-stage is meant to measure the mean in the RFQ input plane to check for steering, matching and LEBT transmission. It is very crucial point of measurement because the quality of the beam in TB1 is a key factor in the performance of the RFQ. Figure 4.4 are drawings of the diagnostic tanks used in TB1 from different perspectives. TB1 provides beam profiles, current, and emittance measurements.

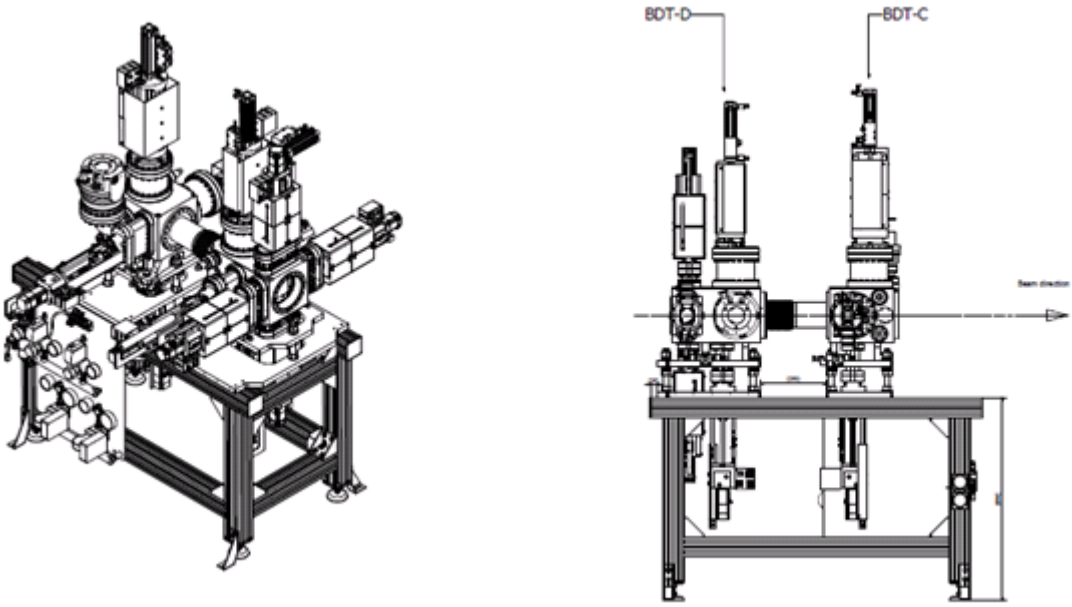

Figure 4.4: Test Bench 1

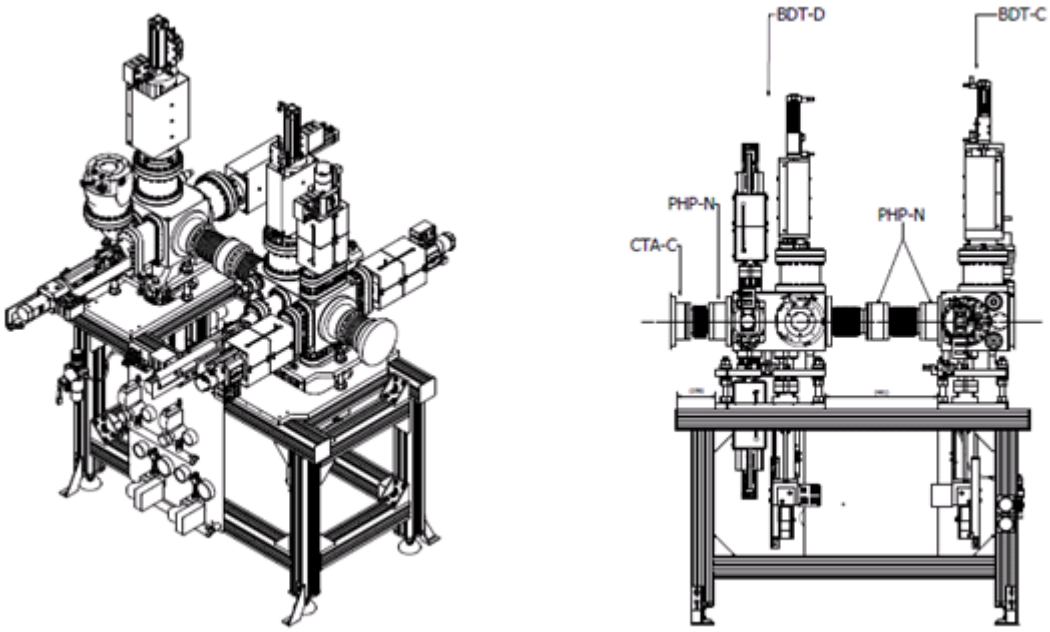

Figure 4.5: Test Bench 2

TB2

TB2's purpose is to analyse the beam at the output of the RFQ. It has all the necessary equipment to measure a bunched an accelerated beam: current transformers (CTA-C), 3 phase probes for TOF-measurements, emittance slits, a profile grid (PGX) for live beam profiles and emittance measurement (combined with the slits) and a high frequency Faraday-Cup (FCN-B) for current measurements. In Figure 4.5 on can still see the wire scanners which were initially planned, but during the process of implementation were decided to be removed.

4.2.6 Measurement stages

The beam measurements at the ITS are planned in three main stages (see Figure 6 and 7) as described below.

- Stage 1
  ECR Ion Source performance optimization including the 90 degree spectrometer dipole and using the BD monitors in two diagnostics tanks TS-01-000-BDT-D and TS-01-001-BDT-A. The nominal beam energy is 8 keV/u. The beam current, profile and emittance are measured. The beam is steered on axes using two combined horizontal and vertical steering magnets MCX-A and two Wire Scanners.

- Stage 2
  Beam transport and measurements in the LEBT up to the entrance of the RFQ using the TB1 in place of the RFQ. The nominal beam energy is 8 keV/u. At this stage the RFQ is not yet installed in the beam-line. The beam current, profile and emittance are measured along the LEBT and in the TB1. The beam is steered on axes using two combined horizontal and vertical steering magnets MCX-A and two Wire Scanners. The beam-line is optimized to minimize the emittance growth, beam losses and to match the beam to the RFQ.

- Stage 3
  RFQ commissioning with beam using a spectrometer dipole and TB2 (with or without IMS). The beam is accelerated from 8 to 400 keV/u in the RFQ. The beam transmission through the RFQ is optimized by fine tuning the settings of the magnets in the LEBT. The beam energy at the exit of the RFQ is measured using a spectrometer dipole. The beam current, profile and emittance are measured in TB2. Time-of-Flight beam energy measurements were planned using PHPs in TB2, however were not performed due to the unavailability of the IMS.

- Stage 4
  The RFQ is first installed in a temporary location for RF conditioning before

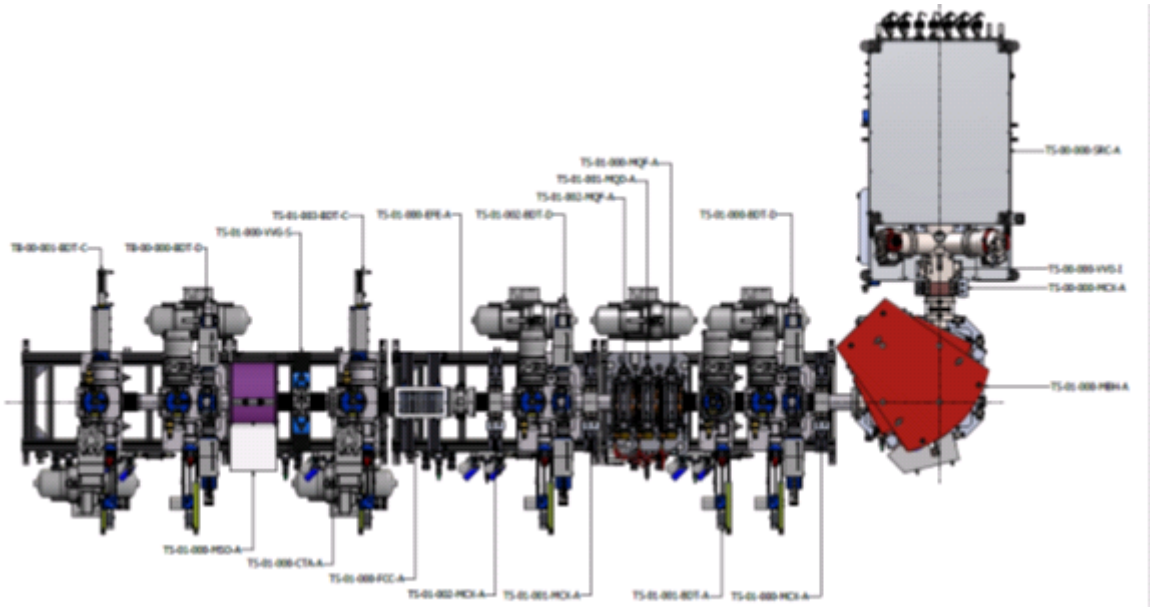

Figure 4.6: ITS layout, measurement stage 1 and stage 2

Stage 3. The RF conditioning is done by gradually increasing the RF power coupled into the RFQ while monitoring the vacuum pressure in the tank. During the RF conditioning the X-ray emissions from the electrodes increase and have to be shielded and monitored.

4.3 Theoretical studies, simulation, and measurements

This section presents theoretical studies and simulations of the ITS beam-line in preparation for the beam measurements. Preliminary beam parameters measured at the exit of the spectrometer dipole in Stage 1 are used as an input for the beam simulations, which in their turn provide preliminary magnet settings and expected beam parameters at different measurement points in the beam-line. Beam parameters like beam current, profile and emittance are measured and compared to the theoretically expected values. Beam-line settings are then fine-tuned to optimize the beam performance and to reduce beam losses. The procedure requires a combination of different programs and algorithms. Simulation codes Trace3D, Path Manager, Delta, PlotWin, GenBeam and MedAustron's own Emittance Analysis Application (EAA) software were used in this process. The raw measurement data was treated to filter the measurement noise using EAA and then processed in GenBeam to generate a best fit particle distribution, which is then imported into Path Manager to track the beam through the entire ITS beam-line. The routine Delta, which is normally used for error studies, was used to find quadrupole gradients and

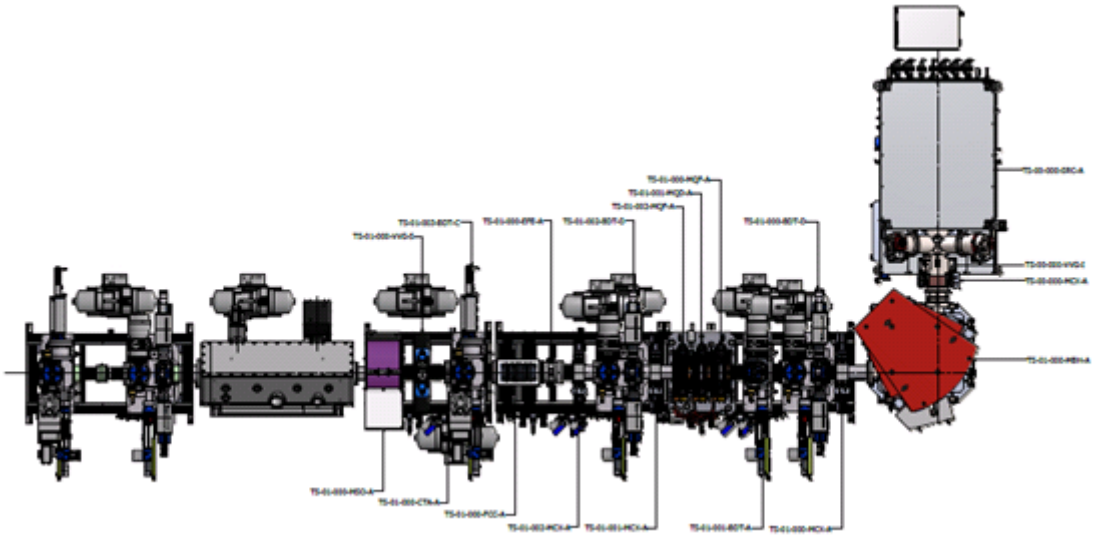

Figure 4.7: ITS layout, stage 3

solenoid field strengths to match the beam to the RFQ. The detailed process of matching, which also involved Trace3D, is not within the scope of this note.

4.3.1 Preliminary measurements

The basis for this section is the emittance measurement, which is performed directly after the spectrometer. It is used to generate a particle distribution, which is then tracked through the entire beam-line up to the RFQ. The matching procedure (i.e. finding correct settings for MQZ and MSO) is also based on this measurement. Also, the factory requirements towards the source can be checked. The ion source configuration can be found below and was kept constant throughout all the measurements which were performed. Ion Source configuration:

- HV: 24 kV
- Focus electrode voltage: 1.9 kV
- Puller electrode voltage: 0 V
- RF generator frequency: 14.486 GHz
- RF attenuation: -20.80 dBm
- Gas flow: 55
- Extraction system position: 0 mm
- Tuner position: 2.48 mm

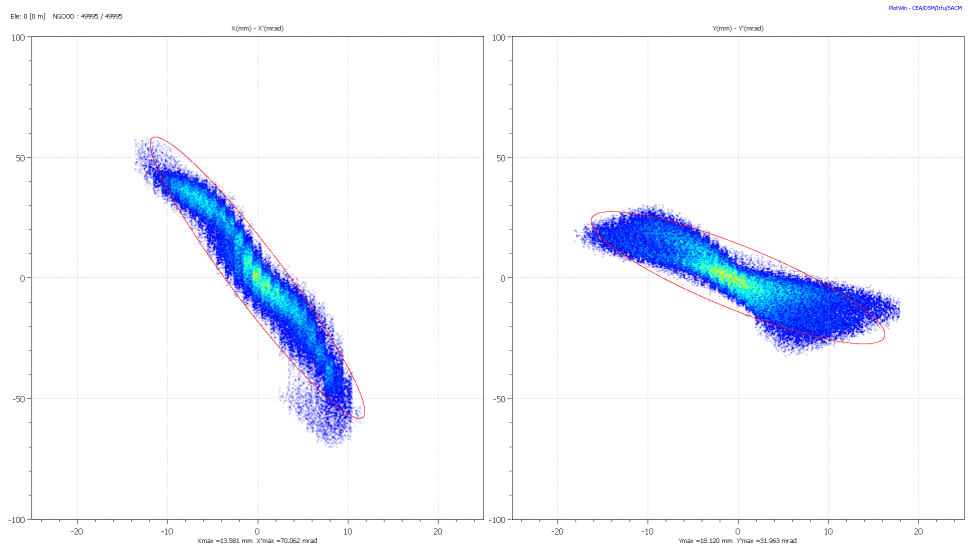

Figure 4.8: phase space measurement at the first BDT

Phase space	α**[1]**	β**[mm/mrad]**	ϵ_{RMS}	$\epsilon_{90\%}$
XX'	3.11	0.67	42.65	176.5
YY'	1.67	1.16	45.87	209.24

Table 4.5: measured beam parameters after the spectrometer

In Table the measured beam parameters are given. GenBeam was used to generate a macro-particle beam that is used for further simulation. This distribution was also imported into PlotWin for analysis. All data corresponds to a 598 μA beam.

The requirement specified tot he source producer (Pantechnik) is 500 μA of H_3^+ and 200 μA of C_{12}^{4+} in 180 $\pi.mm.mrad$ and has been confirmed by measurements. See Figure 4.9.

4.3.2 Beam Tracking

Using the measurements, which were presented in section 4.3.1 the beam is tracked through the LEBT up to the RFQ. It is of course of high interest to predict the measurements at BD monitors downstream the line. The computer code Path Manager was used for beam simulations. The code offers the possibility to export beam data at any desired element so that it is possible to compare simulation and measurement at any point in the line. This was done at TS01002BDT.

Figure 4.10 shows the expected beam distributions in both transverse planes at TS01002BDT. The beam parameters can be found in Table **??**.

One of the important parameters of the beam is its emittance and its development throughout the accelerator. Figure 4.11 displays the development of the transverse RMS emittance through the LEBT, starting behind the spectrometer and ending at

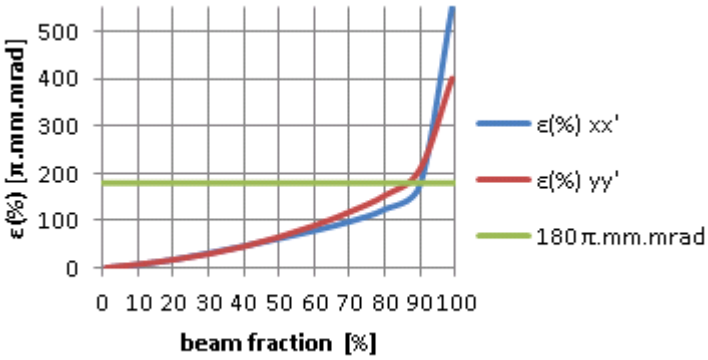

Figure 4.9: Measured beam emittance as a function of beam fraction at TS-01-000-BDT-D

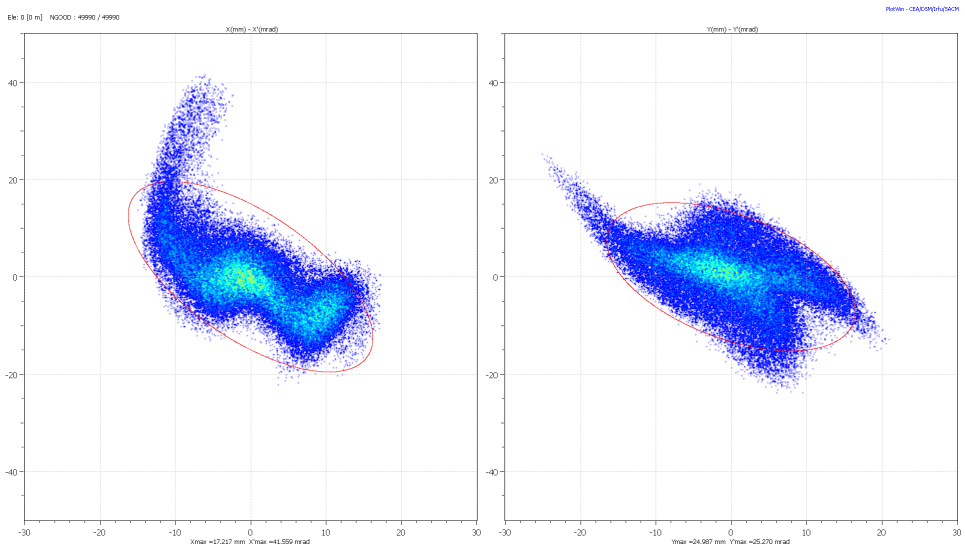

Figure 4.10: Simulated beam distributions at TS01002BDT, TS01004SLH, TS01006SLV

	$\alpha[1]$	$\beta[mm/mrad]$	$\epsilon_{RMS}[\pi.mm.mrad]$
XX'	0.83	1.07	48.74
YY'	0.56	1.24	44.05

Table 4.6: Simulated beam parameters at TS01002BDT

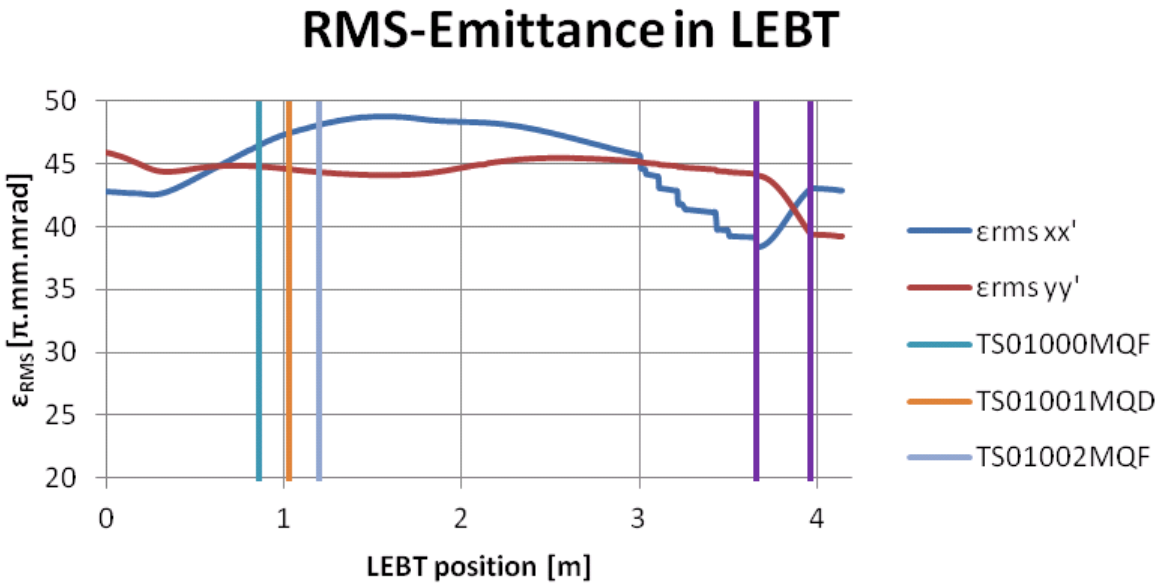

Figure 4.11: RMS emittance along the LEBT up to the RFQ

the RFQ input plane. The purple lines in the plot represent the (optical) beginning and end of the solenoid magnet. The emittance in the horizontal plane increases in comparison to the vertical one. This is not surprising when one takes a closer look at the distribution measured behind the spectrometer. One can find two spatially separated maxima in the beam. These maxima will in the future be referred to as "beamlets". The space charge forces in the horizontal plane have a stronger effect than in the vertical, where just one maximum is found. At around 3 meters the horizontal emittance begins to drop stepwise, but this is only caused by losses. By comparing Figure 11and Figure 12 one can immediately see that the losses correlate with the shrinking of the emittance. What is very clear to see in Figure 11, is the emittance exchange that occurs in the solenoid. Due to non-zero off-diagonal matrix elements in the transformation matrix of a solenoid, coupling is introduced. This causes exchange between the planes. The 3 lines around the 1m mark are the optical centres of the quadrupole magnets.

4.3.3 Matching

As already mentioned in the introduction the matching procedure is of high importance to transmission rate through the RFQ. The beam mismatch will also generate emittance growth. The procedure itself is not part of this note. The magnetic parameters for the optical elements (quadrupole triplet and solenoid) obtained from the matching procedure are:

These parameters were derived using Trace3D for a first approximation and Path Manager's feature for error studies to obtain results for the measured distribution.

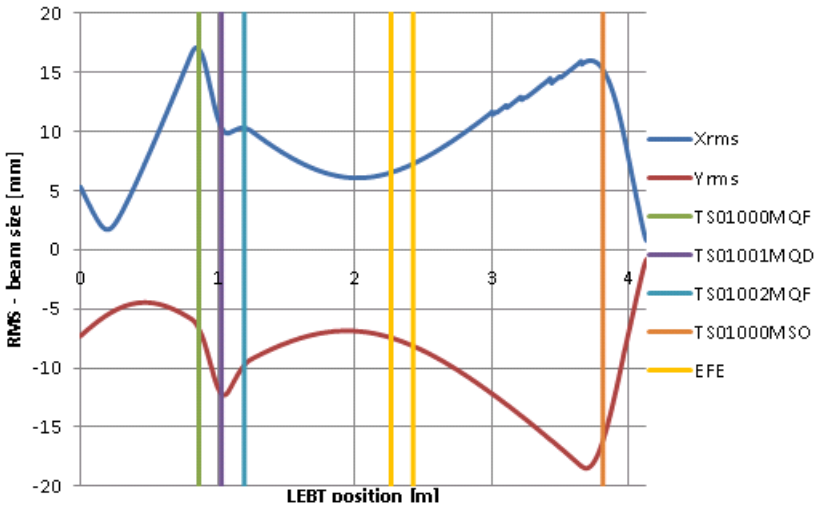

Figure 4.12: RMS beam size, up to RFQ entrance

TS01000MQF: 1.706 T/m $\hat{=}$ 132.4 A
TS01001MQD: -1.88 T/m $\hat{=}$ 149.9 A
TS01002MQF: 0.515 T/m $\hat{=}$ 39.67 A
TS01000MSO: 0.293 T $\hat{=}$ 147.5 A

Table 4.7: Magnetic field parameters for matching

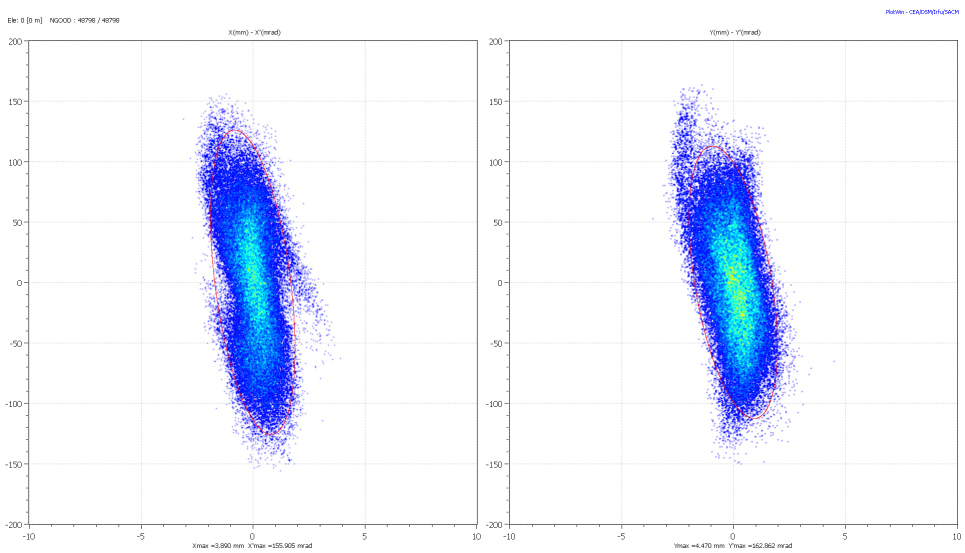

Figure 4.13: Simulated beam distributions at the RFQ input

	$\alpha[1]$	$\beta[mm/mrad]$	$\epsilon_{RMS}[\pi.mm.mrad]$
XX'	0.48	0.0166	42.9
YY'	0.54	0.0198	39.2

Table 4.8: Simulated beam parameters at RFQ input

	$\alpha[1]$	$\beta[cm/rad]$	$\epsilon_{RMS}[\pi.mm.mrad]$
XX'	0.55	1.84	217.0
YY'	0.55	1.84	217.0

Table 4.9: RFQ design input beam parameters given by IAP Frankfurt

All further simulations are based on the parameters given in Table 4.7. According to the simulation the beam after the solenoid (RFQ input)should look like in Figure 14. The corresponding beam parameters can be found in Table 8.

The design parameters at the RFQ input are ?'=0.55, ?=0.0184 mm/mrad in both horizontal and vertical plane. It can be seen that the currently found matching parameters are not optimal. However, even with the distribution seen in Figure 14 a transmission rate of 97.5% through the RFQ is achieved in the simulations using Parmteqm code.

4.3.4 RFQ sensitivity studies

The RFQ requires certain input beam parameters to achieve optimum performance (i.e. high transmission rate, low emittance). Since in reality it is never possible to achieve the perfect parameters, it is important to know the limits in which one can opertate to obtain optimum results. The procedure to analyze the RFQ's behaviour is the following: PARMTEQM uses a 4D waterbag macro particle distribution with uniform phase- and random energy spread, which it tracks through the RFQ. The beam parameters ?, ? and ?of the initial distribution (i.e. at the entrance of the RFQ) can be manipulated simply by editing the input file of PARMTEQM. A script continously varies the input parameters and records transmission and output beam parameters after each run. Only one parameter gets changed at a time. So for example, if one is interested in the behaviour depending on ?, then ? and ? are kept constant at the design values, whilest ? gets varied. The sensitivity to ? (i.e. the acceptance) will be dealt with later in a separate section.

From the output parameters, the so called mismatch factor M [4] can be derived. It is used to give a hint at the increase of the beam size. A mismatch factor of 0.1 corresponds to an increase in beam size of 10%. Since the RFQ efficiency requirement is to have a transmission of 90%, only data which was acquired above 85% will be taken into consideration, to have some margin. Additionally, and only in this section, the unit used for ? is [cm/rad]. The reasons for this are, that PARMTEQM's input

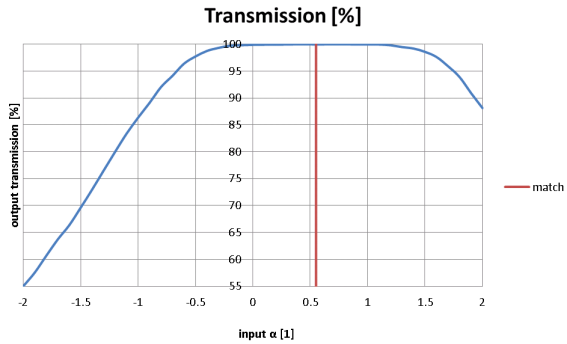

Figure 4.14: RFQ transmission in % depending on input beam α

and output is in [cm/rad] and that the plots become easier to read. The conversion is very simple: 0.01 mm/mrad ? 1 cm/rad.

RFQ sensitivity, α-dependency

3.4.1 RFQ sensitivity, ?-dependency In the following section the RFQ's sensitivity upon variations of the input beam α is studied. Parameters observed at the output of the RFQ are: transmission rate, α, β, and ϵ_{RMS}-growth. The beam parameter α of the RFQ input beam was varied between -2 and +2 for constant β. For this study β was chosen to be 1.84 cm, as it is the matched parameter for this specific RFQ design. The RFQ design α is 0.55. To clarify when the beam is matched to the RFQ a mmatch-lineïs included in all plots . Every plot also shows a curve of the mismatch factor to quantify the effect of the variation of α on beam size after the RFQ. The mismatch factor is plotted on the secondary axis on the right hand side of the plot.

Figure 15 shows the transmission rate depending on α ranging from -2 (highly divergent) up to +2 (highly convergent). Something very basic, but just as important can already be derived from this plot: As long as the beam is converging at the RFQ input plane, the transmission will remain between 90 and 100% over a wide range, which is not surprising taking into consideration that a convergent beam is less likely to hit the aperture unless it is overfocused. The limits for further analysis can also be found. As a lower limit α=-1 is chosen and the upper limit will remain α=+2. So within α = [-1; 2] the effects on the output beam will be analysed.

Figure 16 and Figure 17 display the variation of the output beam parameters depending on the input α in their respective planes. The bandwidth of the variation for $\alpha_{xx'}$ is 0.35 and for $\beta_{xx'}$ 1.2 cm. The maximum mismatch factor M is 0.29 (which corresponds to a beam with 29% increased size in real space!) which was found at α=-0.1. For the vertical plane the bandwidth for $\alpha_{yy'}$ and $\beta_{yy'}$ is 0.22 and 1.91 cm. The maximum mismatch factor M is 0.13 at α=1.6.

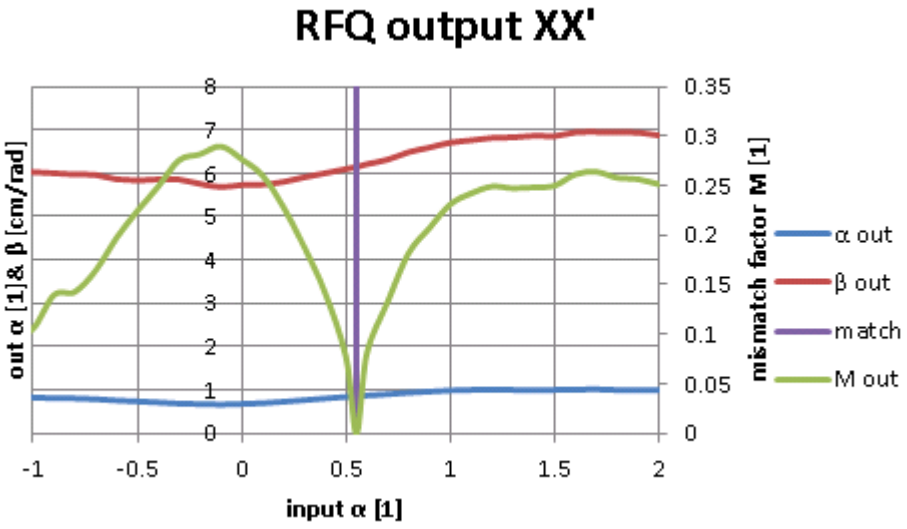

Figure 4.15: RFQ exit parameters for the horizontal plane

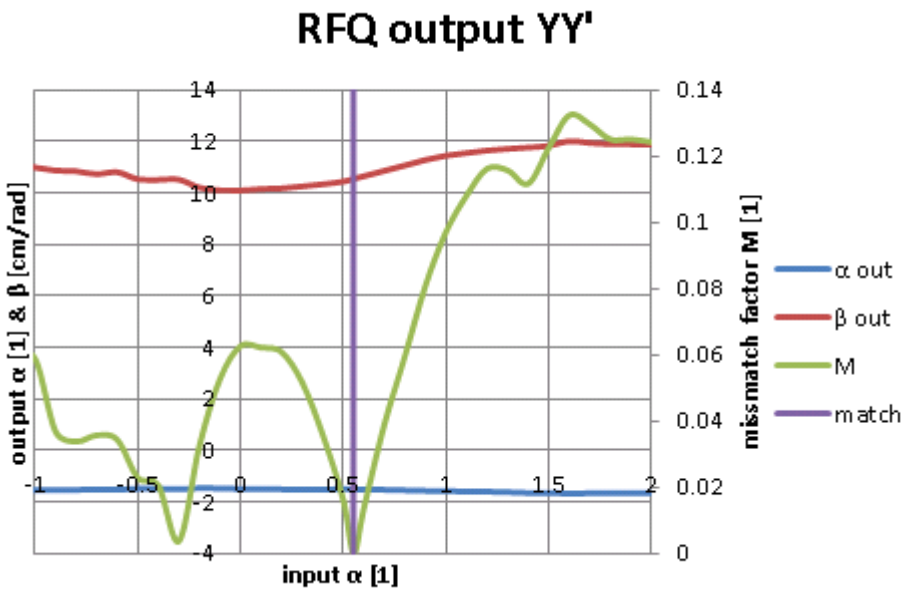

Figure 4.16: RFQ exit parameters for the vertical plane

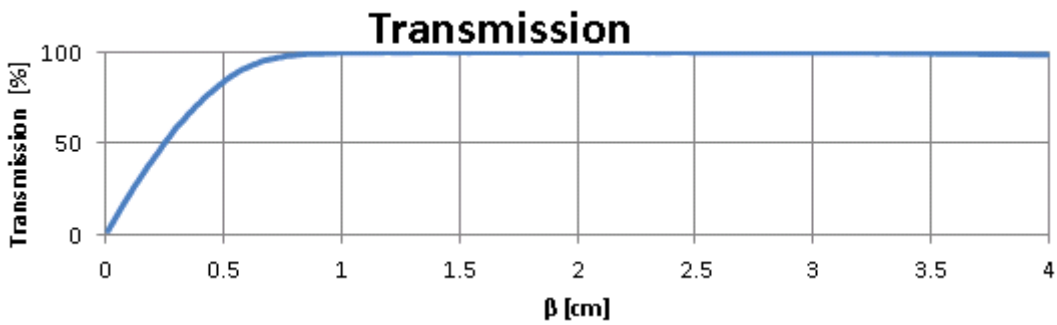

Figure 4.17: transmission rate3depending on β

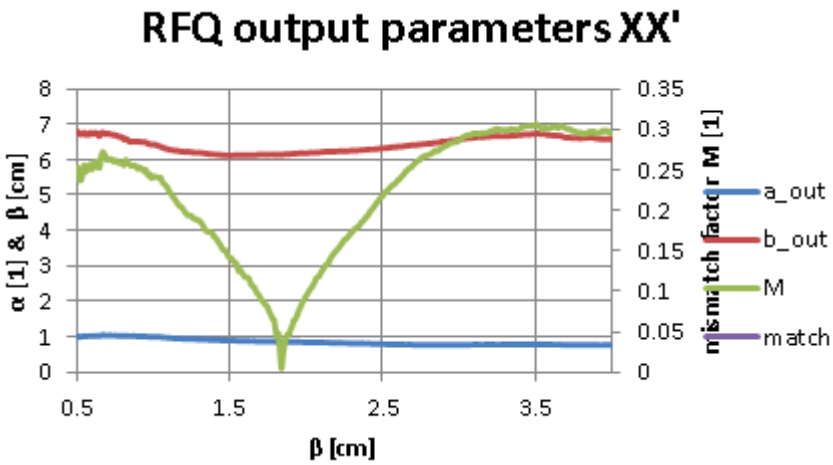

Figure 4.18: RFQ output parameters in the horizontal plane

RFQ sensitivity: input beam β dependency

In Figure 18 one can see that for very small β, the transmission rate rapidly drops down to 2% due to overfocused beam. A transmission of $> 85\%$ is achieved with β=0.51 cm. So this will be the lower limit for further investigation. The upper limit will be kept at β=4 cm even though it could by pushed even further, but it is very unlikely that a mismatch in β of over 100% will occur. For the output parameters in the horizontal plane, likewise behaviour as in **??** can be observed (Figure 19). The bandwidth of variation for $\alpha_{xx'}$ is 0.29 and for $\beta_{xx'}$ 0.84 cm. The maximum mismatch factor is 0.31 and was found at 3.51 cm/rad.

The vertical plane (see Figure 20) paints a similar picture in terms of behaviour in the vertical as it does in the horizontal plane (Figure 19). The bandwidth for $\alpha_{yy'}$ is 0.26 and for $\beta_{yy'}$ it is 1.68 cm/rad. The maximum mismatch is 0.25 at ? = 0.71 cm/rad.

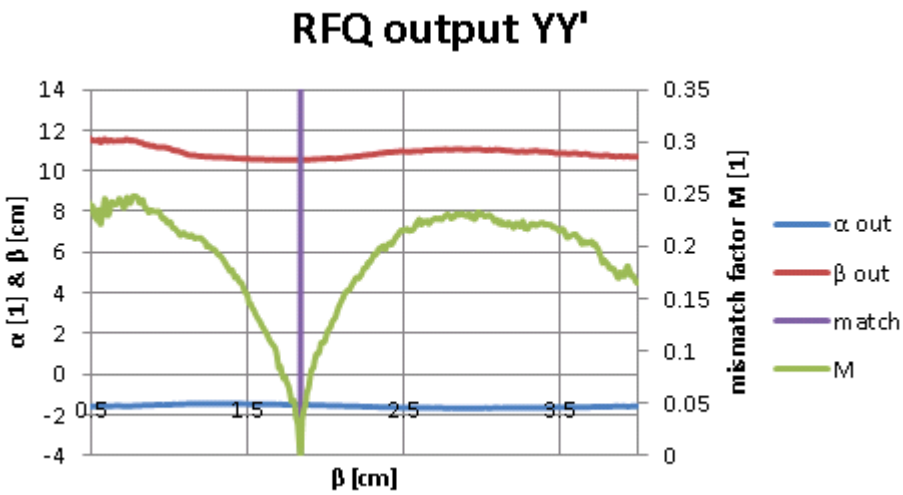

Figure 4.19: RFQ output parameters in the vertical plane

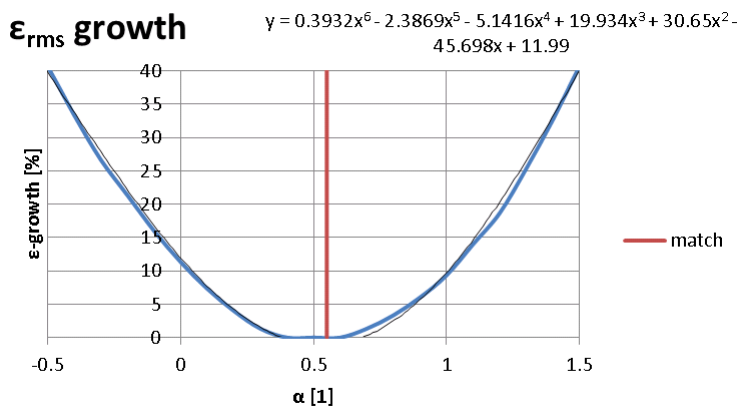

Figure 4.20: α-mismatch induced emittance growth

Mismatch induced emittance growth

Understanding the effects of mismatch on the output α and β is important, because it gives a hint on how to correct certain errors using the quadrupoles in the IMS. Yet the emittance cannot be manipulated.

Despite α & β being relatively independent towards variations of the input parameters, the output emittance is not. Figure 20 and Figure 21 show the emittance growth in [%]. Also included in the plots are polynomial fits, in which even higher order terms play a significant role. This underlines the importance of proper RFQ matching. This analysis makes clear that the optical matching has to be performed with great care to avoid further unwanted emittance growth. The behaviour is so similar in both planes that a separate treatment of the planes would provide no additional insight.

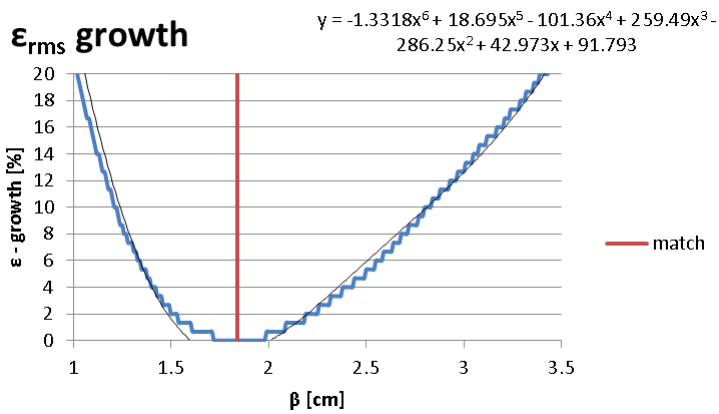

Figure 4.21: β-mismatch induced emittance growth

4.3.5 RFQ acceptance

The key beam parameter to good transmission is the emittance of the input beam. The lower the emittance is, the higher will be the transmission. The upper limit for the emittance is called acceptance. In this section three different approaches to deriving the theoretical value of the acceptance will be used:

- A single particle scan; one particle is tracked through the RFQ with varying input phase space coordinates
- A pencil beam scan; a very small, low current beam with varying position and angle is sent through the RFQ
- Acceptance calculation via phase advance in the RFQ cells.

The calculated values will only give a hint at the real value as all the calculations assume ideal conditions. In reality, the acceptance will be below the theoretical value due to deviations from theory (manufacturing tolerances, alignment, inhomogeneous field distributions).

Single particle scan

The first approach to calculating the acceptance will be a single particle scan in the transverse plane. For each duple XX' in the transversal plane a particle is generated and sent through the RFQ. If the particle is transferred (and accelerated) through the RFQ, its phase-space coordinates will be entered to a list. If the particle is lost, it will be neglected from this list. The obtained list of coordinates is loaded into EAA to calculate the RFQ acceptance.

Using EAA it is possible to fit an ellipse to the plot, which can be varied in size. So finding the correct size of the ellipse will give the acceptance. To determine the correct size of the acceptance ellipse the following criteria were used:

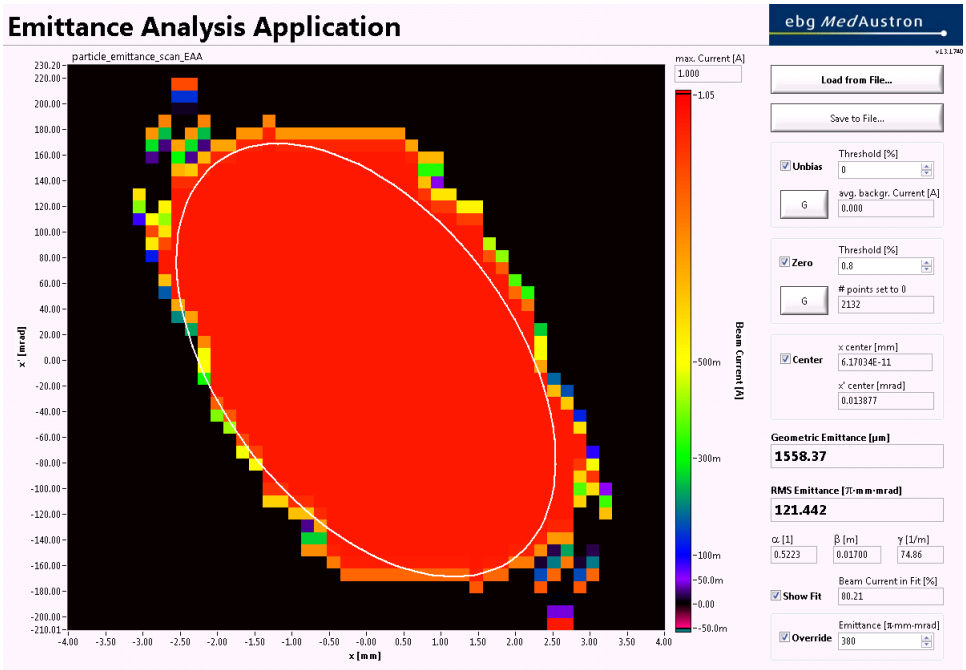

Figure 4.22: RFQ acce[scale=0.4]pse, 380 π.mm.mrad

	$\alpha[1]$	$\beta[mm/mrad]$
design	0.55	0.0184
simulated	0.52	0.0170

Table 4.10: RFQ input α and β

- The ellipse has to be as big as possible
- The ellipse must not enclose coordiantes at which no particle was transmitted.

Using the above mentioned criteria and fitting the ellipse to the distribution, the value of the acceptance amounts to 380 π.mm.mrad.

Figure 21 displays the generated acceptance ellipse already imported into MedAustron's Emittance Analysis Application. The beam parameters of this artificial distribution are very close to the design values of the RFQ, which were given by IAP Frankfurt. Since it is possible to reproduce these values, the single-particle-scan-method has proven to be useful.

The pencil beam approach

In the pencil beam approach in contrast of using a single particle, a finite particle distribution is used. Instead of now changing each particle's coordinates individually, the changes are applied to the centre of the distribution. The basis for the pencil beam was a measurement performed at the TB1. The slits (TS01004SLX) behind

	$\alpha[1]$	$\beta[mm/mrad]$	$\epsilon_{total}[\pi.mm.mrad]$
XX'	0.14	0.007	50
YY'	0.14	0.007	50

Table 4.11: Pencil beam parameters

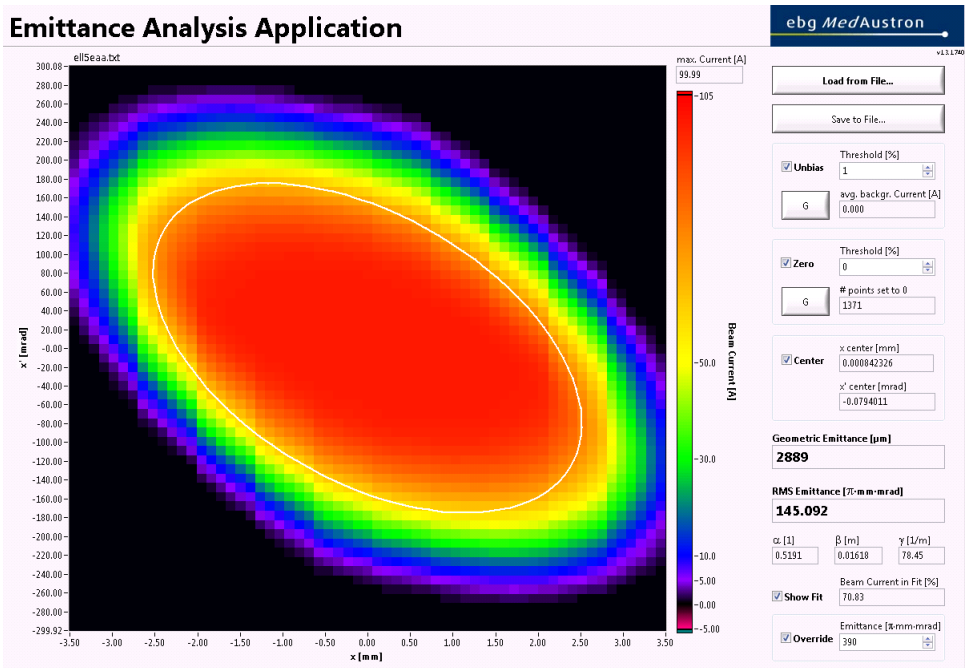

Figure 4.23: pencil beam, tran4mission scan

the quadrupole-triplet were used to cut the beam vertically and horizontally in such a way that the beam in the TB1 would be as small as possible and still measureable in terms of beam current.

The parameters of the beam used for the simulation are listed in Table 11 (note that the 50 π.mm.mrad now correspond to the total emittance and not, as usual, to the RMS).

A small beam (for parameters see Table 11) was generated in PARMTEQM. The beam centre was shifted ($\pm$3.5 mm) and tilted ($\pm$350 mrad) in small steps. The coordinates were only manipulated in the XX'-plane while the YY' plane coordinates were left unchanged (0;0). Each pixel in Figure 22 represents a run of PARMTEQM with the corresponding beam centre coordinates. The colour scale indicates the transmission for the particular run (red is maximum with 100%, yellow 50%, and black the minimum with 0%). Since this approach uses a finite beam distribution the criteria to evaluate the acceptance ellipse had to be adapted. The area which contains all phase-space coordinates that resulted in a $\geq$ 50% transmission is added to the acceptance. The idea is that since 50% of the beam gets lost on the aperture the other 50% must be in the acceptance. Applying this criterion to Figure 22 leads

	$\alpha[1]$	$\beta[mm/mrad]$
XX'	0.55	0.0164
YY'	0.52	0.0164

Table 4.12: RFQ acceptance ellipse parameters

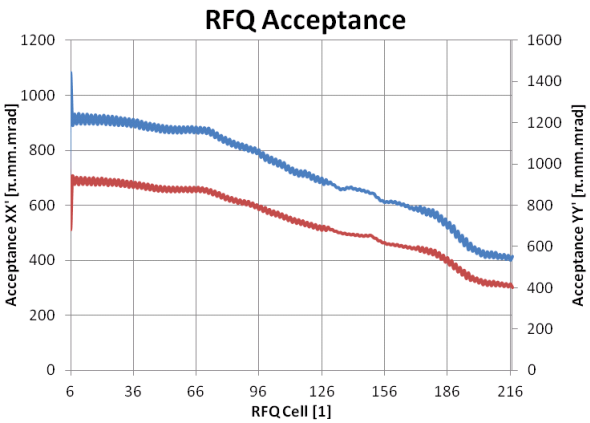

Figure 4.24: Un-normalized acc4ptance along RFQ

to a 390 π.mm.mrad acceptance ellipse which is in agreement with the single particle scan performed in 4.3.5

Calculating acceptance based on phase advance per period

Another strategy to obtain the acceptance of an RFQ is to use a simulation code, that calculates the phase advance per RF-period in each cell and apply it to the following formula:

$$A_n = \min(\frac{\sigma a^2}{\lambda}) \tag{4.1}$$

which gives the normalized acceptance for an RFQ. σ is the phase advance per period with current, a is the minimum radial aperture of the electrodes and λ is the RF-wavelength. The phase advance was calculated using a perfectly matched beam which was artificially generated by the program PARMTEQM as an input. The space charge has been calculated for a 0.5 mA beam.

Both planes are in the same order of magnitude and are therefore displayed on different axis to separate them optically. The blue graph corresponds to the left axis and the red one to the right axis (Figure 23). The minima of these oscillating graphs represent the (un-normalized) acceptance and are:

The average of both planes is: 400.3 mm.mrad. Despite the numbers being different in all theoretical approaches, they are not too far apart (380, 390 and 400 $\pi.mm.mrad$) the acceptance is always in the same order of magnitude.

	$A_{un}[\pi.mm.mrad]$
XX'	400.7
YY'	399.9

Table 4.13: RFQ acceptance ellipse parameters

4.3.6 Experimental results

The following section will cover beam measurements through the LEBT and the RFQ. Configuration settings for the optical elements of the beam-line are given. Unfortunately it was not possible to perform all measurements with the same setup. Due to wear-off of the ECR Ion Source extraction electrodes, it was necessary to replace them with a new version provided by the Ion Source supplier PANTECHNIK. At that point the TB1 (the measurement setup displayed in Figure 4 and Figure 6) was already removed and replaced by the RFQ and the TB2. That means that emittance measurements after the solenoid (before the RFQ) could not be redone. It was decided to reconfigure the optical elements to match to measured beam parameters after the bending magnet (TS-01-000-BDT-D) and after the quadrupole triplet (TS-01-002-BDT-D), which were performed during Stages 1 and 2. This was done under the assumption that the beam optics will be similar when passing through the solenoid and the beam will be matched to the RFQ. Besides setting-up the optical elements, it is also very important to steer the beam on axis before and after the solenoid magnet. The steering procedure is covered in a separate section of this document. At the end of this chapter a comparison between simulations and measurements at different beam diagnostic devices in the beam-line is presented.

Steering and solenoid alignment

There are four combined horizontal and vertical steering magnets and one dipole magnet along the LEBT, that allow correction of the position and angle of the beam centre in the horizontal and vertical planes. After configuring the entire beam-line, so that the beam is centred at all beam profile measurement points. It became clear that the system was dynamic and not fully reproducible from day to day (small beam variations from the Ion Source) and therefore it was not possible to reproduce the beam steering throughout the entire beam-line for the same magnet settings. The ripple of the output current of the magnet power converters is in the order of 5x10-5 and is not an issue for the steering stability. Since adapting the steering to every new situation is a time consuming task (no automated procedure at that time), it was decided to change only the steering magnets after the quadrupole triplet in order to save time. This is sufficient since any deviation from the centre after the triplet can be corrected with two steering magnets to ensure the beam enters the solenoid on axis. The general procedure is as follows: Both steering magnets (TS-01-002-MCX and TS-01-003-MCX) have to be turned off to evaluate the momentary position and

angle of the beam. From this, the necessary currents for the steering magnets can be calculated. These values give a good assumption for the actual currents which have to be applied. At first the displacement has to be corrected. This is done using the first steering magnet (TS-01-002-MCX). The goal is to place the centre of the beam in the centre of the second steering magnet (TS-01-003-MCX). The position of the beam in the second steering magnet cannot be measured directly. It is necessary to measure its position at two separate wire-scanners (TS-01-004-WSX and TS-01-006-WSX). With these two points it is possible to calculate the position of the beam in the magnet (TS-01-003-MCX) using a simple linear interpolation. After 3-4 iterations the beam is usually well centred in the second steering magnet. From this point on, all that needs to be done is to correct the angle. Simply applying the calculated current usually centres the beam within ± 0.2 mm. Varying the steerer current manually by a small amount ($\tilde{0}.1$ A) results in a centred and angle-free beam.

- Turn off steering magnets
- Measure position at TS-01-004-WSX and TS-01-006-WSX,
- Calculate steering currents,
- Use TS-01-002-MCX to centre the beam in TS-01-003-MCX,
- Correct angle with TS-01-003-MCX.

The importance of steering comes into play when taking into consideration that a solenoid is very sensitive to displacement or angle of the beam. A beam will only be centered after a solenoid if it enters centered (assuming the magnetic centre is the same as the geometric one) due to the fringe fields. Otherwise, because of the coupling of the transverse planes in a solenoid, an error in one plane creates an error in both planes after the solenoid (position and angle). In addition, the beam emittance increases as well. Therefore it is of high importance that the beam is well steered. Also the solenoid must be well aligned with respect to its magnetic axis. With the initial alignment, a centered beam at the entrance of the solenoid would be significantly off-axis (up to 1.5 mm and 9 mrad) at the RFQ entrance. To obtain a centered beam at the RFQ entrance, it was necessary to steer the beam off-axis when entering the solenoid. This led to beam current losses since the beam was touching the electrodes of the EFE. The measured displacement at the RFQ input could be either due to an error in the BD devices (hardware and/or software) or due to a misalignment of the solenoid. The fault of BD devices has been discarded after several checks. It was therefore concluded that the alignment of the solenoid was not done properly. The alignment was done using the only two available alignment targets. Due to the lack of a third target, 3-point alignment was impossible and the horizontal tilt had to be checked using a tilt-meter on a 4mm machined surface on top of the solenoid, which is not sufficiently accurate. It was proposed to perform a beam based alignment of the solenoid by shifting and tilting the solenoid to bring the

beam on-axis after the solenoid. Due to the complex behaviour of a beam passing through a solenoid the procedure required extensive preparation. The effect of the solenoid on off-axis beam was simulated using Trace 3D. The simulations showed that the effects of beam displacement and angle are linear and furthermore, they add up linearly. So to understand the combined effect of displacement and angle one just has to add the corresponding values calculated with Trace3D. Using Trace 3D it was also possible to track the beam back through the solenoid to its entrance and to the position of Wire Scanners TS-01-004-WSX, TS-01-006-WSX upstream the solenoid. This gave a first idea in which direction the solenoid had to be shifted and tilted. The preliminary values found from the simulation were used to shift and tilt the solenoid. In order to get a more accurate idea on how to realign the solenoid, the beam was missteered many times to gain a better understanding of the effects of an off-axis beam. With this experience and simulation it was possible to start with the beam-based alignment. After several trials and large amount of measurements the proper alignment of the solenoid was achieved. The measured beam centre position at the RFQ entrance was strongly reduced and was within tolerances. See 4.2.2.3 for details.

4.3.7 Beam-line configuration and measurements

Configuration

Ion source configarion

- HV: 24 kV
- Focus electrode voltage: 1.9 kV
- Puller electrode voltage: 0 V
- RF generator frequency: 14.486 GHz
- RF attenuation: -20.80 dBm
- Gas flow: 55
- Extraction system position: 0 mm
- Tuner position: 2.48 mm

Optical elements:

- Spectrometer dipole TS-01-000-MBH: 37.8 A $\hat{=}$ B =0.9526 T
- Quadrupole magnet TS-01-000-MQF: 141 A $\hat{=}$ GL=0.198 T
- Quadrupole magnet TS-01-001-MQD: 156 A $\hat{=}$ GL=0.219 T
- Quadrupole magnet TS-01-002-MQF: 51 A $\hat{=}$ GL=0.072 T

- Solenoid magnet TS-01-000-MSO: 146 A $\hat{=}$ BL=0.08903 T.m

For the quadrupole triplet it has been found that the integrated field gradients obtained from measurements have to be up to 7% higher than those obtained from simulations. This is caused by the cross-talk between the adjacent magnets, which is not taken into consideration in the simulation codes (L_{eff}= 109 mm $\forall$ MQZ). The effective length of the quadrupole magnets in the triplet varies from 104 mm to 109 mm with the strength of the field gradient, which is very different for the last quadrupole (see above).

Steering elements before the quadrupole triplet:

- TS-00-000-MCX-A horizontal plane: 0 A
- TS-00-000-MCX-A vertical plane: 4 A BLeff = 2.62*10-4 Tm; θ_{kick} = 6.77 mrad
- TS-01-000-MCX-A horizontal plane: 0 A
- TS-01-000-MCX-A vertical plane: 0 A

Steering elements after the quadrupole triplet:

- TS-01-001-MCX-A horizontal plane: 0.65 A BLeff = 2.78*10-5 Tm; θ_{kick} = 0.7 mrad
- TS-01-001-MCX-A vertical plane: 0.3 A BLeff = 2.27*10-5 Tm; θ_{kick} = 0.59 mrad
- TS-01-002-MCX-A horizontal plane: -0.95 A BLeff = -4.56*10-5 Tm; θ_{kick} = -1.2 mrad
- TS-01-002-MCX-A vertical plane: 0.2 A BLeff = 1.6*10-5 Tm; θ_{kick} = 0.42 mrad

Measurements

TS-01-000-BDT-D Figure 24 is the first beam current measurement in the beam-line performed in the Faraday Cup in TS01000BDT-D. It shows the beam current after the spectrometer and will be used as a reference current to calculate the transmission efficiency of the beam-line. The highest measured relative deviation of the current is ±1.5%.

Figure 25 and Figure 26 show the measured beam profiles in the horizontal and vertical planes on the first set of Wire Scanners.

The Wire Scanner measurements in Figure 25 and Figure 26 were used to steer the beam on axis. The beam position is measured with an accuracy of ±0.1 mm. The measured beam size is used to define the necessary boundaries for slit movement in order to perform an emittance measurement. From the horizontal Wire Scanner and

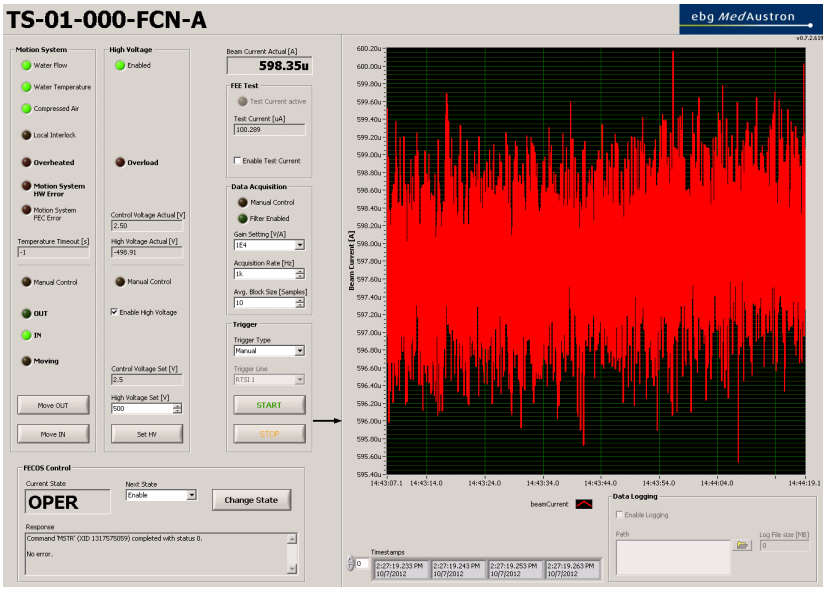

Figure 4.25: TS01000FCN-A, 5983μA

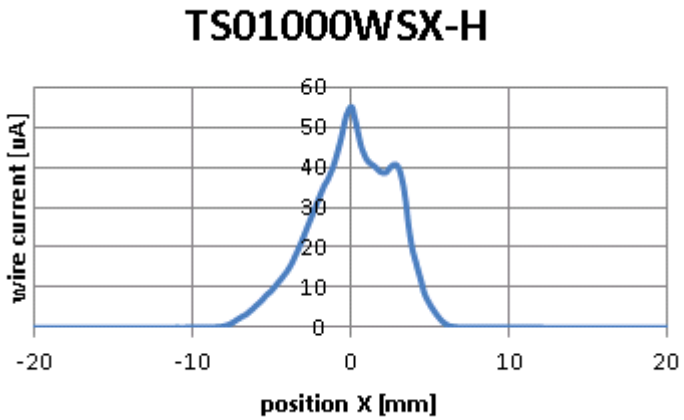

Figure 4.26: horizontal beam profile at TS01000WSX-H

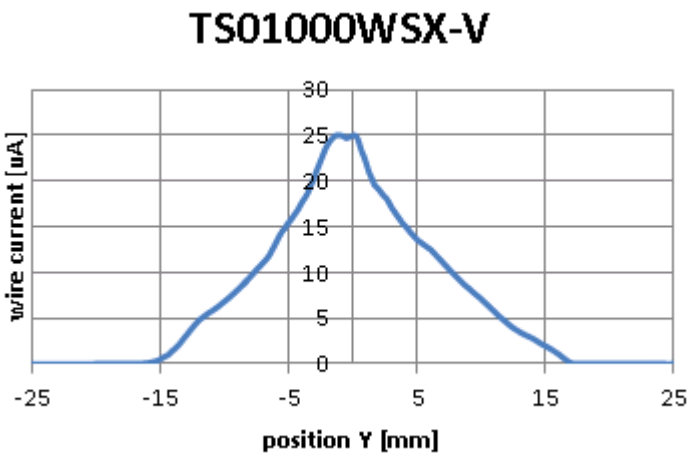

Figure 4.27: vertical beam profile at TS01000WSX-V

Phase space	α**[1]**	β**[mm/mrad]**	ϵ_{RMS}	$\epsilon_{90\%}$
XX'	3.11	0.67	42.65	176.5
YY'	1.67	1.16	45.87	209.24

Table 4.14: measured Twiss parameters after spectrometer

the emittance measurement performed in TS01000BDT-D it becomes visible that the beam is in fact a conglomeration of two separate beamlets. When looking at Figure 27, one can clearly see two spatially separated maxima in the beam current. The origin of these two beamlets can be found in the magnetic field geometry of the Ion Source, which confines the plasma [ref]. The development of the beam exiting the plasma chamber and up to the first diagnostic tank is subject to later studies.

The measured beam distribution was transported through the beam-line up to the RFQ. The matching procedure covered in Section 3.3, is based on this measurement.

TS-01-000-BDT-D The next diagnostic tank is placed right after the quadrupole triplet. It contains diagnostic devices for emittance, profile and beam current measurements. It is the first position in the beam-line where the measurement and simulation are compared.

Figure 29 and Figure 30 allow quick comparison of the measured and simulated beam profiles. In both planes the general shape agrees to a certain extent. The beam width can be found in Table 4.15. Here the widths show quite a large discrepancy (up to 20% for Y), but it has to be noted that it is much simpler to find a single particle in a histogram (simulation) than it is on a moving wire. This could explain the larger tails in simulation compared to the measurement.

The emittance measurement behind the quadrupole triplet can be seen in figure

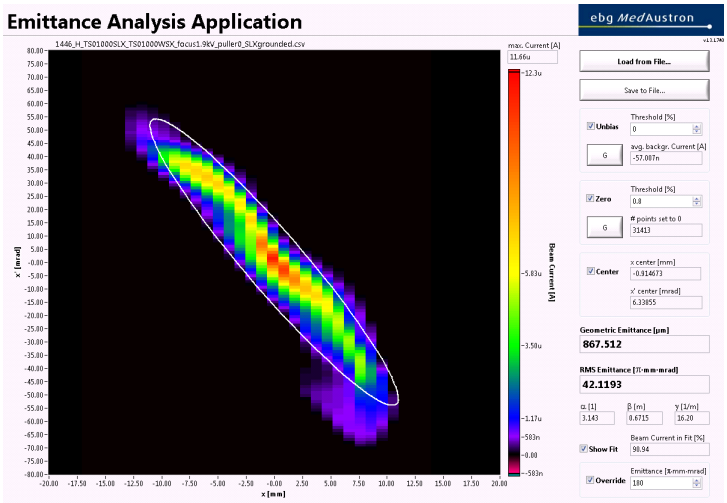

Figure 4.28: emittance measurement - XX′

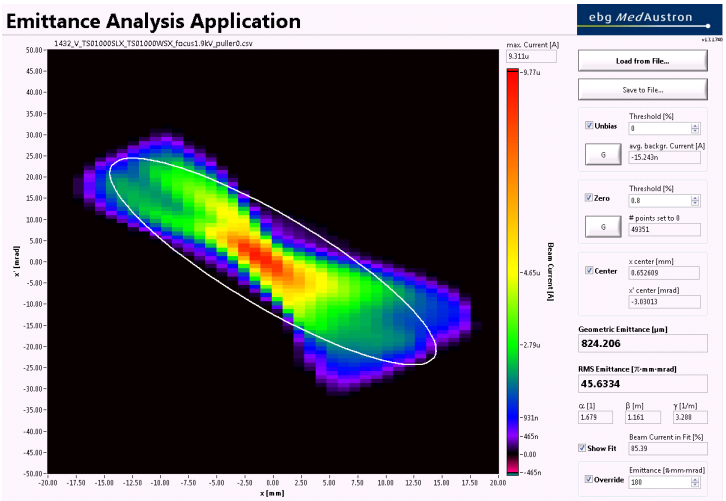

Figure 4.29: emittance measurement - YY’

(a) measured beam profile

(b) simulated particle histogram

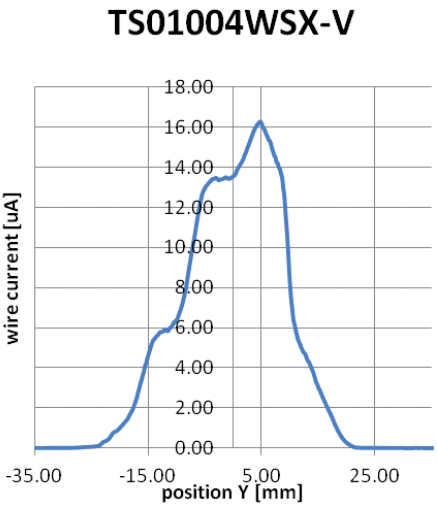

(a) measured beam profile

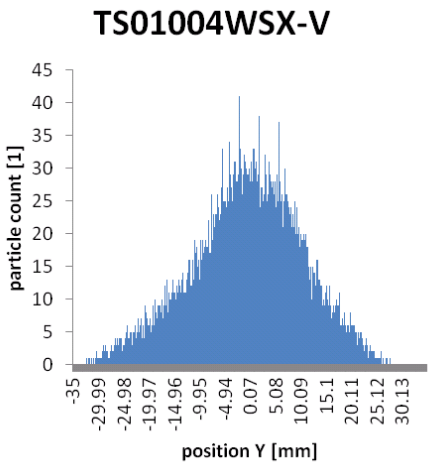

(b) simulated particle histogram

	Width measured [mm]	Width simulated [mm]
X	33.7	36.3
Y	46.0	57.2

Table 4.15: measured and simulated beam width at TS01004WSX

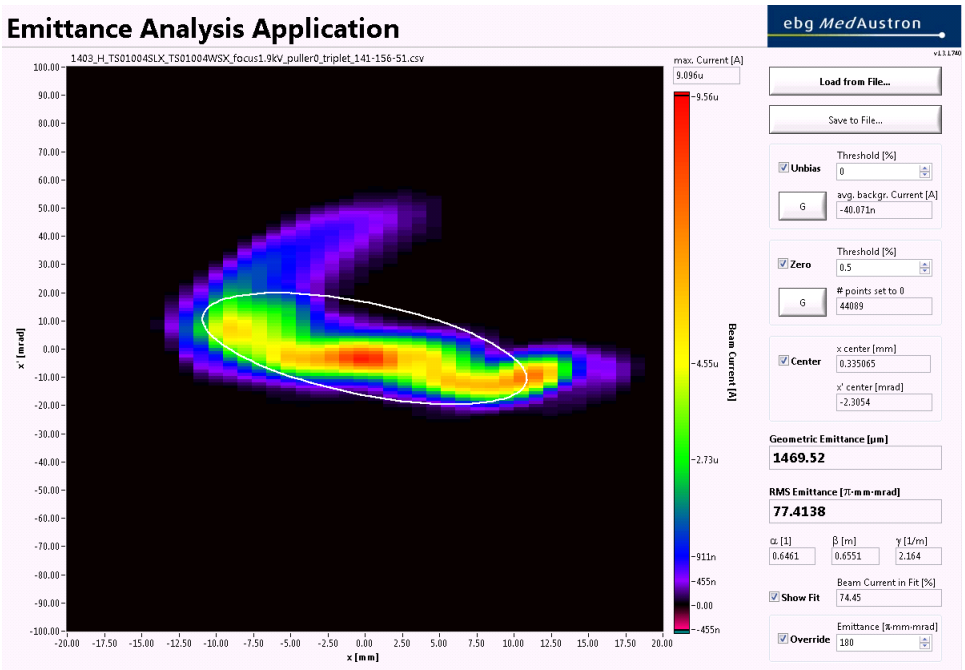

Figure 4.32: emittance in XX′, TS01004SLX-H

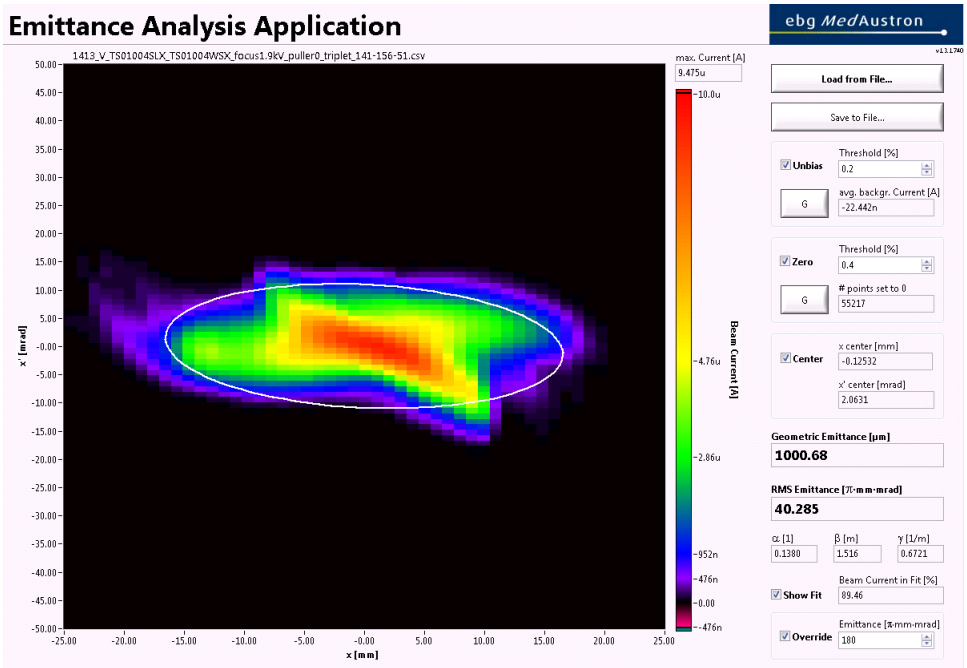

Figure 4.33: emittance in YY′, TS01004SLX-H

	$\alpha[1]$	$\beta[mm/mrad]$	$\epsilon_{RMS}[\pi.mm.mrad]$
XX’	0.646	0.655	77.41
YY’	0.138	1.516	40.29

Table 4.16: Beam parameters after triplet

4.32 and figure 4.33.

What is outstanding about this measurement is that the horizontal emittance has increased dramatically between the first measurement after the spectrometer and the diagnostics tank after the triplet. This increase does not appear in simulations even though a best-fit macro-particle distribution was used. Simulations starting after the spectrometer dipole do not take into account the dispersion in the horizontal plane introduced by the spectrometer dipole. Yet emittance growth introduced by dispersion alone cannot explain such a strong increase. A possible explanation of this phenomenon could be that the beam is in fact consisting of two beamlets, which rotate differently in phase space. In that case the effect of space charge forces and dispersion could lead to such an emittance growth. It is also interesting that the vertical RMS emittance has decreased, which also cannot be found in simulations. This however could be explained by the beam losses. The emittance measurement technique using slits and wire scanners cannot provide the correlations between the two planes. This would also explain why the emittance growth in the horizontal plane cannot be seen in the simulations. Additionally the dipole has a non-negligable sextupole-field. It’s effect can be seen in figure 4.29. The blowup towards the tails

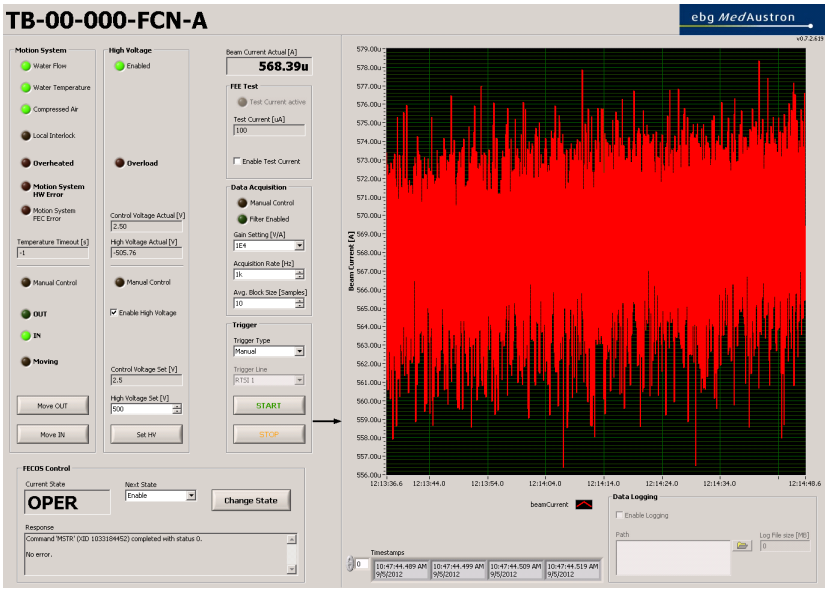

Figure 4.34: beam current in TB00000FCN-A,568.4μA

	Width measured [mm]	Width simulated [mm]
X	46.7	62.3
Y	64.6	68.3

Table 4.17: measured and simulated beam profiles at TB00000WSX

originates from the coupling introduced by a sextupole field. So not being able to capture the correlations between the planes hinders the simulation additionally.

TB-00-000-BDT-D The TB-00-000-BDT-D covers all the necessary measurements at the RFQ entrance. The emittance measurement set-up is slightly different in this diagnostic tank. Instead of using two Slit plates that are separated longitudinally by 4 mm, as in the LEBT, a single Slit plate with a 0.5 mm gap is used in both transverse planes. This allows placing the horizontal Slit plate right in the matching plane of the RFQ and therefore measure the beam emittance and Twiss parameters directly in the matching plane. For mechanical reasons the vertical Slit is located 14 mm downstream the matching plane. One is interested in the beam parameters at the RFQ entrance and therefore the measured vertical beam parameters are tracked back to the matching plane using simulation code Trace 3D.

Figure 4.34 displays the beam current measured with the Faraday Cup in the TB-00-000-BDT-D. The initial beam current at the exit of the spectrometer dipole is μA. So the overall transmission throughout the beam-line is $\tilde{95}\%$ (97.6% in simulation).

Figure 35 and Figure 36 show the measured and simulated beam profiles in TB00000BDT-D. Comparing simulation and measurement is not very reliable in this case, due to the faulty alignment of the solenoid. The general shape however

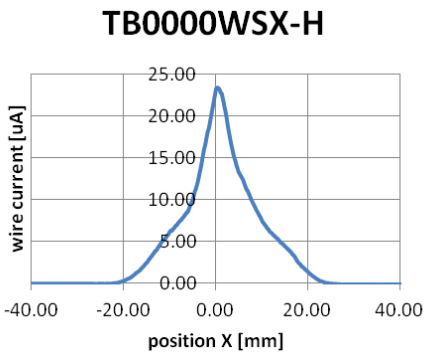

(a) measured beam profile

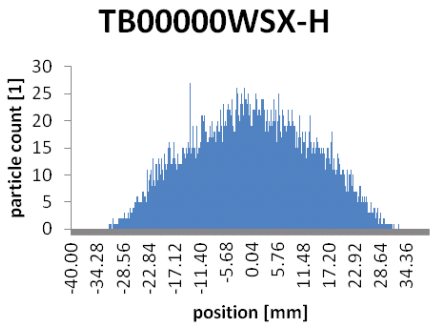

(b) simulated particle histogram

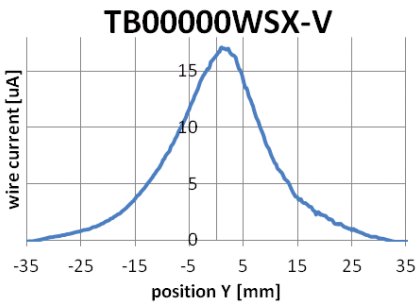

(a) measured beam profile

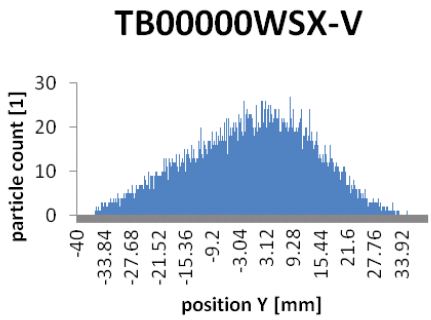

(b) simulated particle histogram

	XX′	YY′
Position [mm]	0.01	0.31
Angle [mrad]	7.03	-2.61

Table 4.18: beam center coordinates in the RFQ matching plane

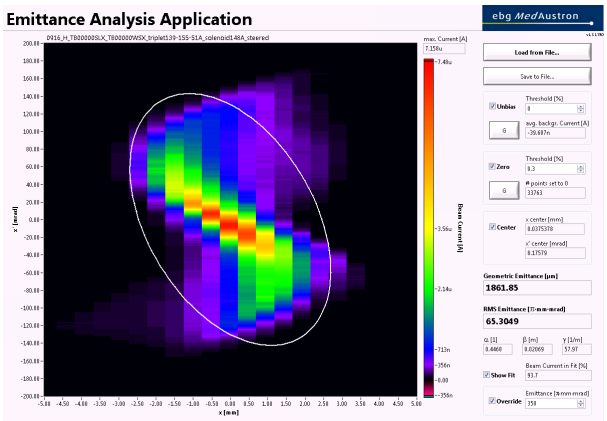

Figure 4.37: Measured XX′ beam emittance in TB00000BDT-D

seems to be in agreement. The centre of charge for the horizontal measurement is 1.2 mm and for vertical it's -0.1 mm at the TB00000WSX. As can be seen in Table 19 the beam is on axis at the RFQ matching plane. The vertical coordinates have been tracked back by 14 mm (Trace 3D) to obtain results at the RFQ input plane. The beam position and angle obtained from the emittance measurement is coherent with the Wire Scanner measurements. The measured input beam Twiss parameters are well within the acceptable limits and can be found in Table 20. The last column on the right shows how much of the beam is within the acceptance of the RFQ, which was calculated in Section 3.5. A conservative value of 350 $\pi.mm.mrad$ is used for the RFQ acceptance in this note. The Twiss parameters for the vertical plane have already been tracked back by 14 mm.

The emittance measurement data is used to generate a best-fit particle distribution with genBeam. The simulated transmission through the RFQ using that particle distribution as an input for Parmteqm is 86.5%. As showed in Section 3.4, the variation of the beam Twiss parameters at the RFQ output due to the variation of the input beam Twiss parameters is very small.

Phase space	α**[1]**	β**[mm/mrad]**	ϵ_{RMS}	**beam in acceptance [%]**
XX'	0.447	0.0207	65.30	93.7
YY'(tracked back)	0.361	0.0204	75.61	89.26

Table 4.19: measured Twiss parameters in the RFQ matching plane

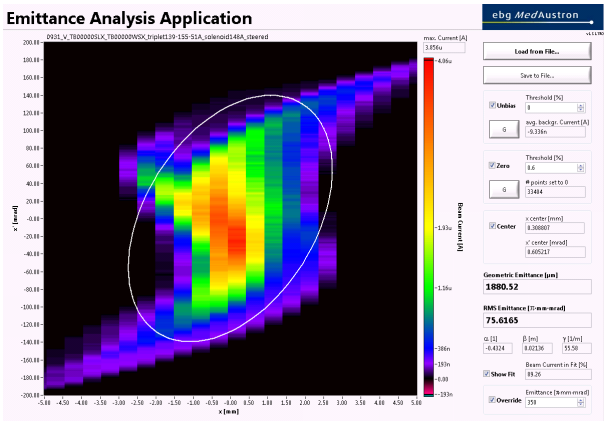

Figure 4.38: Measured YY′ beam emittance in TB00000BDT-D

	$\alpha[1]$	$\beta[mm/mrad]$
XX'	0.88	0.06
YY'	-1.465	0.1

Table 4.20: simulated Twiss parameters at RFQ output

Measurement vs. simulation in LEBT - a quick overview This section is supposed to allow quick look at measurements and simulations. Each of the plots which represent measurements can be found in between 4.2.2.1 and 4.2.2.3 with a more detailed analysis of the results.

The first position to compare simulation and measurement is downstream the quadrupole triplet. It will give insight into the behaviour of the beam and how much one can trust simulation for this beam-line. Comparing Figure 39 and Figure 40 shows that the general shape of the beam can be well predicted for both planes. Also the Twiss parameters can be calculated relatively well. Unfortunately it was not possible to predict the intense emittance growth in the XX' plane. The simu-

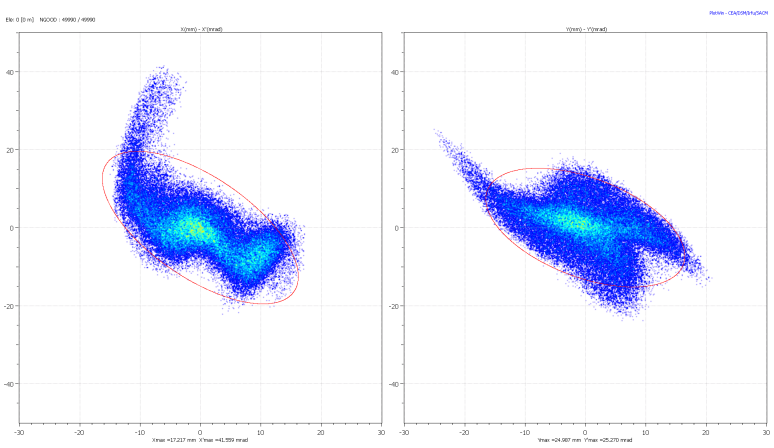

	$\alpha[1]$	$\beta[mm/mrad]$	$\epsilon_{RMS}[\pi.mm.mrad]$
XX'	0.86	0.90	48.6
YY'	0.37	1.53	44.0

Table 4.21: simulation after triplet

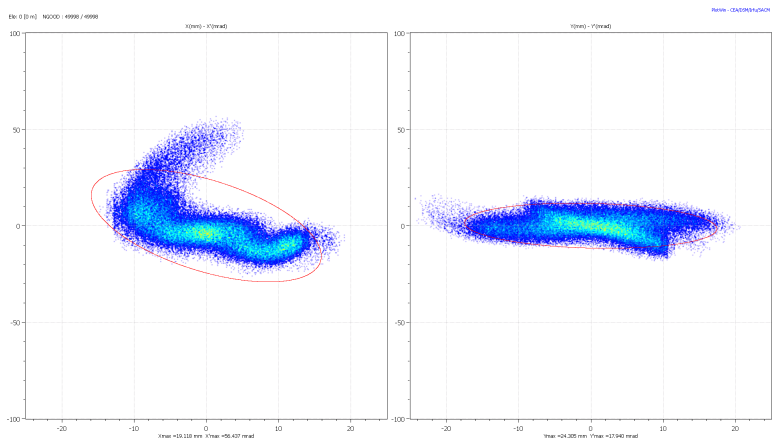

	$\alpha[1]$	$\beta[mm/mrad]$	$\epsilon_{RMS}[\pi.mm.mrad]$
XX'	0.646	0.655	77.41
YY'	0.138	1.516	40.29

Table 4.22: measurement after triplet

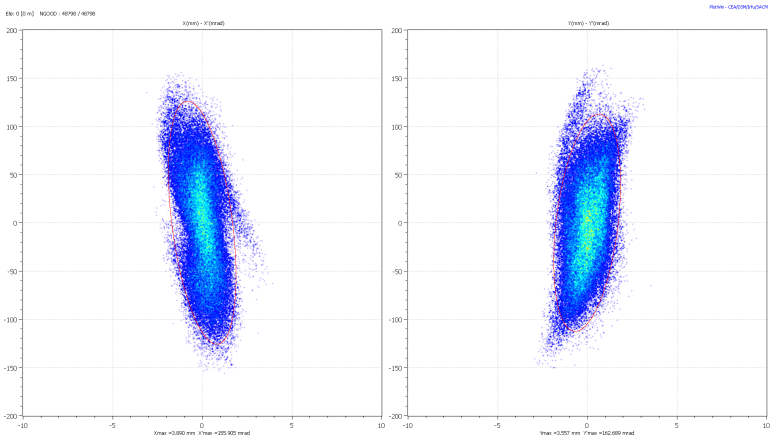

	$\alpha[1]$	$\beta[mm/mrad]$	$\epsilon_{RMS}[\pi.mm.mrad]$
XX'	0.48	0.0166	42.8
YY'	-0.38	0.0177	39.2

Table 4.23: simulation after solenoid

lation code does not take into account that the dipole introduces dispersion in the horizontal plane. It is not possible in Path Manager to include an artificial dispersion curve to a distribution. The same statement can be done about the measurement behind the solenoid. ? and ? could be predicted very well, but the emittance could not. Also the tails in the vertical distribution are not strongly developed in the simulation. With proper alignment of the solenoid, it is hoped that the origin of these tails is remedied.

The particles have been tracked an additional 14 mm in the vertical plane to account for the distance between horizontal and vertical emittance slits.

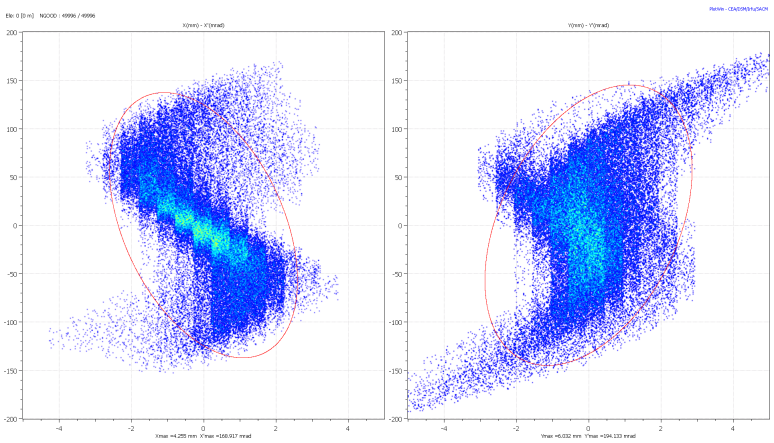

Figure 4.39: measurement after solenoid

	$\alpha[1]$	$\beta[mm/mrad]$	$\epsilon_{RMS}[\pi.mm.mrad]$
XX'	0.447	0.0207	65.30
YY'	-0.43	0.0214	75.61

Table 4.24: measurement after solenoid

RFQ measurements

The most crucial measurements performed at the ITS, are of course measurements directly regarding the RFQ. The beam is bunched with a 218.816 MHz time-structure and accelerated from 8 keV/u to 400 keV/u in the RFQ. To measure the energy of the beam, IAP Frankfurt provided a suitable spectrometer dipole. The calibration of this spectrometer dipole was done at IAP Frankfurt by using a Helium beam with known energy. The calibration has then been rescaled to H_3^{1+}.

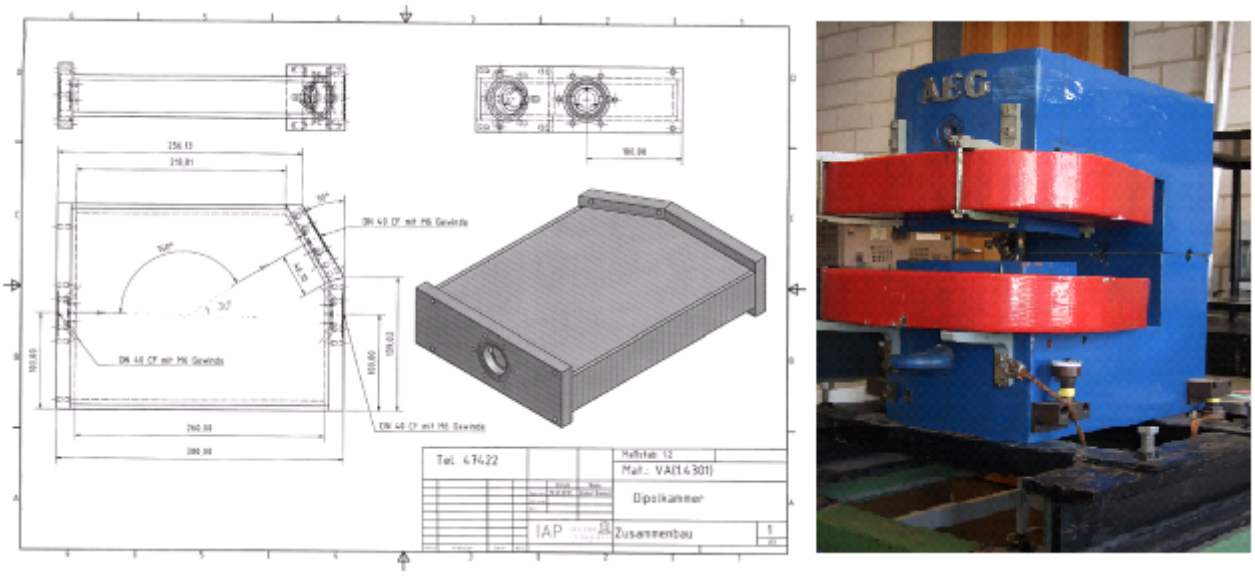

Figure 4.40: dipole chamber and dipole [13]

The set-up for the energy measurement was placed immediately after the RFQ exit plane and consisted of the following:

- The dipole magnet (4.40), which was powered by a 300A Heinzinger power supply. The parameters of the dipole are [13]:
  - Bending angle: 30°
  - Radius of curvature: 0.4 m
  - Edge angles: 0°
  - Nominal field at 62A: 0.46 T

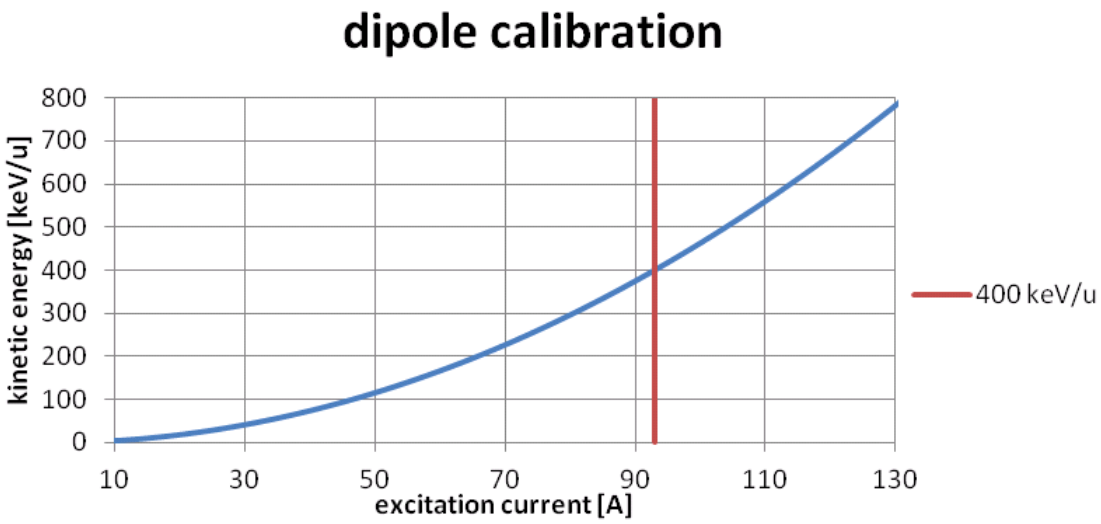

Figure 4.41: IAP Frankfurt spectrometer calibration [14]

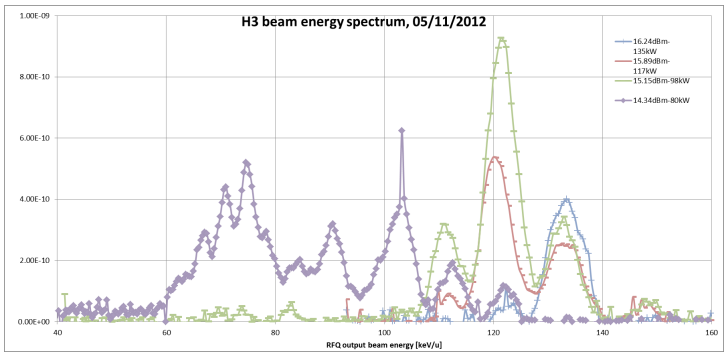

Figure 4.42: H3 energy spectrum for various power levels [14]

- The vacuum chamber of the dipole (**??**), in which two collimators with 1 mm circular opening are installed - one at the entrance and one at the exit of the chamber. The horizontal limitation introduced by the collimator prevents errors in the energy measurement, which would be caused by the horizontal extent of the beam. Two small Faraday cups - one for a bent beam for energy measurement and one for a straight beam which is used for beam based alignment of the set-up.

- A highly sensitive Pico-Ammeter, which is externally triggered to measure the bunched beam current with the proper timing.

- A computer with software to record the measurements.

The first energy measurements performed, did not draw a promising picture of the RFQ's functionality.

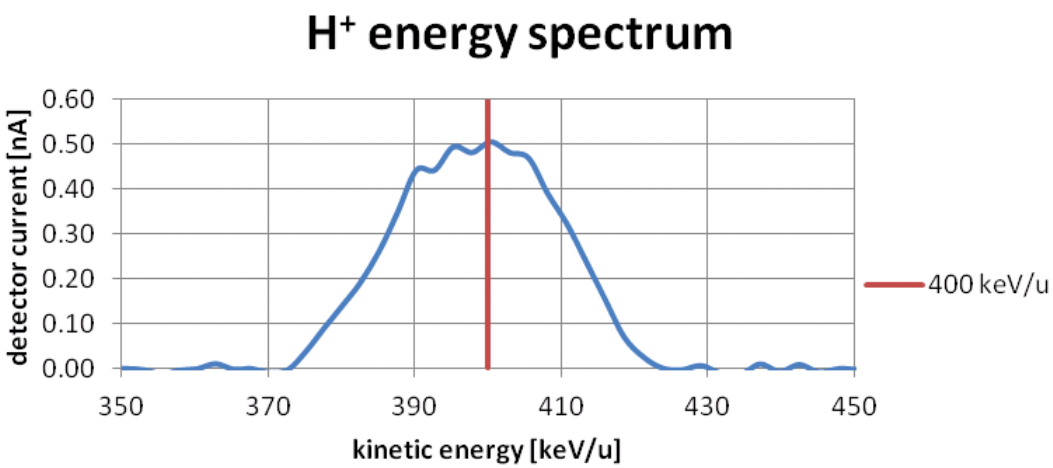

Figure 4.43: H^+ energy spectrum at 15 kW

Figure 4.42 shows energy spectra for various RF power levels, up to 135 kW measured at the transmitter. Since the output power from the RF amplifier is not a clear measure of the field in the RFQ tank, a 50 Ω impedance field probe with an attenuation of 45 dB is placed inside the RFQ tank to measure the power level inside the tank. The voltage on the electrodes is proportional to the measurement of the field probe, which is given in dBm. One can clearly see that the spectrum in Figure 4.42 is nowhere near what is to be expected from the RFQ. First of all, the measured energy is far too low compared to the nominal output beam energy of 400 keV/u. Second, the beam energy is spread over a very wide range. From simulations one would only expect an energy spread of ±7 keV/u around the design energy. The transmission could be tweaked to up to 39%, which is still very little as compared to 86.5% found in simulations.

It was concluded that the nominal electrode voltage of 70 kV was not achieved at this stage and it was impossible to transmit more RF power into the tank due to high reflected power, which caused the amplifier to interlock. It was decided to test the RFQ with H^+, which require 1/3 of the electrode voltage and therefore only 1/9 of the RF power as compared to H_3^{1+}. This allowed testing the RFQ on a wider range of RF power, which could be easily transmitted into the RFQ tank. This could give some insight into the beam dynamics.

After rescaling the Ion Source and the entire beam-line for $q/m = 1$ and also readjusting the transmitted RF power to 15 kW, a well-defined peak was found in the spectrum around the nominal energy (Figure **??**). This led to the conclusion that the electrode geometry is correct. This was a great relieve to the project, as major ßurgeryön the RFQ electrodes would have caused several months of delay. The next step was to try the same measurement with H_2^{1+}. The Ion Source and the entire beam-line was rescaled for $q/m = 1/2$. H_2^{1+} beam requires twice the voltage of H^+ and therefore four times the RF power. Under the assumption that 15 kW

is the appropriate RF power level for H^+, at a power level of 60 kW, also a well-defined peak was found in the output beam energy spectrum. When continuing to $q/m = 1/3$ (135 kW), a spectrum as in Figure 4.42 was found again. The conclusion from these 3 measurements was, that the electrode geometry was correct but at higher RF powers, the nominal electrode voltage of 70 kV necessary to accelerate $q/m = 1/3$ particles was not possible to reach. The next question was how linearly the RFQ electrode voltage responds to the input RF power. In order to check this, the field level in the RFQ tank was measured with the field probe for different input RF power levels. The voltage squared can be calculated using the following expression:

$$U^2 = \frac{Z}{1000} 10^{\frac{x}{10}} \tag{4.2}$$

with x being the measured power level in the tank, taking the probe attenuation into account and Z being the design shunt impedance ($74k\Omega$). The calculated value versus the input RF power is plotted in Figure 4.44. As soon as the curve deviates from a linear trend, part of the transmitted RF power goes into field emission [15]. This can be due to a design Kilpatrick limit of 2.4, which is rather high. Field emission can be enhanced by impurities on the electrode surface. In order to reduce the field emission a second, more intensive RF conditioning of the RFQ tank has been performed. Higher RF power levels (up to 200 kW) were achieved during that process. The blue curve in Figure 4.44 shows the situation after the preliminary RF conditioning and the red one after the second conditioning process. One can immediately see that the red curve is linear on a wider range than the blue one. It was therefore possible to achieve higher fields in the cavity at lower power levels. To check the outcome of the RF conditioning procedure the energy spectrum of H_3^{1+} beam was measured one more time.

Figure 4.45 shows the beam energy spectrum, which was recorded after the second conditioning process, with a field level of 17.90 dBm in the tank. It roughly corresponds to the RF amplifier output power of 190 kW. Other than the peak at 400 keV/u the energy spectrum, which was recorded from 0 to 500 keV/u, was clean. It is important to stress, that due to the losses in the transmission line from the RF amplifier to the RFQ tank the output power of the RF amplifier is not directly indicative of the accelerating field in the tank. The field level measured by the field probe in the tank is the essential number. Experience has shown that the RFQ is very dependent on temperature at which it is operated. If it is too warm, the cavity field will be lower at the same input power due to the increased ohmic losses in the cavity. The temperature stability is extremely critical for a good operation of the RFQ. The final cooling system and temperature stabilization of the RFQ tank was not implemented at the ITS. Also the automatic tuning of the plunger position was not operational at the ITS and had to be done manually.

The plots below show at which field level the beam acceleration in the RFQ starts. This will give a hint for the required power/voltage on the electrodes for acceleration and good transmission.

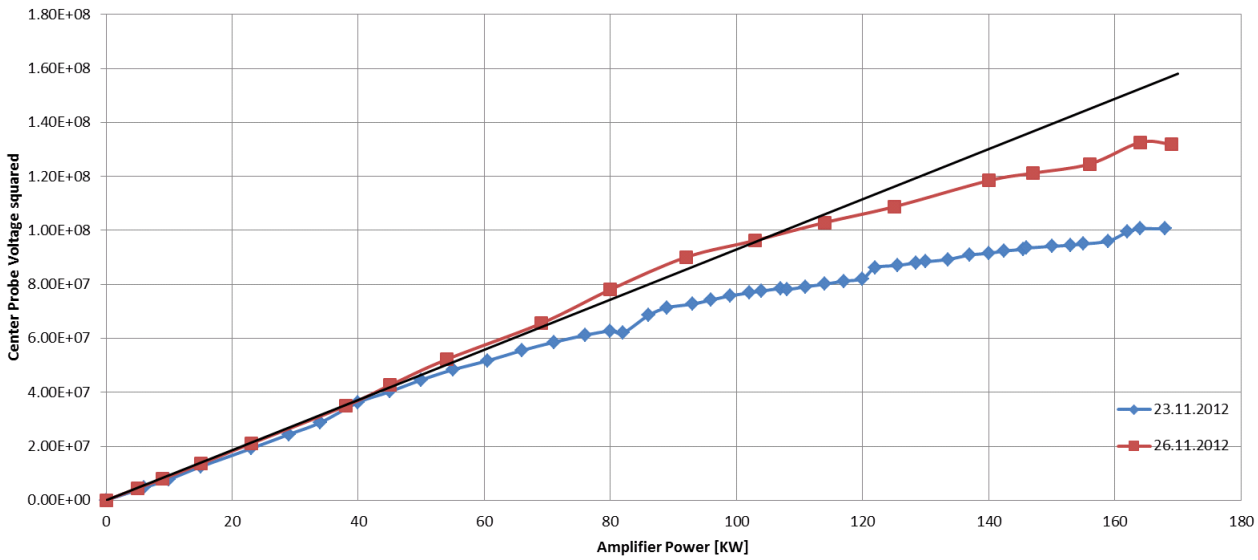

Figure 4.44: Voltage squared (arbitrary values) vs. amplifier power

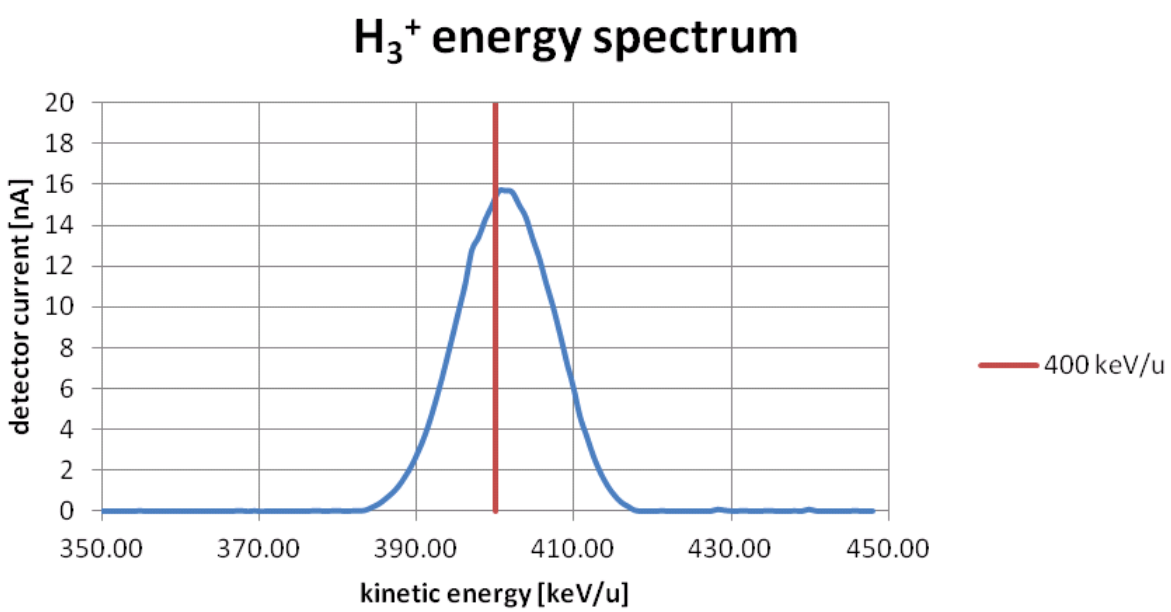

Figure 4.45: H_3^{1+} energy spectrum after the second conditioning process

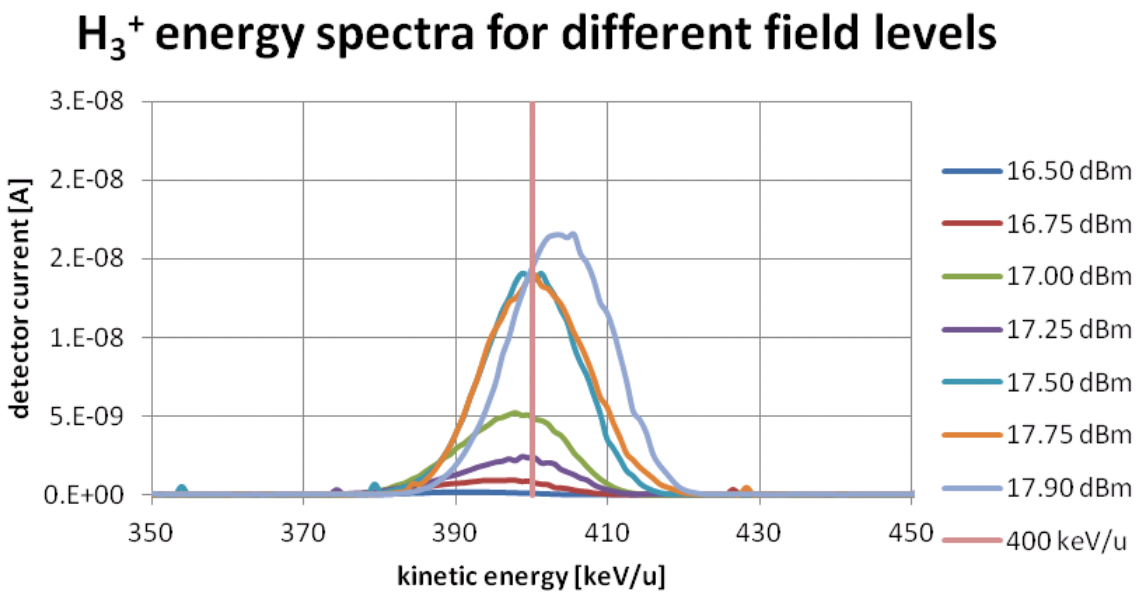

Figure 4.46: H_3^{1+} beam energy spectra for different cavity fields

In general it is very hard to make an accurate statement about the energy measurements with the given setup. First of all, the RFQ was not aligned properly due to the difficulties with its alignment system, so the beam might actually exit the RFQ with an angle with respect to the spectrometer dipole. This can result in an error in the energy measurement. A complete and more accurate statement about energy and its spread can be done at a later point, when ToF measurements with phase probes are possible. This is planned for later measurements in Wiener Neustadt. So the energy measurement with the spectrometer is more a qualitative statement. What can be done is to find a starting point for future measurements in terms of input power and cavity field. In order to do this, spectra were recorded for various power/field levels. From Figure 4.46 one can see that the beam acceleration starts at around 16.75 dBm field level. The nominal energy is reached between 17.50 dBm (397 keV/u) and 17.90 dBm (400 keV/u). Again, this is a rough estimate and requires confirmation using phase probes and ToF measurements. Also for this plot, it is important to mention that the height of the curve does not allow a conclusion in terms of transmission. The vacuum chamber of the dipole has an aperture (1 mm hole at the entrance and the exit), which only allows a fraction of the beam to pass through. If the beam now exits the RFQ with an angle, which may change at different power levels, it is possible that the majority of the beam gets dumped on the aperture and therefore only a small current is measured at the detector after the bending magnet. For transmission statements one should always refer to measurements on current transformers.

To check the consistency of the RFQ behaviour, the same measurement was per-

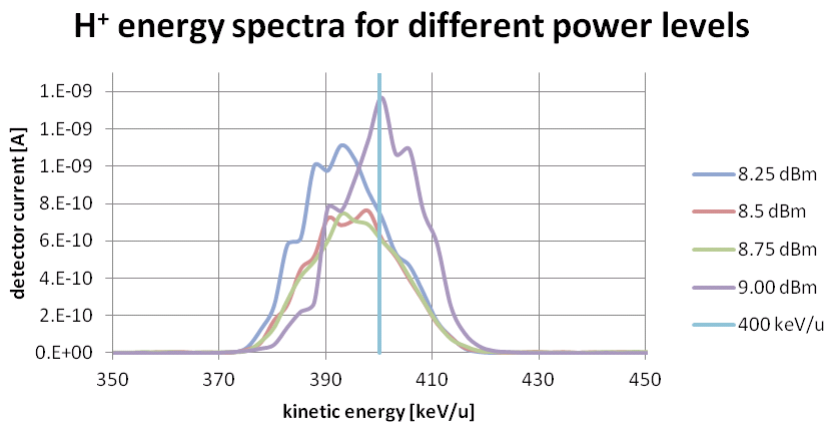

Figure 4.47: energy spectra for H^+

formed for H^+ . The factor in mass of 3 results in a voltage factor of 3 which results in a power factor of 9. A ninth of the power is equivalent to $10 * log(9) = 9.54$ less dBm on the field probe. So if we assume 17.90 dBm to be the nominal field level, 8.36 dBm should give a similar result for protons.

From Figure 4.47 one can draw the conclusion that H^+ get accelerated to 400 keV if the power level for H_3^{1+} is scaled down by a factor 9. The discrepancy between the predicted field level and the actual measured one may come from the field probe itself. The same field probe is used to measure both high and low powers. Many factors come into play here, the dynamic range of the probe, the temperature dependence, field distribution within the cavity itself, etc. Another important parameter of the RFQ performance is the beam transmission. With the measured beam distribution at the RFQ entrance plane, one expects 86.5% transmission from simulations.

The measured maximum transmission is 72% for 196 kW RF power output from the amplifier. Maybe a higher transmission at even higher RF power is possible, but the momentary limitations given by the RF amplifier were reached at 200 kW. Figure 51 shows the simulated transmission versus the electrode voltage. It can be seen that when the nominal electrode voltage has been reached, the transmission plateaus. Looking at Figure 4.49 one can see that the transmission begins to plateau at 190 kW (17.9 dBm). This is another indication that 190 kW RF power is a valid candidate for the nominal input power.

There are a few reasons why the transmission is only 72%. First, the alignment of the RFQ is poor, and second, the input emittance is quite large. Therefore, some tails of the beam will most likely get lost on the aperture. To understand how much of an influence the emittance has on the transmission, another study was performed. It is possible to shape the beam emittance, simply by creating an aperture with the Slit plates after the triplet. This location in the beam-line was chosen because of how the beam ellipse is oriented in phase-space. Since ? is close to 0 in both planes, it is feasible to cut the beam tails in real space. The

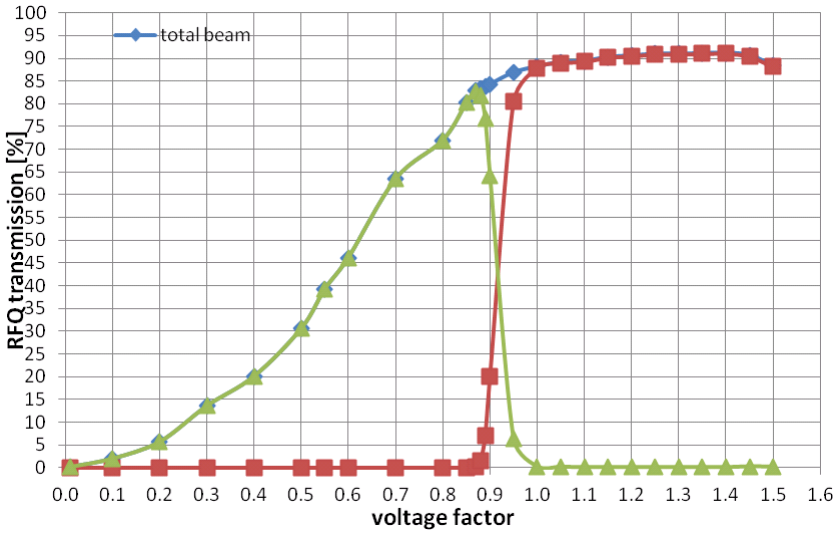

Figure 4.48: simulated RFQ transmission

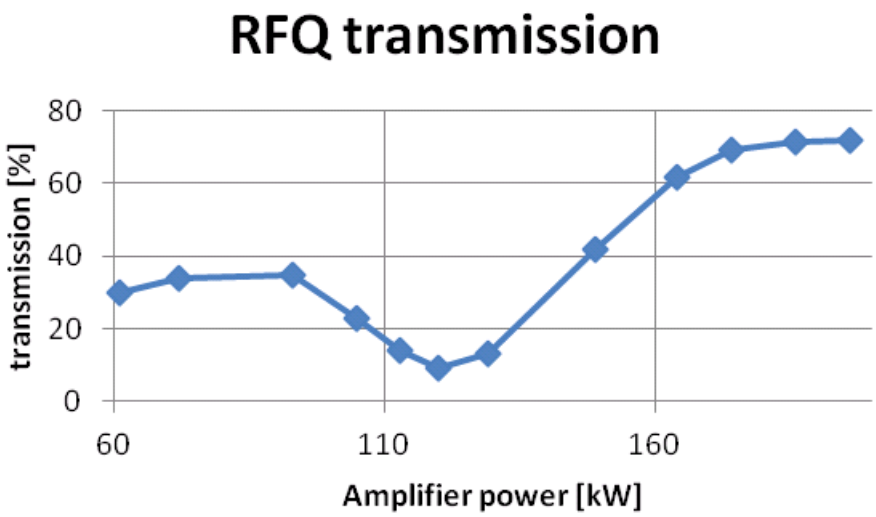

Figure 4.49: measured RFQ transmission

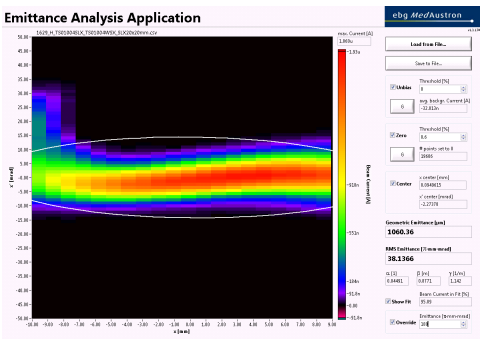

(a) measured beam profile

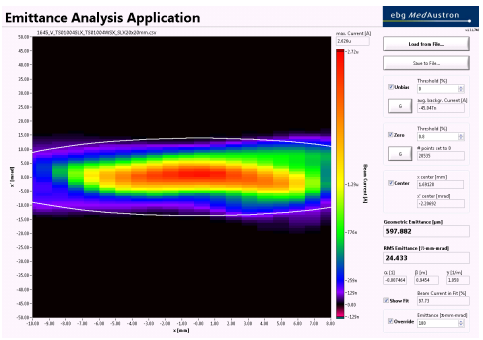

(b) simulated particle histogram

	XX'	YY'
$\epsilon_{rms}[\pi.mm.mrad$	38.14	24.43

Table 4.25: shaped emittance

procedure itself is the following: starting from a very small Slit opening (2x2mm, 100% relative transmission through the RFQ) the opening was increased in steps of 1 mm simultaneously until the relative transmission through the RFQ dropped down to 85%. This occurred at a 20x20mm Slit opening. The next step was to measure the emittance of the cut beam. Wwhile measuring the horizontal plane the vertical slits were kept inside to maintain the 20mm opening, while the horizontal slits were moved from -10mm to + 10mm. The same was done for the vertical emittance measurement.

Figure **??** shows the measured, shaped beam distributions behind the quadrupole triplet (ϵ in Table 4.25). It is no surprise that the emittance has been drastically reduced, but by paying the price of losses. Yet, in the future, it could be taken into consideration to shape the beam with slit plates. The RFQ's transmission can be improved by increasing the electrode voltage. This will increase the transversal focusing and for that reason more of the beam will be accepted and transmitted through. But increasing the transversal focusing has an effect on the longitudinal emittance. Too strong focusing can change the beam phase spread, to which the IH-DTL is very sensitive. So the price for better transmission in the RFQ, might be increased losses in the DTL. To avoid this, it should be considered to shape the beam to a good relative transmission and then increase the output current to match the 400 μA criterion for the IH-DTL. How the increase of output current affects the initial emittance in the LEBT is subject to future studies at the MedAustron facility.

Another matter, which is of highest interest, is how much of the beam can be transported through the IH-DTL, which will be installed downstream the RFQ in Wiener Neustadt. The un-normalized transverse acceptance of the IH-DTL is 47 $\pi.mm.mrad$ in both planes. An emittance measurement after the RFQ would reveal, which fraction of the beam is within the acceptance of the IH-DTL.

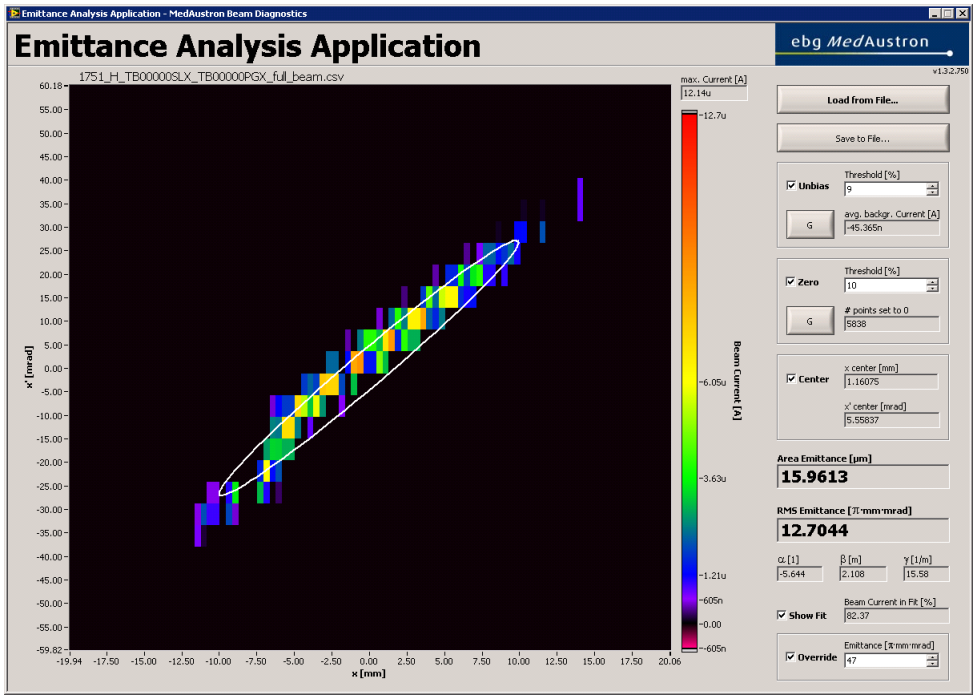

Figure 4.51: XX' emittance

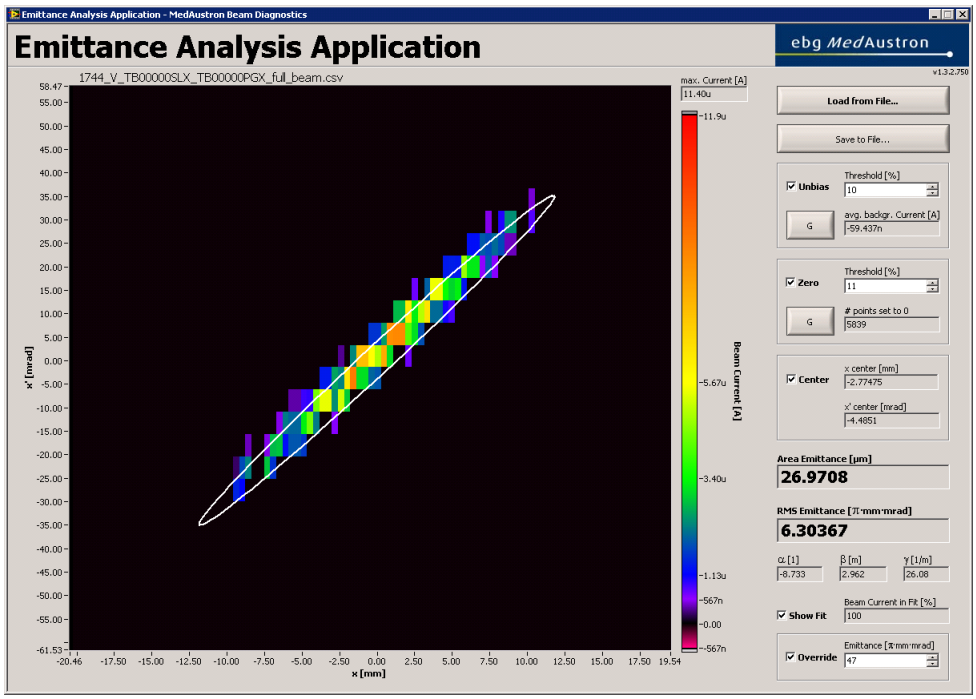

Figure 4.52: YY' emittance

	$\alpha[1]$	$\beta[mm/mrad]$	beam in 47 $\pi.mm.mrad$
XX'	-5.64	2.11	82.37%
YY'	-8.73	2.96	100 %

Table 4.26: measurement after solenoid

These measurements allow an optimistic look into the future, when operating the IH-DTL in Wiener Neustadt. In both cases over 80% of the beam is within the acceptance of the IH-DTL. The emittance measurement was done using emittance slits and a Profile Grid monitor (PGX). The PGX is a device which is still under development and is very prone to noise. So the measurements are to be taken with some caution and should only be considered as a rough estimate, especially for such a highly diverging beam.

4.3.8 Conclusions from the ITS operation

After 10 months of configuring and operating the Ion Source, the LEBT and the RFQ many lessons have been learned. The importance of key elements, such as alignment, device reliability, a good control system and the RFQ temperature stability have been underlined strongly during this test phase of the MedAustron Injector. To ensure a stable operation over longer periods of time a reliable and robust control system must be implemented that has to undergo heavy testing over a long period of time. Most of the troubles that were encountered during operation were caused by the main communication layer currently used in the project (LabView Shared Variable Engine). The devices themselves (magnets, power supplies, RFQ, RF-amplifier, Ion Source, Beam Diagnostics, vacuum pumps) have proven to operate reliably and can be left operational over a long period of time. The measurement results have shown that the RFQ is fully functional. The output energy has been proven to be 400 keV/u. A beam transmission of 72% was achieved and can be further increased by improving the input beam emittance and proper alignment of the RFQ. Improvements of the alignment system are required. The final cooling system and temperature stabilization of the RFQ have to be implemented for stable and reliable operation. There is certainly a room for improvement, but nevertheless the beam delivered by the RFQ is adequate for further testing of downstream systems (matching section, IH-DTL).

5 Simulation Software

An important section of the thesis is the simulation of the beam through the ITS to predict measurements or parameters optical devices. To gain useful predictions are large variaty of programs was used. In this section the programs will be introduced and what they were used for explained.

5.1 TRACE 3D

Trace 3D is an interactive program with a graphical user interface that allows quick analysis of the beam line. It includes various optical elements such as drifts, thin lenses, quadrupoles, permanent-magnet-quadrupoles (PMQ), solenoids, quadrupole doublets and triplets, bending magnets, RF gaps, RFQs, RF cavities, coupled-cavity tanks, and wiggler magnets. The so called σ-matrix, which was introduced by the program TRANSPORT [16] (which was not used in this thesis). The σ-matrix defines a six-dimensional hyperellipsoid in phase-space which represents the beam. Projecting this hyperellipsoid on any two-dimensional plane gives information on the boundary of the beam in this plane. Useful for analysis are the transverse (x-x' and y-y') and the longitudinal ($\Delta E - \phi$) plane. The projection of a hyperellipsoid on a two-dimensional subspace gives an ellipse. This ellipse is characterized by the Courant-Snyder or Twiss parameters discussed earlier. Using the matrix formalism introduced in CHAPTER LOLWUT the characteristics of the beam can be tracked between two elements. Using a simple text command interface the user can manipulate the elements. TRACE 3D allows to see the effects of manipulating optical devices on the beam very quickly. It also includes several routines that are able to match the beam, for example by varying quadrupole gradients, to desired parameters. This works very well for matching a beam to an RFQ, or matching between and RFQ and a DTL. TRACE 3D also includes space charge calculations, but it assumes that the space-charge forces are linear. The graphical user interface provided by TRACE 3D includes beam envelopes, dispersion and phase-space ellipses. The immediate graphical display when changing beam line parameters makes TRACE 3D a very intuitive and interesting tool for not just analysis and designing but also for learning. [17]

5.2 Path Manager

Path Manager is the graphical version of Travel. It also is a program that calculates beam properties through out the beam line. The major difference to TRACE3D is

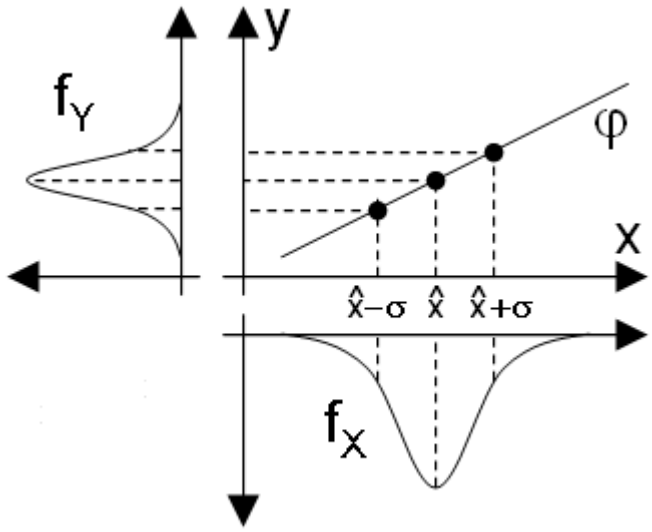

Figure 5.1: example of a linear system mapping

though, that it does not apply the matrix formalism onto the Twiss parameters. It uses a particle distribution and calculates the trajectories of each particle separately. This of course results in longer computation time, but also in higher accuracy. One can also include aperture constraints. Since Path Manager tracks each particle separatly, the feature of aperture constraints allows to analyze the transmission of a beam line to high detail. Path Manager generates an outputfile, that allows the user to see where and which particle was lost during transmission. A very strong aspect of Path Manager is that one can use a particle distribution based on measurement. So it is possible to simulate a "real" particle beam within one's beam-line. This opens the opportunity to design a beamline around a non-idealized beam. Path Manager offers a variety of different devices (quadrupole, bending magnet, etc.) to be included in the beam line. It also has one additional powerful feature and that is to include a device simply by its field map. So for example, by importing an electrostatic field map from the program VectorFields (a 3D electrodynamics simulation tool) one can simulate the devices' effect on the beam. [18] Another very useful aspect of Path Manager is the error-study routine Delta. This feature allows to generate a study of possible errors in fields, allignment, distances, etc. It creates a system mapping of values around the design parametes. The error follow a certain distribution (uniform or gaussian). Mathematically speaking the mapping can be understood as the evaluation of the a function of the form

$$\phi : \mathfrak{R}^n \rightarrow \mathfrak{R}^m \tag{5.1}$$

with $\mathfrak{R}^n$ being the space of the values on which and error is applied and $\mathfrak{R}^m$ the space of beamline parameters. 5.1 gives an easy example of a linear mapping. The x-axis represents the pertubated parameters and the y-axis represents the corresponding image.

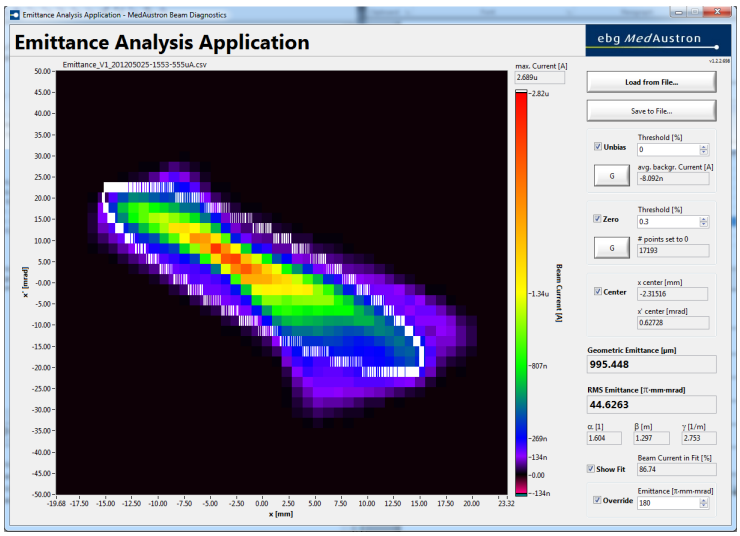

Figure 5.2: MedAustron Emittance Analysis

In general there are two ways to evaluate this function. A statistical approach using a Monte Carlo method and an analytical one. The error study feature is not limited to simply study the effects of errors. It can also be used as a beam matching routine. Using beam line parameters obtained from the matching routine used in TRACE 3D in Path Manager and then starting an error study with errors around those parameters allows for a quick and accurate matching proceedure. [19]

5.3 genBeam

GenBeam is a program that generates a particle distribution out of emittance measurement data. It reads out measurement data to define a histogram which is then filled up by random numbers representing coordinates in transversal phase-space. It assumes that the particles are all of the same energy and evenly distributed in phase over 360 °. The output file is in text format and can be edited with any texteditor and Microsoft Excel. It can also be used as a source file for Path Manager. This allows very interesting simulations throughout a beam line. [20]

5.4 MedAustron Emittace Analysis

EBG MedAustron has developed its own emittance analysis program for measurement data. It includes noise filtering algorithms and phase-space ellipse fitting. It is capable of calculating Twiss parameters and RMS and geometrical emittance. It can also save the noise filtered data in a format that can be used for further processing in genBeam.

5.5 PARMTEQM

PARMTEQM is used for RFQ beam dynamics simulations. With already provided design of the RFQ it is possible to simulate the dynamics of a particle distribution throughout the RFQ. It uses 2-dimensional space charge calculation. It's output offers a large spectrum of data. Manipulating certain parameters in the input-file (for example the vane voltage tilt) gives the opportunity to scan for a wide area of properties. PARMTEQM also covers the effects of higher order multipol fields caused by circular vane tips. [21]

5.6 PlotWin

PlotWin is a tool, that is capable of graphically displaying beam distributions. It can project 6D-distributions on a two dimensional subspace. Also beam properties such as emittance and Twiss parameters are being calculated out of the the beam distribution. It can load various types of datasets which allows easier comparison of simulation and measurement.

Bibliography

[1] Jay S Loeffler Marco Durante. Charged particles in radiation oncology.

[2] Tobias Kulenkampff. Emittance measurements via quad scans an analysis implementation at medaustron.

[3] Thomas P. Wangler. *Principles of RF Linear Accelerators*. WILEY-VCH Verlag GmbH & Co. KGaA, 2004.

[4] S. Turner, editor. *CAS CERN Accelerator School, Fifth General Accelerator Physics Course*. CERN, 1994.

[5] E. Sargsyan. Rf linacs, ma lecture, May 2011.

[6] Jr T. J. Boyd. Kilpatrick's criterion. Technical report, Los Alamos Group AT-1, February 12, 1982.

[7] Markus Stockner. E-mail exchange.

[8] Mario Conte and William MacKay. *An Introduction To The Physics Of Particle Accelerators*.

[9] Emmanuell Branlard. 2009fermi. URL `http://emmanuel.branlard.free.fr/work/papers/html/2009fermi/node18.php`.

[10] I.M. Kapchinskiy and V.A. Tepliakov. *Prib. Tekh. Eksp. 2 19-22*, 1970.

[11] Geek3. Vectorfieldplot. URL `https://commons.wikimedia.org/wiki/User:Geek3/VectorFieldPlot`.

[12] Alessandra Lombardi. Radio frequency quadrupole cas. URL `https://cas.web.cern.ch/cas/Holland/PDF-lectures/Lombardi/RFQ.pdf`.

[13] Oliver Meusel. E-mail correspondance.

[14] Christoph Wagner. Email correspondance, 2012.

[15] Vretenar M. Field emission measurements on rfq2 and recalibration of the vane voltage. *PS/RF/Note 91-11 (MD)*, 1997.

[16] K. L. Brown and S. K. Howry. Transport/360. Technical report, SLAC, 1970.

[17] K. R. Crandall D. P. Rusthoi. *TRACE 3-D Documentation*. Los Alamos National Laboratory, third edition edition, May 1997.

[18] Arnaud PERRIN Jean-François Torsten Mütze Jean-Baptiste Sara Lanzone. *CERN TRAVEL v4.07 User Manual*. CERN, April 2007.

[19] Torsten Mütze Sara Lanzone. *Delta User Manual*. CERN, April 2007.

[20] Dinah BOUMA James STOVALL. *genBeam v1.0*. CERN, June 2009.

[21] Lloyd M. Young James H. Billen George H. Neuschaefer Kenneth R. Crandall, Thomas P. Wangler and Dale L. Schrage. *RFQ Design Codes*. Los Alamos National Laboratory, 3.0.7 edition, December 2005.